

CORRESPONDENCE:

graham.andrews@mail.wvu.edu

CITATION: Andrews, G.D.M., Busby, C.J., Brown, S.R., Fisher, C.M., Davila-Harris, P., Strickland, A., Vervoort, J.D., Pettus, H.D., McDowell, F.W., and Murray, B.P., 2022, Petrogenesis of voluminous silicic magmas in the Sierra Madre Occidental large igneous province, Mexican Cordillera: Insights from zircon and Hf-O isotopes: *Geosphere*, v. 18, no. 3, p. 946–984, <https://doi.org/10.1130/GES02430.1>.

Science Editor: Shanaka de Silva
Guest Associate Editor: Jonathan S. Miller

Received 5 March 2021
Revision received 6 December 2021
Accepted 28 January 2022

Published online 25 February 2022



This paper is published under the terms of the CC-BY-NC license.

© 2022 The Authors

Petrogenesis of voluminous silicic magmas in the Sierra Madre Occidental large igneous province, Mexican Cordillera: Insights from zircon and Hf-O isotopes

Graham D.M. Andrews^{1*}, Cathy J. Busby^{2*}, Sarah R. Brown^{1*}, Christopher M. Fisher^{3*}, Pablo Davila-Harris^{4*}, Ariel Strickland^{5*}, Jeffrey D. Vervoort^{6*}, Holly D. Pettus^{1*}, Fred W. McDowell^{7*}, and Bryan P. Murray^{8,*}

¹Department of Geology and Geography, West Virginia University, 98 Beechurst Avenue, Morgantown, West Virginia 26505, USA

²Department of Earth and Planetary Sciences, University of California Davis, Davis, California 95616, USA

³School of Earth Sciences, University of Western Australia, 35 Stirling Highway, Perth, Western Australia 6009, Australia

⁴División de Geociencias Aplicadas, Instituto Potosino de Investigación Científica y Tecnológica, San Luis Potosí, SLP, 78215, Mexico

⁵Department of Geoscience, University of Wisconsin, 1215 W. Dayton Street, Madison, Wisconsin 53706, USA

⁶School of Earth and Environmental Sciences, Washington State University, Pullman, Washington 99164, USA

⁷Department of Geological Sciences (retired), Jackson School of Geosciences, University of Texas at Austin, Austin, Texas 78712, USA

⁸Department of Geological Sciences, Cal Poly Pomona University, 3801 West Temple Avenue, Pomona, California 91768, USA

ABSTRACT

Combined Hf-O isotopic analyses of zircons from tuffs and lavas within the Sierra Madre Occidental (SMO) silicic large igneous province are probes of petrogenetic processes in the lower and upper crust. Existing petrogenetic and tectonomagmatic models diverge, having either emphasized significant crustal reworking of hydrated continental lithosphere in an arc above the retreating Farallon slab or significant input of juvenile mantle melts through a slab window into an actively stretching continental lithosphere. New isotopic data are remarkably uniform within and between erupted units across the spatial and temporal extent of the SMO, consistent with homogeneous melt production and evolution. Isotopic values are consistent with enriched mantle magmas (80%) that assimilated Proterozoic paragneisses (~20%) from the lower crust. $\delta^{18}\text{O}_{\text{zircon}}$ values are consistent with fractionation of mafic magma and not with assimilation of hydrothermally altered upper crust, suggesting that the silicic magmas evolved at depth. Isotopic data agree with previous interpretations where voluminous juvenile melts entered the lithosphere during the transition from a continental arc experiencing slab rollback (Late Eocene) to the arrival of a subducting slab window (Oligocene and Early Miocene) and failure of the upper plate leading to the opening of the Gulf of California (Late Miocene). An anomalously large heat flux and extension of the upper plate allow for the sustained fractionation of the voluminous SMO magmas and assimilation of the lower crust.

Graham D. M. Andrews <https://orcid.org/0000-0002-7911-702X>

Sarah Brown <https://orcid.org/0000-0002-8762-3301>

Pablo Dávila Harris <https://orcid.org/0000-0002-0620-5459>

Jeff Vervoort <https://orcid.org/0000-0002-1138-4527>

*E-mail: graham.andrews@mail.wvu.edu; cjbusby@ucdavis.edu; srbrown19@gmail.com; chris.fisher@uwa.edu.au; pablo.davila@ipicyt.edu.mx; ariel23tx@gmail.com; vervoort@wsu.edu; hdpettus@mix.wvu.edu; fwmcdowell@yahoo.com; bpmurray@cgp.edu

INTRODUCTION

This is a study of the petrogenesis of voluminous rhyolites in the Sierra Madre Occidental (SMO) silicic large igneous province (SLIP) of northwestern Mexico (Fig. 1) through the lens of Lu-Hf and O isotopes in zircons dated by U-Pb geochronology. The SMO is the largest Cenozoic SLIP (Bryan and Ferrari, 2013) and is therefore an important natural laboratory to examine the petrogenesis of voluminous silicic magmas. Moreover, the SMO is an atypical SLIP not associated with continental breakup (e.g., Chon Aike) nor with a mantle hotspot (e.g., Yellowstone). Specifically, this is a regional-scale study of the northern and central SMO that tests competing hypotheses for the formation of the eponymous Eocene to Miocene ignimbrite flare-up events and offers insights into the formation of voluminous silicic magmas in an extending continental arc setting (e.g., Taupo, etc.). Through analysis of 49 rhyolitic to dacitic ignimbrites and lavas, we reveal ~25 m.y. of monotonous silicic magma production associated with fractionation of mantle-derived juvenile melts mixing with lower-crustal anatectic melts throughout the SMO. We demonstrate that Hf and O isotopic values are compatible with a largely primitive source for melts and heat in the mantle and only ~20% recycling of paragneissic continental crust. This analysis supports one set of models and strongly refutes others that argue for a dominantly crustal recycling petrogenesis and, therefore, emphasizes the importance of material and heat transfer from the mantle to the continental crust during arc rifting.

Sierra Madre Occidental Silicic Large Igneous Province

The middle Eocene to early Miocene SMO (Fig. 1) is the most voluminous (~3.9 × 10⁵ km³; Bryan et al., 2008) Cenozoic SLIP on Earth (Bryan and Ferrari,

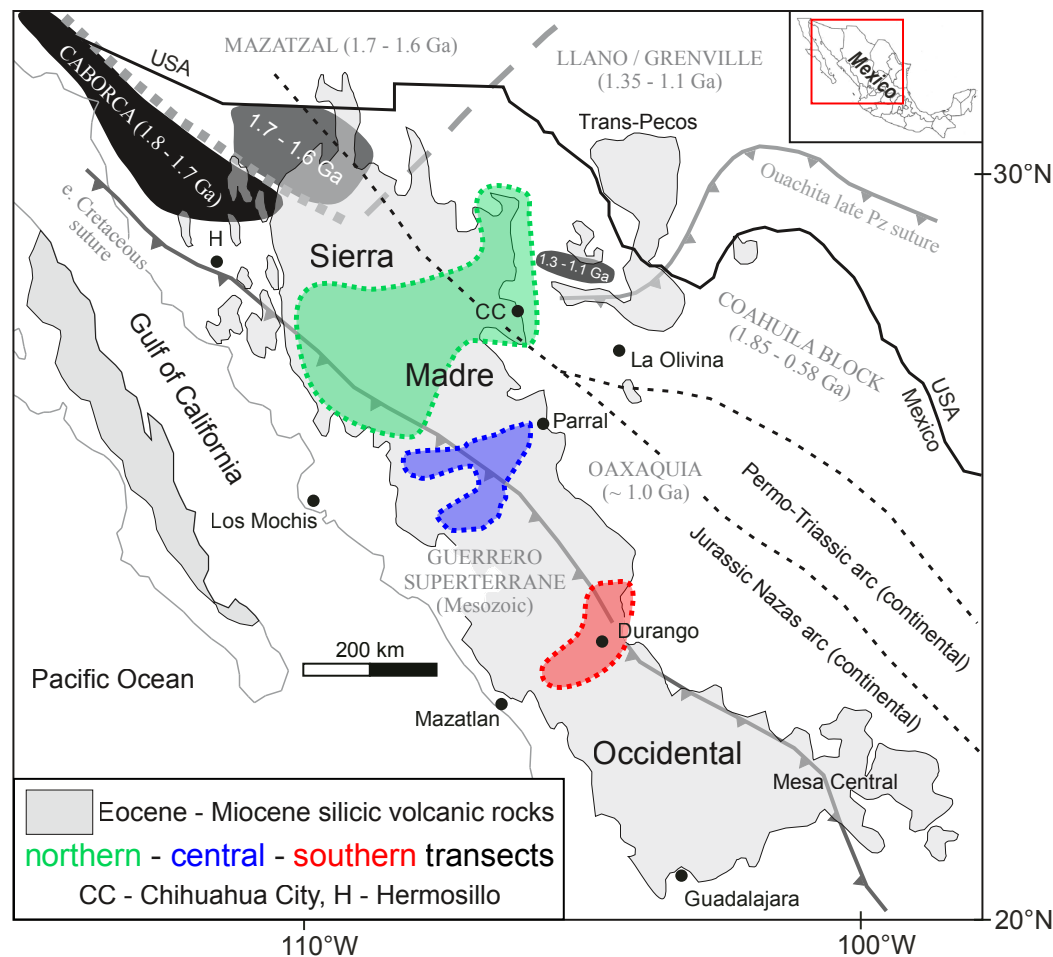


Figure 1. Simplified geological map of northwestern Mexico depicting the Sierra Madre Occidental (SMO) silicic large igneous province, inferred basement blocks, and the locations of the three transects discussed in this paper. SMO outline adapted from Ferrari et al. (2002). Basement block and terrane boundary outlines adapted from Campa and Coney (1983), Kerppe and Ortega-Gutiérrez (1995), Dickinson and Lawton (2001), and Ortega-Gutiérrez et al. (2018).

2013) and is host to the world's largest epithermal Ag province (Camprubí et al., 2003). The ash dispersed during the SMO ignimbrite eruptions has been suggested as a driver of global cooling at the Eocene–Oligocene transition and the onset of Antarctic glaciation (Cather et al., 2009; Jicha et al., 2009). The SMO buries ~400,000 km² beneath a 1–1.5 km thickness of silicic ignimbrites and lavas (Fig. 1; McDowell, 2007; Bryan et al., 2008), forming a central plateau with mean elevation 2000 m above sea level (Fig. 2). The margins of the SMO are extended, tilted, and truncated by normal fault-bounded graben and half-graben of the southern Basin and Range province in the east (Henry and Aranda-Gomez, 1992, 2000) and the Gulf of California extensional province in the west (e.g., Ferrari et al., 2013). The elevated core is less extended and

is characterized by subhorizontal ignimbrite sheets (>10 km² each) exposed for tens of kilometers in canyon walls and on peaks and ridges, with isolated clusters of contemporaneous lava domes and several large calderas (e.g., Swanson et al., 2006).

The SMO forms the southern and largest part of an ignimbrite flare-up that extended from British Columbia to Mexico from the Eocene to the earliest Miocene, widely interpreted to result from rollback of the Farallon slab that had been subducting under North America since the Jurassic (e.g., Sedlock et al., 1993). The silicic SMO arc developed on the remnants of the Paleocene–Eocene continental arc that had formed during slab flattening, which in turn, was constructed on the Mesozoic continental margin (Fig. 1). However, the

SMO is understudied compared to other parts of the Cordilleran arc, and much of it remains unexplored: even basic knowledge of its internal architecture, stratigraphy, and geochronology is lacking. What understanding there is comes from studies along the few roads that exist, and a few regional-scale geophysical studies (e.g., Bonner and Herrin, 1999; Purucker et al., 2007). Many published studies of the northern and central SMO are constrained by either a small number of samples (e.g., Bryan et al., 2008), a small study area (e.g.,

Murray et al., 2013), or both (e.g., Mahar et al., 2019), limiting understanding of regional variations and patterns. The available age data are relatively sparse compared to the total area and the total age range and are probably biased by accidental over-sampling of some widespread units (e.g., Vista Tuff; McDowell and McIntosh, 2012) and under-sampling in less accessible areas and in poorly exposed, non-welded units. The few regional-scale compilations available are focused on K/Ar and Ar/Ar geochronology and the first-order

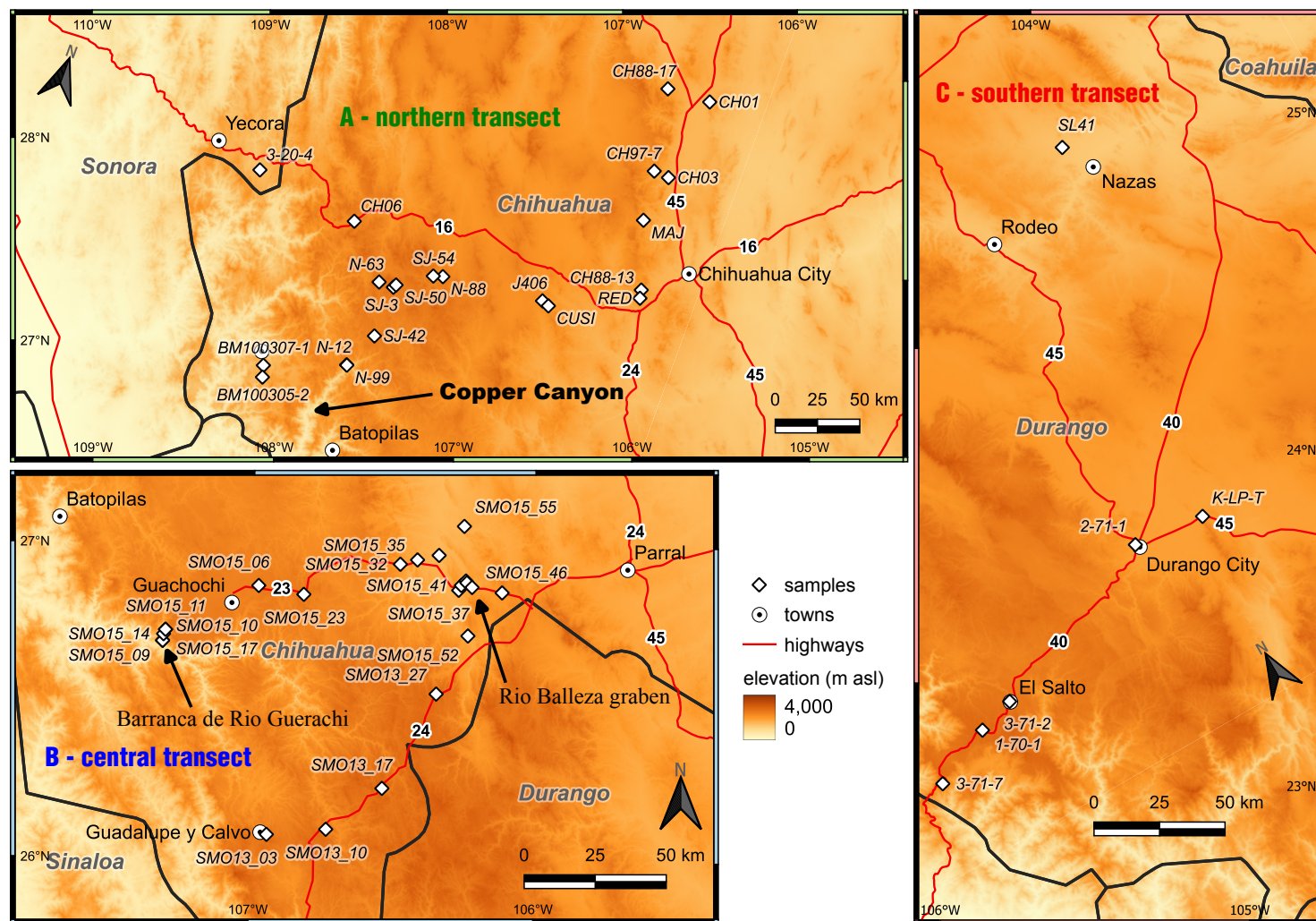


Figure 2. Locations of samples along the northern (A), central (B), and southern (C) transects.

geological history of the SMO (Ferrari et al., 2007; McDowell and McIntosh, 2012; Ferrari et al., 2018).

Silicic volcanism generally migrated southwestward after slab rollback began at ca. 40 Ma (Damon et al., 1981). The northern and central SMO experienced several localized, ~2-m.y.-long, ignimbrite flare-ups throughout the period with ca. 46–42 Ma and 38 Ma (mainly north of Chihuahua City; Fig. 2A), 36–28 Ma (widespread), and ca. 24–18 Ma (southwestern margins) being significant timespans although not necessarily discrete events (McDowell, 2007; McDowell and McIntosh, 2012). The largest flare-up pulse was at 36–28 Ma, with a total volume flux of $\sim 3.0 \times 10^6 \text{ km}^3$ (Bryan and Ferrari, 2013). The late Oligocene pulse (25–23 Ma) encroached on the western margins of the northern and central SMO where it is unconformable upon and recycles zircon from the much more voluminous middle Eocene–middle Oligocene (36–28 Ma) volcanic succession (e.g., Murray et al., 2013; Mahar et al., 2019). This pulse is contemporaneous with the oldest parts of the predominantly early Miocene (24.5–18 Ma) ignimbrite flare-up in the southernmost SMO (Ferrari et al., 2007; Aguirre-Díaz et al., 2008; Bryan and Ferrari, 2013; Ferrari et al., 2013), which we will not discuss further.

Volcanism appears to have developed as ~100–150-km-wide clusters of similar-aged calderas, lava dome complexes, and fissure vents at different times along each transect (McDowell and Keizer, 1977; Swanson and McDowell, 1984, 1985; Swanson et al., 2006; McDowell and McIntosh, 2012; Ferrari et al., 2013; Murray et al., 2013). The relative paucity of calderas identified in the SMO compared to the number of thick and extensive ignimbrites suggests that either many calderas remain to be discovered (e.g., Swanson and McDowell, 1984; Henry et al., 2012; McDowell and McIntosh, 2012) or that many eruptions were fed by fissure vents bounding or within graben (Aguirre-Díaz and Labarthe-Hernández, 2003; Torres-Hernández et al., 2006; Aguirre-Díaz et al., 2008; Tristán-González et al., 2008; Murray et al., 2013).

Competing Models of SMO Petrogenesis

The majority of SLIPs are associated with either intracontinental hotspot volcanism (e.g., Yellowstone–Snake River Plain), continental rifting (e.g., Whit Sunday), or both (e.g., Etendeka–Paraná), and may or may not be associated with voluminous mafic volcanism (Bryan and Ferrari, 2013). The SMO is unusual among SLIPs for being an arc; although large calderas and large-volume rhyolitic eruptions occur in arc settings (e.g., Altiplano–Puna, Bolivia; Taupo volcanic zone, New Zealand; Kyushu arc, Japan), none match the scale and duration of the SMO. Attempts to explain the tectonic influences on the petrogenesis of SMO magmas fall into two categories: (1) waning of the Cordilleran arc accompanied by rollback of the Farallon slab (e.g., Wark, 1991; McDowell and Mauger, 1994; McDowell and McIntosh, 2012); and (2) breakup of the Farallon slab and opening of a slab window beneath western Mexico (Mahar et al., 2019), accompanied by waxing lithospheric extension leading to seafloor spreading in the Gulf of California (Ferrari et al., 2018, and references therein).

Geochemical studies of the SMO rhyolites, coeval mafic lavas, and Cenozoic xenolith localities in the 1980s and 1990s were dominated by whole-rock elemental and isotopic (Sr and Nd) analyses and modeling to test between petrogenesis through assimilation of continental crust, fractionation of mantle-derived mafic magmas, or a combination of the two (assimilation-fractional crystallization [AFC]). Such studies produced contradictory interpretations for rhyolite petrogenesis. For example, Ruiz et al. (1988b) inferred up to 100% melting and recycling of Paleozoic and older lower continental crust, and Bryan et al. (2008) interpreted zircon solubility and age data as evidence in favor of crustal melting. Alternatively, relatively closed-system fractionation of arc-derived mafic and intermediate magmas with $\leq 20\%$ lower-crustal contamination satisfies AFC mixing models in several studies (e.g., Lanphere et al., 1980; Cameron and Cameron, 1985; Cameron et al., 1986; Wark, 1991; Smith et al., 1996). Analysis by Mahar et al. (2019) of Hf isotopes in zircons from southwestern Chihuahua suggests that 90–50 Ma plutons and early Miocene SMO rhyolites share a common source in the subcontinental lithospheric mantle and were produced by AFC processes. Analysis by Ferrari et al. (2018) of Oligocene to Pliocene mafic and silicic rocks throughout northwestern Mexico reveals a transition from calc-alkaline magmas that incorporated continental crust (low-negative ϵ_{Nd}) before 20 Ma and increasingly tholeiitic, uncontaminated, mantle-derived magma after that. They interpret this to reflect the cessation of arc magmatism and the increasing dominance of crustal extension and eventual tapping of the asthenospheric mantle.

This Study

This paper focuses on the isotopic geochemistry of zircon to elucidate the petrogenesis of SMO magmas and to assess competing tectonomagmatic models. Combined zircon U–Pb, Hf, and O studies are excellent tools for studying the origin of igneous and metaigneous rocks and have been applied to high-grade metamorphic assemblages (e.g., Zheng et al., 2006; Hiess et al., 2009, 2011) and batholith complexes (e.g., Kemp et al., 2007; Appleby et al., 2010; Bolhar et al., 2012; Zhao et al., 2013) to evaluate crustal growth mechanisms and rates (e.g., Hawkesworth and Kemp, 2006; Kemp et al., 2006). This O–Hf–U/Pb in zircon method has been applied to only a few silicic volcanic systems including Yellowstone–Snake River Plain SLIP (e.g., Stelten et al., 2013; Colón et al., 2018) and Iceland (e.g., Banik et al., 2018; Carley et al., 2020); this is the first application to the SMO.

Our samples come from the northern and central SMO collected from three transects: northern, central, and southern (Figs. 1 and 2), all in the ancestral homelands of the displaced Rarámuri people. From north to south: (A) the ~250-km-long northern transect, which extends from Chihuahua City to the Hermosillo area (Cochemé and Demant, 1991; Swanson et al., 2006; McDowell, 2007; Murray et al., 2013, 2015; Murray and Busby, 2015); (B) the ~150-km-long central transect in the Chihuahua–Durango border region west of Parral; and (C) the ~100-km-long southern transect from Durango to just east of Mazatlán (Aguirre-Díaz and McDowell, 1991, 1993; Ferrari et al., 2007; Aranda-Gómez

et al., 2015). This is the first study of the central transect. All three transects include samples from the high-elevation SMO plateau and the adjacent rifted eastern margins of the southern Basin and Range (Fig. 2), thus allowing us to look for variations across the complete extent and timespan of the SMO and across the structural boundaries of the non-extended core.

METHODS

Zircon (ZrSiO_4) is uniquely able to record isotopic changes during rhyolite petrogenesis because it is abundant, refractory, and preserves useful textural information. It is often one of the only phases present in magmas erupted close to their liquidus. Zircon readily incorporates Hf over Lu ($\text{Lu}/\text{Hf} \sim 0.002$) in substitution for Zr (0.5–2.0 wt%; Kinny and Maas, 2003) and has a strong affinity for U but not for Pb, making it ideal for both U-Pb geochronology and Hf isotope analyses. Importantly, zircon allows for only very slow diffusion of O and cations; therefore, O and Lu-Hf isotope ratios in zircon are typically not reset by metamorphism or metasomatism (Valley et al., 1994; Kinny and Maas, 2003; Page et al., 2007; Bowman et al., 2011).

Oxygen and Hf isotopes inform on the sources of magmas (Hawkesworth and Kemp, 2006). Hafnium isotopes are radiogenic and are sensitive to the ages of rocks being melted (Kinny and Maas, 2003); conversely, O isotopes are stable and reflect the specific oxygen isotope compositions of the melts from which they crystallized (Valley, 2003). Mantle-derived magmas are expected to have strongly positive ϵHf values and $\delta^{18}\text{O}_{\text{zircon}}$ values $\sim 5.3\text{‰} \pm 0.3$ (1 σ ; Valley, 2003).

Anatectic magmas are expected to have widely variable $\delta^{18}\text{O}_{\text{zircon}}$ values and ϵHf values correlated to the nature of the protolith: low-positive to low-negative for melting of metagneous rocks and strongly negative for metasedimentary rocks.

Sample Preparation

Zircon separates were prepared by standard methods at the University of California Santa Barbara (UCSB) and California State University Bakersfield (CSUB). Samples were crushed by hand with a mortar and pestle and then by jaw crusher and BICO disk mill. Sand-sized crush was sieved to remove grains greater than 200 μm and then was density separated on a water table. The densest fractions underwent magnetic separation, followed by separation of apatite from zircon by flotation in methylene iodide (MEI). Zircon concentrates were mounted in Epofix epoxy and imaged by scanning electron microscopy and cathodoluminescence (CL) at CSUB, the University of Wisconsin Madison, and the University of Idaho.

Zircon recovery varied from minimal (≤ 5 grains per sample) to abundant (1000 s), with no systematic correlations between abundance and age or location. Zircon are uniformly prismatic and oscillatory zoned under CL (Fig. 3). Grains typically range from ~ 40 –150 μm in length and are usually euhedral or subhedral. Many grains contain melt inclusions. High CL contrast cores are common and subhedral, but only very rarely display internal zoning discordant to the outer rims. Zircon grains were analyzed for U-Pb, Hf, and O isotopes in the same core and rim locations determined by CL imaging.

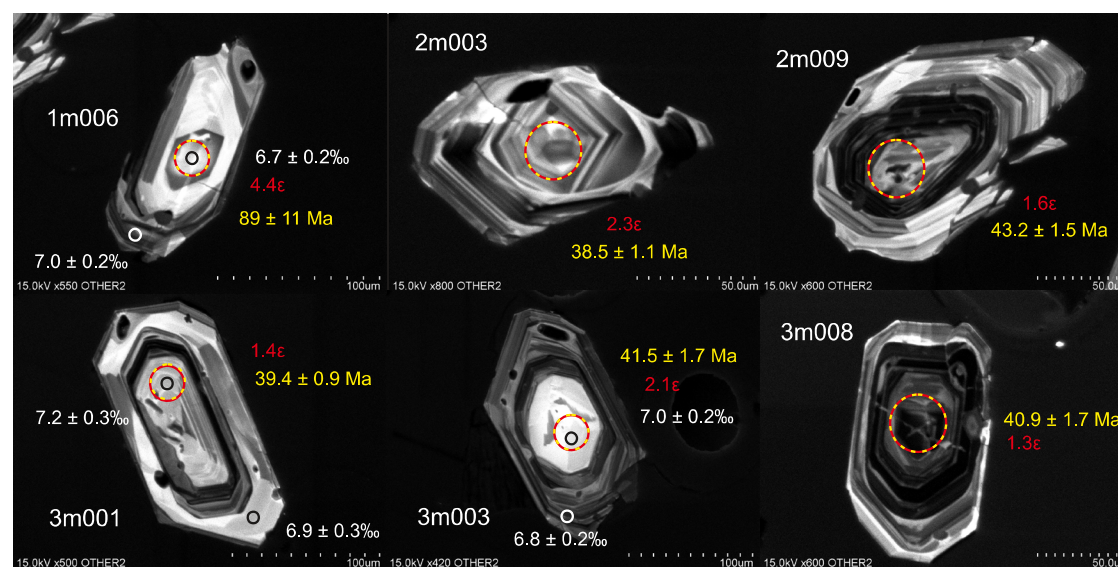


Figure 3. Example of coincidence of spot-analyses by secondary ion mass spectrometry (SIMS) (University of Wisconsin Madison) and laser ablation split-stream (LASS) (Washington State University) in cathodoluminescence (CL) images of oscillatory zoned euhedral and subhedral zircon grains from sample RED. SIMS spot diameter is ~ 15 μm and LASS spot diameter is ~ 40 μm . $^{206}\text{Pb}/^{238}\text{U}$ crystallization ages are shown in yellow, ϵHf , values in red, and $\delta^{18}\text{O}_{\text{zircon}}$ values in white.

Oxygen Isotope Analysis

Oxygen isotopes in zircons were measured at the University of Wisconsin-Madison (Kita et al., 2009; Valley and Kita, 2009) and the University of California Los Angeles secondary ion mass spectrometry (SIMS) laboratories.

Samples from the northern and southern transects were analyzed on the CAMECA IMS-1280 ion microprobe at the WiscSIMS Laboratory, University of Wisconsin-Madison against the KIM-5 zircon standard ($\delta^{18}\text{O} = 5.09 \pm 0.06\text{‰}$ (1σ) Vienna standard mean ocean water [V-SMOW]; Valley, 2003). Samples were cast within 7 mm of the center of 25.4-mm-diameter epoxy mounts, ground to approximate midsection, and polished. Sample relief was evaluated by profilometer. Data were acquired in four 12–15 h sessions following the procedures described previously (Kita et al., 2009; Valley and Kita, 2009). Three Faraday cup detectors were used to simultaneously analyze $^{16}\text{O}^-$, $^{16}\text{O}^1\text{H}^-$, and $^{18}\text{O}^-$. Ratios of OH/O were background corrected against values on bracketing anhydrous KIM-5 and provide a monitor of “water,” which might result from inclusions or metamict zones within a zircon (Wang et al., 2014). Analyses were conducted using a 1.9–2.2 nA primary Cs^+ beam with a spot diameter of 10 μm . The KIM-5 standard was analyzed four times between every batch of 10–15 sample spots to calibrate analyses and evaluate possible drift. The mean precision (1σ) of analyses is 0.15%. Usually eight to ten analyses were made on up to 12 different grains.

Oxygen isotopes from samples from the central transect were analyzed on the CAMECA IMS-1290 ion microprobe at UCLA against the R33 ($\delta^{18}\text{O} = 5.55 \pm 0.04\text{‰}$ (1σ) V-SMOW; Valley, 2003) and Mud Tank ($\delta^{18}\text{O} = 5.03 \pm 0.10\text{‰}$ (1σ) V-SMOW; Valley, 2003) standards. Data were acquired in two 8–12 h sessions following the procedures described by Trail et al. (2007). Analyses were conducted using a focused 2–3 nA primary Cs^+ beam with a spot diameter of 10–15 μm . Usually 10–12 analyses were made on up to 12 different grains.

Oxygen isotopes were measured in quartz phenocrysts from eight samples (five from the northern transect and three from the southern transect) by laser fluorination at the University of Wisconsin-Madison (Spicuzza et al., 1998; Valley, 2003). Anhedral, 100–200- μm -diameter quartz crystals were concentrated by HF digestion of a coarse, sand-sized aggregate, and then were handpicked. Samples were run against the UWG-2 standard ($\approx 5.8 \pm 0.15\text{‰}$ (1σ) V-SMOW; Valley et al., 1995). Six quartz samples (four from the northern transect and two from the southern transect) correspond with analyses of coexisting zircon (samples CH03, CH97-7, N-99, SJ-54, K-LP-T, and SL-41).

Uranium-Lead and Lutetium-Hafnium Isotope Analysis

Zircons were subsequently analyzed by laser ablation–inductively coupled mass spectrometry (LA-ICPMS) and SIMS to measure U-Pb and Lu-Hf analyzes.

Archived samples from the northern and southern transects were analyzed for U-Pb and Hf simultaneously in ~8–11 grains by laser ablation split-stream (LASS) ICPMS at Washington State University (40 μm); ~10–12 additional U-Pb

ages were determined by LA-ICPMS (30 μm) for each sample. The LASS setup at Washington State University measures U/Pb and Lu-Hf isotopes simultaneously from a single ablation; the method is described in detail in Fisher et al. (2014). Samples are ablated using a NewWave 213 nm Nd:YAG laser using laser spot diameters of either 30 or 40 μm . The laser was operated at 10 Hz with a fluence of ~9–10 J/cm². The ablated material is transported out of the laser cell using helium carrier gas and is mixed with a small amount (5 mL/min) of N₂ gas, which is added using a plastic “Y” split ~30 cm after exiting the laser ablation system. The ablated *sample+He+N₂* mixture is then split into two separate paths, again using a “Y” split, an additional 30 cm downstream from the point of N₂ gas addition. One path carries the ablated aerosol to a ThermoScientific Element2 high-resolution ICPMS for U-Pb isotopic measurement, and a second path carries the ablated aerosol to a ThermoScientific Neptune MC-ICPMS for Lu-Hf isotopic measurement. Ar sample gas is added to each path ~20 cm from the torch.

Samples from the central transect were analyzed at UCLA and at the University of Arizona. U-Pb zircon geochronology was carried out in several analytical sessions on the CAMECA ims 1270 ion microprobe at UCLA, using established protocols for the analysis of Cenozoic zircon (Schmitt et al., 2003). Primary beam intensities for mass-filtered $^{16}\text{O}^-$ were ~20 and ~40 nA with a spot size of ~20–30 μm with depths after analysis being approximately one-tenth of the crater diameter. Oxygen flooding was used at the saturation pressure to enhance sensitivity for Pb. A ^{204}Pb -based common Pb correction was used for reference zircon, whereas ^{207}Pb was used as a proxy for common Pb for unknowns. Reproducibility of $^{206}\text{Pb}^*/^{238}\text{U}$ ages for AS3 (1099 Ma; Paces and Miller, 1993) used as a primary reference for the UO^+/U^+ versus U-Pb relative sensitivity calibration was ~2%–3% (relative), and accuracy of the weighted-average $^{206}\text{Pb}^*/^{238}\text{U}$ ages based on comparison with replicate analyses ($n = 10$ each) on 91500 reference zircon was ~1.5% (relative deviation from reported age of 1065 Ma; Wiedenbeck et al., 1995). Th/U in unknown zircon was determined from measured $^{232}\text{Th}^+/\text{U}^+$ using a relative sensitivity factor calibrated on measured $^{208}\text{Pb}^*/^{206}\text{Pb}^*$ of AS3 reference zircon. Uranium abundances were estimated from $\text{U}^+/\text{Zr}_2\text{O}^+$ in relation to zircon 91500 with 81 ppm U (Wiedenbeck et al., 2004).

U-Pb analyses were corrected in IsoplotR (Vermeesch, 2018) for common Pb based on measured ^{207}Pb , assuming $^{207}\text{Pb}/^{206}\text{Pb} = 0.8283$ (Sañudo-Wilhelmy and Flegal, 1994) and disequilibrium based on $\Delta\text{Th}/\text{U} = 0.17$ (Blundy and Wood, 2003). IsoplotR was used to calculate mean ages and to plot Tera-Wasserberg concordia.

Hf isotopic analyses were conducted on grains already dated at UCLA using a Nu Instruments HR multi-collector ICPMS connected to a Photon Machines Analyte G2 excimer laser at the Arizona LaserChron Center at the University of Arizona, following established analytical protocols described in Gehrels and Pecha (2014). Instrument settings were optimized for laser ablation analysis, and in-run analyses of seven different natural zircon standards (Mud Tank, Temora, FC52, R33, Plesovice, and Sri Lanka) were analyzed and monitored every 15–20 unknowns.

Ablation with a laser beam diameter of 40 μm targeted zircon domains directly over the earlier U-Pb analysis craters. All measurements were made in static mode using Faraday collectors equipped with $3 \times 10^{11} \Omega$ resistors. Each acquisition consisted of one 40-second integration for backgrounds (on peak with laser idle) followed by 60 1-second integrations with the laser firing. A 30-second delay between laser analyses provided adequate time to ensure the previous sample was completely purged from the collector block. The laser was run in constant energy mode with an output of 7.5 mJ (fluence $\sim 8 \text{ J/cm}^2$) and a pulse rate of 7 Hz. Isotope fractionation (β) was accounted for by incorporating the method of Woodhead et al. (2004) with β_{Hf} determined from the measured $^{179}\text{Hf}/^{177}\text{Hf}$ and β_{Yb} from the measured $^{173}\text{Yb}/^{171}\text{Yb}$ (except for very low Yb signals); β_{Lu} is assumed to be the same as β_{Yb} ; and an exponential formula is used for fractionation correction. Yb and Lu interferences are corrected by measurement of $^{176}\text{Yb}/^{171}\text{Yb}$ and $^{176}\text{Lu}/^{175}\text{Lu}$ (respectively), as advocated by Woodhead et al. (2004). Isotope ratios of $^{179}\text{Hf}/^{177}\text{Hf} = 0.73250$ (Patchett and Tatsumoto, 1981); $^{173}\text{Yb}/^{171}\text{Yb} = 1.132338$ (Vervoort et al., 2004); $^{176}\text{Yb}/^{171}\text{Yb} = 0.901691$ (Vervoort et al., 2004; Amelin and Davis, 2005); $^{176}\text{Lu}/^{175}\text{Lu} = 0.02653$ (Patchett, 1983) were used and all corrections are done line-by-line. Data reduction protocols account for all standards and unknowns analyzed during an entire session, and the β_{Hf} and β_{Yb} cut-offs were determined by monitoring the average offset of the standards from their known values resulting in a final standard offset of 0.0000001. $^{176}\text{Hf}/^{177}\text{Hf}$ uncertainty on the standard analyses for the entire session was determined to be 0.000037 (2σ).

RESULTS

A total of 49 samples (Table 1) were described (Supplemental Material, Section A¹) and analyzed including 21 from the northern transect, 22 from the central transect, and six from the southern transect (Fig. 2). The samples include silicic lavas and ignimbrites and encompass the full spatial and temporal range of volcanism in the northern and central SMO. The only unit knowingly duplicated was the Quemada Tuff (N-12 and N-88; Swanson et al., 2006).

Archived samples and mineral separates were analyzed from collections at the University of Texas Austin and the University of Texas San Antonio. Twenty-nine samples have a complete suite of $\delta^{18}\text{O}$, ϵ_{Hf_t} , and U/Pb age measurements on individual zircon grains.

Lithostratigraphy

New samples along the central transect were collected during field work along Federal Highways 23 and 24 in 2013 and 2015. Figure 4 is a graphic

¹Supplemental Material. Sample details, U-Pb geochronology data, EarthChem Database references, Lu-Hf data, oxygen isotope data, zircon saturation temperature data, and assimilation-fractional crystallization modeling. Please visit <https://doi.org/10.1130/GEOS.S.19090274> to access the supplemental material, and contact editing@geosociety.org with any questions.

log of a previously undocumented ~ 1.2 -km-tall SMO section in a side canyon of the 1.5-km-deep Barranca de Rio Guerachi, west of Guachochi (Figs. 1 and 2); this section is exemplary of geology in the previously under-explored Parral-Guachochi-Guadalupe y Calvo region and the northern and central SMO generally (e.g., Swanson et al., 2006; Murray et al., 2013).

The base of the SMO is unconformable on Eocene (?) andesites and late Cretaceous (?) granite. In this section, the lower third of the SMO is composed of >500 m of silicic lavas and volcanic breccias, with minor debris flow deposits and sandstones. The middle ~ 650 m is composed of horizontal, ~ 40 – 120 -m-thick ignimbrites separated by rare, thin, and altered fall deposits and paleosols. The lower units are weakly to moderately welded, lithic-rich lapilli tuffs. The two uppermost ignimbrites are very strongly welded with small fiamme and few lithic clasts; the informally named “San Miguel Arcangel” ignimbrite (Fig. 4) is weakly rheomorphic at its base and has a prominent basal vitrophyre. The uppermost ~ 350 m contains several welded dacitic ignimbrites, interbedded felsic volcaniclastic layers with paleosols, and ~ 150 m of felsic and andesitic breccias. The top ~ 50 m is a sequence of mafic lavas. To the best of our knowledge, this is the first detailed description and sampling of such a thick stratigraphic section in the SMO.

Petrology

All central transect samples and a small number of archived samples from the northern and southern transects were available for whole-rock and petrographic analysis. Additionally, several archived samples have published data and descriptions available. All but five units are rhyolites, one of which is peralkaline (Acantilado tuff; CH97-7); the others are rhyodacites (3-71-2, SMO15_11, and _52), dacite (SMO15_10), and latite (SMO15_41). The rhyolites are typically 10%–50% phyrlic with $\leq 30\%$ lithic fragments, and a typical crystal assemblage of plagioclase-quartz-biotite, \pm alkali feldspar, \pm hornblende. The groundmass is usually thoroughly devitrified to a cryptocrystalline mass of interlocking quartz and albite. Plagioclase, biotite, and hornblende are usually subhedral, broken crystals; many plagioclases are sieve-textured. Quartz content is highly variable within each sample, and all quartz crystals are anhedral and often embayed. Hydrothermal alteration is pervasive in many samples with sericitized feldspars, chlorite replacement of amphibole, and vesicles filled with chalcedony.

U/Pb Geochronology

Zircon crystals are characteristically euhedral and oscillatory zoned and typically vary from 50–150 μm in length (e.g., Fig. 3). Anhedral, metamict cores are very rare. Melt inclusions are often abundant (>5 per crystal) and are typically subparallel to the crystal margins. No anhedral or rounded, strongly embayed, or metamict crystals were recovered.

U-Pb age data are presented in Figure 5. $^{206}\text{Pb}/^{238}\text{U}$ zircon crystallization ages ($n = 578$) were determined to constrain ϵ_{Hf_t} values and mean square of

TABLE 1. SUMMARY OF MEAN AGE AND ISOTOPIC VALUES FOR SAMPLES FROM THE NORTHERN, CENTRAL, AND SOUTHERN TRANSECTS

Sample	Rock type and name	Latitude (°N)	Longitude (°W)	U/Pb mean weighted age			Hf		δ ¹⁸ O ‰ _{VSMOW}			Published Ar age		References			
				n	²⁰⁶ Pb/ ²³⁸ U age (Ma)	±95% confidence (Ma)	MSWD	n	εHf _t	±1σ (ε)	n	δ ¹⁸ O _{ZrC} (‰)	±1σ (‰)		δ ¹⁸ O _{qtz} (‰)	Ar age (Ma)	±2σ (Ma)
Northern Transect*																	
3-20-4	Unnamed rhyolite tuff	28.3303	108.7094	18	21.44	0.20	3.1	1	+0.5	–	9	5.80	0.40	–	23.3 ¹⁵	2.2	9
BM100305-2	Unnamed rhyolite lava	27.3080	108.2373	3	21.24	1.19	2.3	–	–	–	8	6.40	0.20	–	–	–	12
BM100307-1	Cerro Salitrera rhyolite plug	27.3682	108.2579	5	21.70	0.39	5.3	4	+1.8	0.7	9	6.60	0.20	–	–	–	12
CH01	Gallego rhyolite Lava and/or lava-like tuff	29.5366	106.3141	13	37.44	0.24	3.5	9	–2.6	0.9	9	6.70	0.40	–	37.77 ¹¹	0.1	10, 11
CH03	Bellavista rhyolite tuff	29.0813	106.3866	12	45.57	0.29	7.8	8	+2.1	1.1	11	5.50	0.20	8.89	Ca. 48–46 ¹⁰	–	7, 10
CH06	Vista Tuff	28.2611	108.0665	29	32.22	0.13	4.5	13	+0.2	0.9	–	–	–	8.97	33.37 ¹¹	0.4	3, 4, 6, 11
CH88-13	Chivato rhyolite tuff	28.4684	106.3008	27	41.26	0.25	4.9	15	+0.7	1.2	10	6.10	0.20	–	~42–40 ¹⁷	2.4–1.0	7, 9
CH88-17	Sierra del Nido rhyolite lava	29.5232	106.5813	19	37.23	0.21	5.3	8	–4.1	1.4	10	6.80	0.20	–	~38–36 ¹⁷	0.8–0.6	7
CH97-7	Acantilado peralkaline rhyolite tuff	29.0867	106.4816	15	30.39	0.17	5.3	15	+0.5	1.2	10	6.80	0.20	9.71	29.99 ¹¹	0.11	11
CUSI	Unnamed rhyolite tuff	28.2137	106.7915	18	36.78	0.21	3.4	12	+0.6	1.3	12	6.60	0.30	–	~37–35 ¹⁷	1.1–0.6	7, 9
J406	Bufa rhyolite tuff	28.2274	106.8355	16	39.83	0.17	5.0	10	+3.0	0.7	9	6.80	0.10	–	–	–	9, 10, 11
MAJ	Majalca Canyon rhyolite tuff	28.8210	106.4374	14	42.21	0.25	2.0	8	+0.2	1.0	7	6.00	0.20	–	45.11 ¹¹	0.15	7, 11
N-12	Quemada rhyolite tuff	27.5330	107.7954	8	31.13	0.33	5.4	3	+2.6	0.9	15	6.30	0.30	–	–	–	8
N-63	Unnamed felsic lava	28.0075	107.7942	3	29.95	0.59	4.9	2	+3.4	0.9	5	5.80	0.30	–	29.4 ¹⁸	0.5	8
N-88	Quemada rhyolite tuff	28.1574	107.4484	4	29.29	0.39	6.8	2	+3.6	1.7	8	6.30	0.20	–	–	–	8
N-99	Copper Canyon rhyolite tuff	27.5316	107.7933	18	29.93	0.22	6.9	8	+4.6	1.0	8	6.40	0.20	9.29	29.62 ¹⁸	0.32	8
RED	Canada de Gato rhyolite lava	28.4248	106.2910	16	39.53	0.17	8.5	9	+1.8	0.6	8	5.80	0.30	–	40.85 ¹¹	0.13	9, 11
SJ-3	San Felipe rhyolite tuff	28.0090	107.7030	10	32.90	0.26	3.1	1	+1.5	–	10	6.10	0.20	–	36.5 ¹⁶	3.2	6, 8, 9
SJ-42	Divisadero tuff	27.7303	107.7030	23	28.98	0.13	5.7	5	+4.5	1.2	–	–	–	–	29.9 ¹⁸	0.7	8
SJ-50	Cerro de la Luna rhyolite lava	28.0253	107.6926	10	29.22	0.15	3.1	4	+3.9	0.6	10	6.00	0.10	–	–	–	8
SJ-54	Unnamed rhyolite lava	28.1420	107.5033	12	33.62	0.17	5.0	3	+3.7	0.4	8	6.20	0.40	9.32	–	–	8
Southern Transect*																	
1-70-1	Las Adjuntas rhyolite dome	23.7506	105.5118	2	26.95	0.33	1.0	–	–	–	9	6.60	0.20	–	~28–27 ¹¹	–	1
2-71-1	Santaurio tuff	24.0409	104.6683	20	30.33	0.15	4.4	1	+2.3	–	–	–	–	9.55	31.67 ¹¹	0.09	1, 2
3-71-2	El Salto rhyodacite tuff	23.7900	105.3700	11	24.84	0.14	4.5	3	+3.7	1.9	9	6.10	0.10	–	24.0 ¹¹	0.05	1, 2, 11
3-71-7	“plateau units”	23.6584	105.7403	13	23.79	0.21	3.6	–	–	–	7	6.30	0.20	–	~24–23 ¹¹	–	1
K-LP-T	Aguilla rhyolite tuff	24.0088	104.3970	19	32.56	0.15	9.3	5	–3.1	0.9	10	6.80	0.30	10.23	31.46 ¹¹	0.07	2, 11
SL-41	Agua Nueva dome	25.3496	104.1521	4	45.15	0.74	3.2	–	–	–	10	6.70	0.70	10.81	~45.6 ¹⁵	–	5

(continued)

TABLE 1. SUMMARY OF MEAN AGE AND ISOTOPIC VALUES FOR SAMPLES FROM THE NORTHERN, CENTRAL, AND SOUTHERN TRANSECTS (continued)

Sample	Rock type and name	Latitude (°N)	Longitude (°W)	U/Pb mean weighted age			Hf		δ ¹⁸ O ‰ _{VSMOW}			Published Ar age		References			
				n	²⁰⁶ Pb/ ²³⁸ U age (Ma)	±95% confidence (Ma)	MSWD	n	εHf _t	±1σ (ε)	n	δ ¹⁸ O _{Zrc} (‰)	±1σ (‰)		δ ¹⁸ O _{Qtz} (‰)	Ar age (Ma)	±2σ (Ma)
Central Transect⁶																	
SMO13_03	Cerro El Caracol rhyolite lava	26.0830	106.9397	15	41.07	1.25	0.1	10	+1.5	0.6	12	6.59	0.14	–	40.60 ¹³	0.13	14
SMO13_10	La Joya rhyolite lava	26.1018	106.7313	14	31.65	0.72	1.7	10	+1.7	1.4	–	–	–	–	30.31 ¹³	0.17	14
SMO13_17	Unnamed rhyolite lava	26.2339	106.5353	12	35.70	0.68	3.5	4	+0.8	1.9	–	–	–	–	31.47 ¹³	0.13	14
SMO13_27	Unnamed rhyolite lava	26.5352	106.3478	14	30.84	0.53	0.6	13	+3.4	2.1	–	–	–	–	31.79 ¹³	0.38	14
SMO15_01	Unnamed rhyolite tuff	26.9755	106.3422	15	33.77	1.08	0.2	11	+4.4	1.5	13	6.42	0.27	–	31.53 ¹³	0.12	14
SMO15_06	Unnamed rhyolite plug	26.8726	106.9798	16	33.07	0.70	0.2	8	+2.6	1.0	9	6.78	0.44	–	30.13 ¹³	–	14
SMO15_09	Unnamed rhyolite tuff	26.6934	107.3167	13	33.63	0.77	0.6	8	+3.5	2.1	10	7.01	0.45	–	31.46 ¹³	0.07	14
SMO15_10	Unnamed quartz-latite tuff	26.6934	107.3167	16	32.34	0.58	1.5	6	+4.0	1.2	–	–	–	–	31.72 ¹³	0.12	14
SMO15_11	Unnamed rhyodacite tuff	26.7285	107.3071	14	31.21	0.60	0.6	9	+2.6	1.2	1	7.25	–	–	–	–	14
SMO15_14	San Miguel Arcangel rhyolite tuff	26.7145	107.3138	13	29.50	0.61	0.4	8	+2.6	1.3	–	–	–	–	–	–	14
SMO15_17	Unnamed rhyolite tuff	26.7285	107.3071	12	32.19	1.33	0.2	10	+1.9	1.4	10	6.84	0.32	–	29.26 ¹³	0.06	14
SMO15_23	Unnamed rhyolite lava	26.8465	106.8198	15	30.10	0.54	1.2	11	+1.1	1.3	–	–	–	–	30.44 ¹³	0.16	14
SMO15_32	Unnamed rhyolite tuff	26.9460	106.4792	14	32.72	0.80	0.6	8	+1.5	1.5	10	7.44	0.66	–	–	–	14
SMO15_35	Unnamed rhyolite tuff	26.9603	106.4186	14	34.61	0.52	0.6	8	+0.3	0.6	–	–	–	–	–	–	14
SMO15_37	Unnamed rhyolite tuff	26.8653	106.2717	14	32.17	0.77	0.1	10	+1.4	1.2	16	6.45	0.27	–	–	–	14
SMO15_41	Unnamed latite lava	26.8807	106.2625	15	38.57	1.06	0.1	10	+3.2	1.0	14	6.21	0.46	–	39.33 ¹³	0.50	14
SMO15_42	Unnamed rhyolite tuff	26.8951	106.2460	15	33.26	0.52	0.6	10	–0.1	1.0	–	–	–	–	32.11 ¹³	0.11	14
SMO15_44	Unnamed rhyolite lava	26.8893	106.2428	15	35.02	0.71	0.8	7	–0.1	1.4	–	–	–	–	30.86 ¹³	0.12	14
SMO15_46	Unnamed rhyolite tuff	26.8747	106.2244	13	27.27	0.57	0.9	11	–1.2	1.9	13	6.54	0.90	–	31.43 ¹³	0.16	14
SMO15_49	Unnamed rhyolite tuff	26.8582	106.1178	14	33.11	0.56	0.8	10	+0.1	0.6	–	–	–	–	–	–	14
SMO15_52	Los Baños rhyodacite tuff	26.7205	106.2375	15	25.85	0.92	3.2	11	–0.8	2.6	12	6.96	0.79	–	–	–	14
SMO15_55	Unnamed rhyolite tuff	27.0684	106.2536	15	34.62	0.52	0.6	8	+0.6	0.7	–	–	–	–	–	–	14

Note: Dash indicates not measured.

*Analyzed at the University of Wisconsin (secondary ion mass spectrometry [SIMS]–δ¹⁸O_{Zrc} and laser fluorination–δ¹⁸O_{Qtz}) and Washington State University (laser ablation–inductively coupled plasma mass spectrometry [LA-ICPMS] split stream - U/Pb and Hf).

⁶Analyzed at the University of California Los Angeles (SIMS - U/Pb and δ¹⁸O_{Zrc}) and the University of Arizona (LA-ICPMS - Hf). VSMOW—Vienna standard mean ocean water.

¹K-Ar age.

⁴Ar-Ar age.

1—McDowell and Keizer (1977).

2—Swanson et al. (1978).

3—Swanson and McDowell (1985).

4—Wark et al. (1990).

5—Aguirre-Diaz and McDowell (1991).

6—Wark et al. (1991).

7—McDowell and Mauger (1994).

8—Swanson et al. (2006).

9—McDowell (2007).

10—Bryan et al. (2008).

11—McDowell and McIntosh (2012).

12—Murray et al. (2013).

13—Pack (2017).

14—This study.

Strat. log of Barranca Río Guerachi

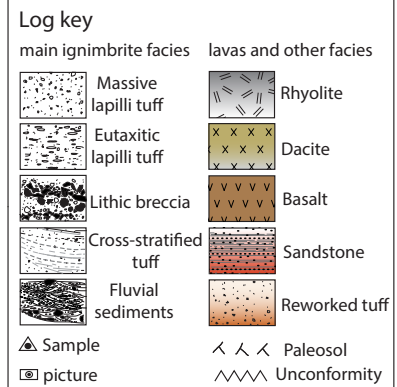
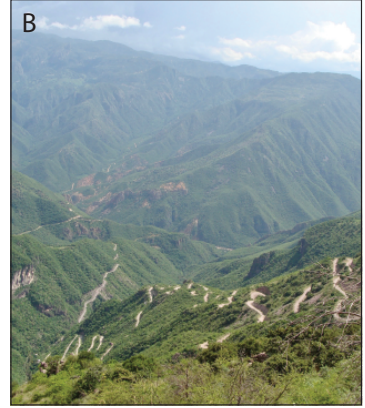
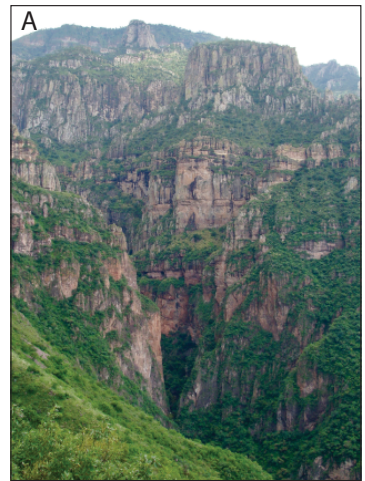
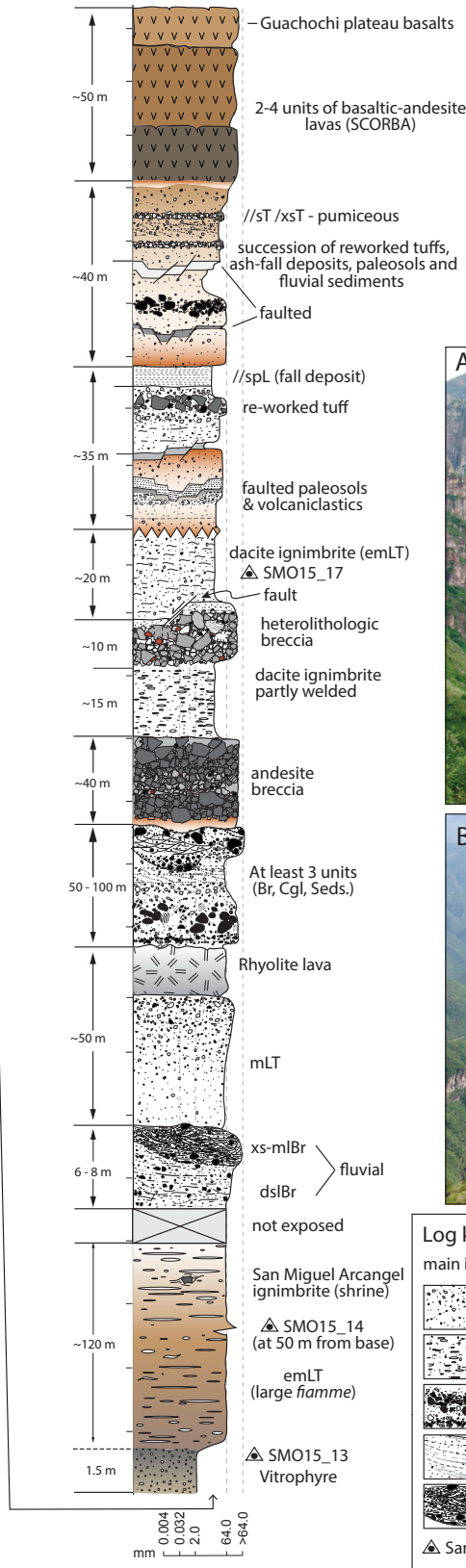
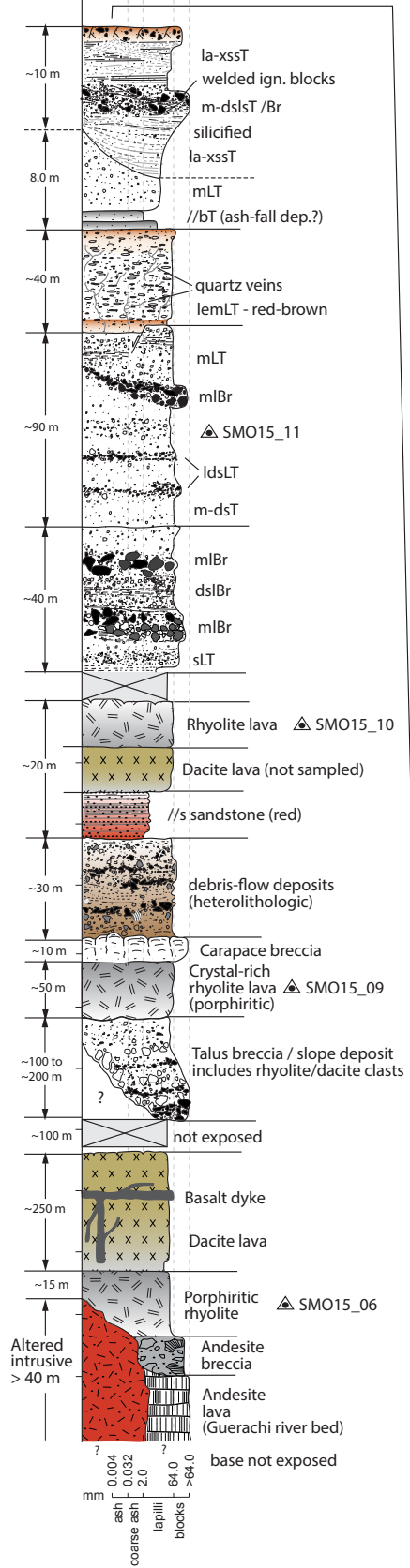
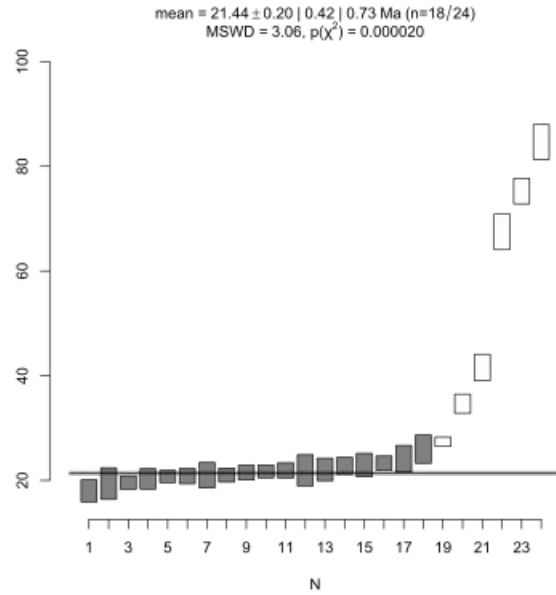
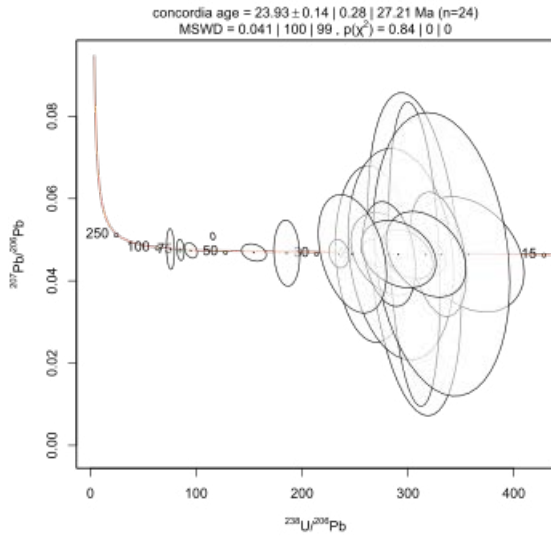
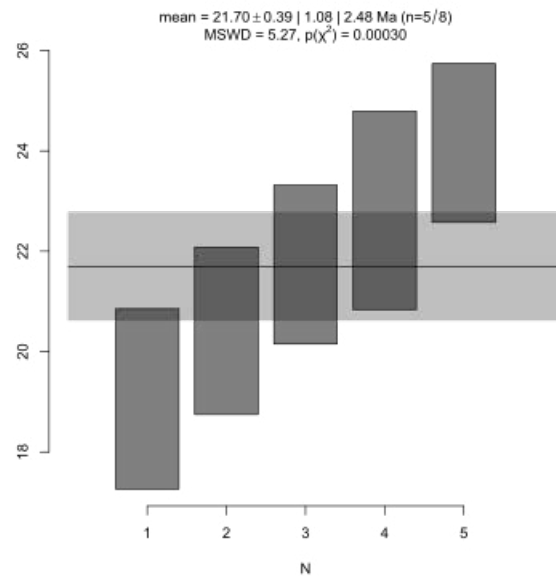
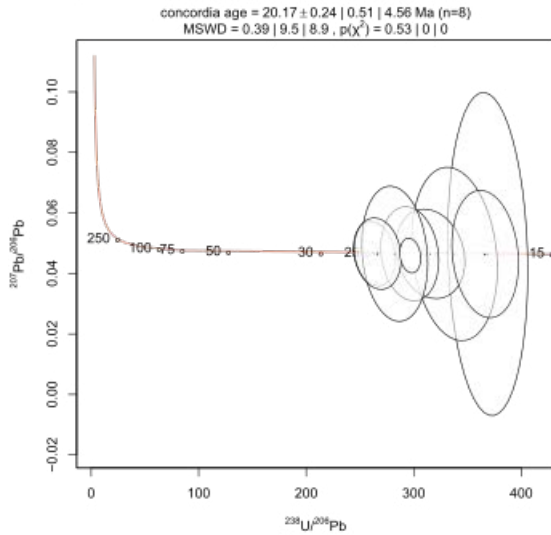


Figure 4. Lithological log of the Barranca de Río Guerachi section, Chihuahua. Inset: (A) view of the upper-half of the section with the “San Miguel Arcangel” ignimbrite at the base and the basalts of the Guachochi plateau at the top; and (B) view south across the Barranca de Río Guerachi with the Sierra Madre Occidental (SMO) plateau at Guadalupe y Calvo on the horizon. SCORBA—Southern Cordilleran basaltic andesite.

sample 3-20-4 -- 21.44 +/- 0.20 Ma



sample BM100307-1 -- 21.70 +/- 0.39 Ma



sample CH01 -- 37.44 +/- 0.53 Ma

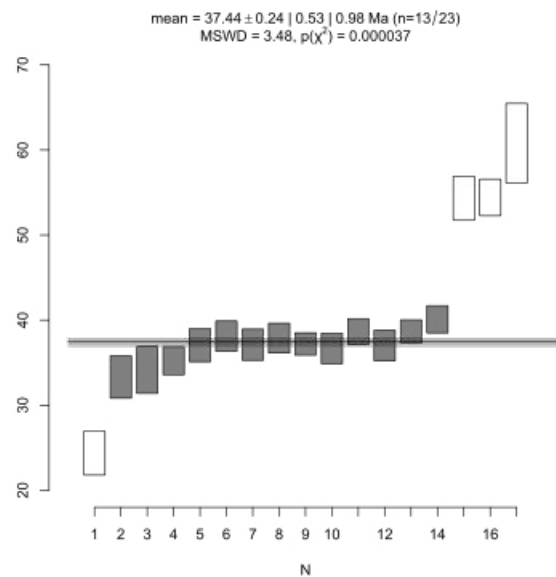
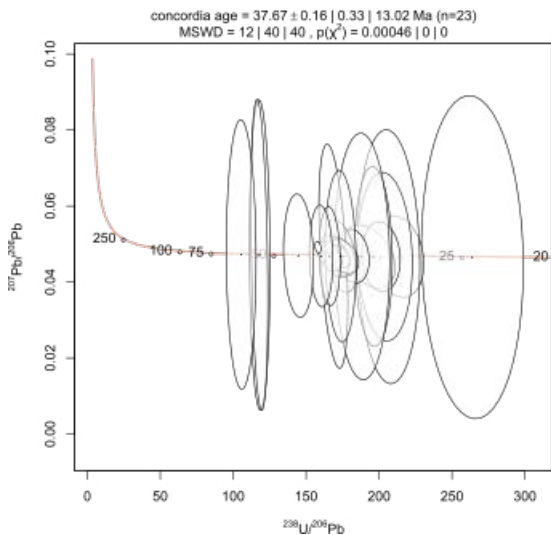
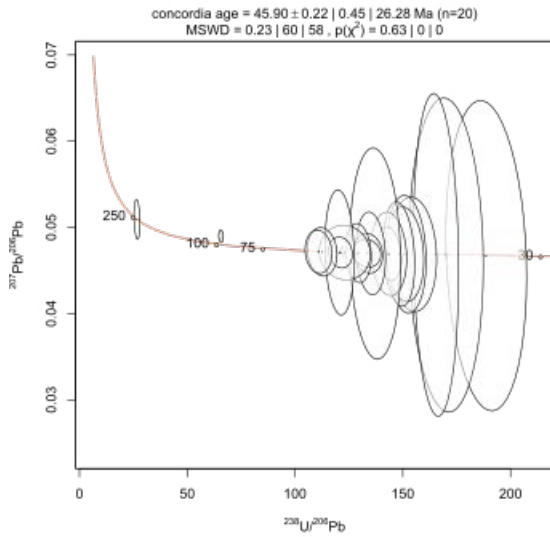
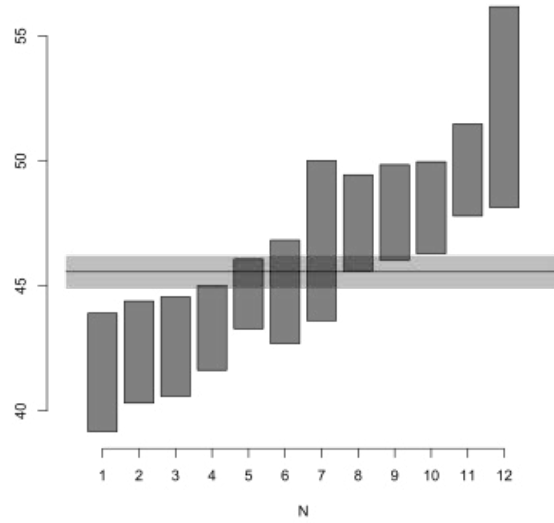


Figure 5. U-Pb data for each sample presented as Tera-Wasserburg concordia plots (left) and weighted mean average ages (right). (Continued on following 13 pages.)

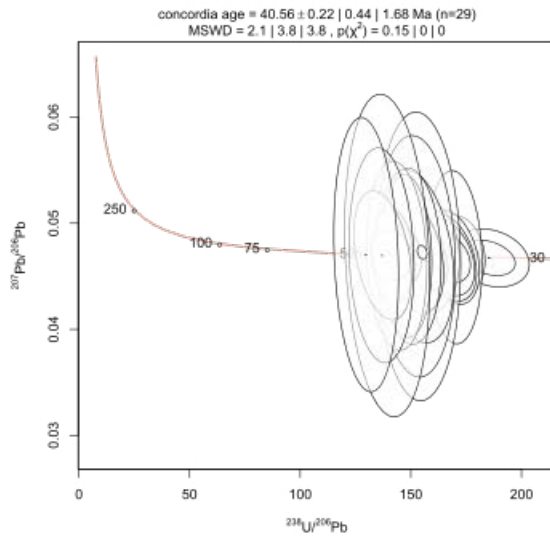
sample CH03 -- 45.57 +/- 0.29 Ma



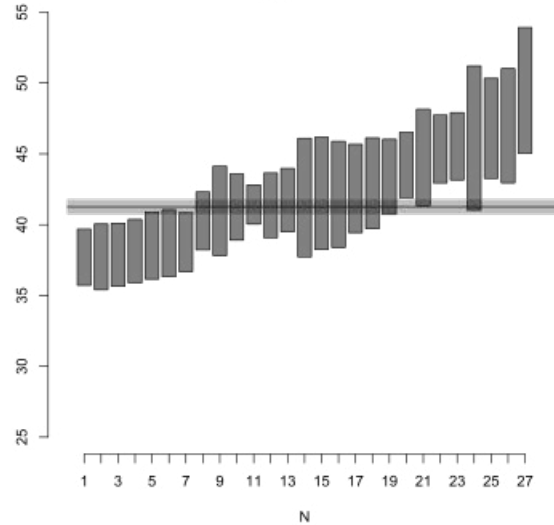
mean = 45.57 ± 0.29 | 0.64 | 1.79 Ma (n=12/20)
MSWD = 7.76, $p(\chi^2) = 0.000000000000014$



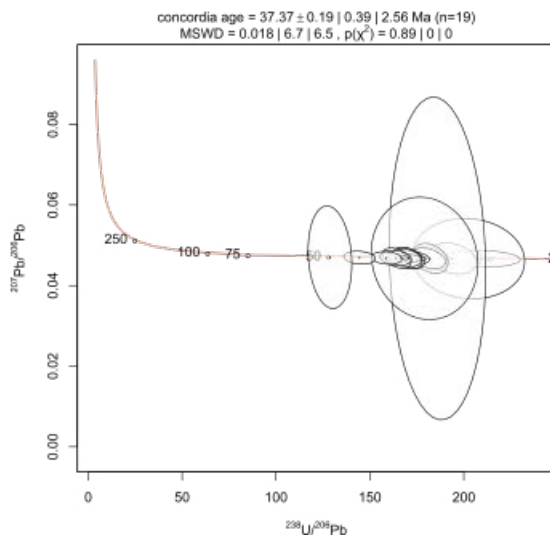
sample CH88-13 -- 41.26 +/- 0.25 Ma



mean = 41.26 ± 0.25 | 0.51 | 1.12 Ma (n=27/29)
MSWD = 4.85, $p(\chi^2) = 0.00000000000000040$



sample CH88-17 -- 37.23 +/- 0.21 Ma



mean = 37.23 ± 0.21 | 0.46 | 1.06 Ma (n=15/19)
MSWD = 5.30, $p(\chi^2) = 0.000000000000033$

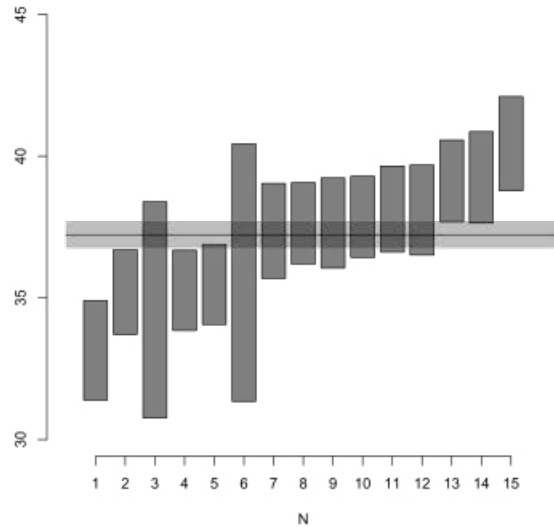
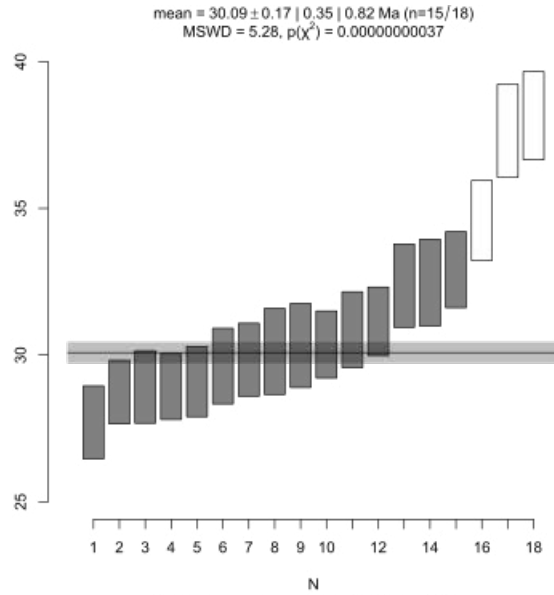
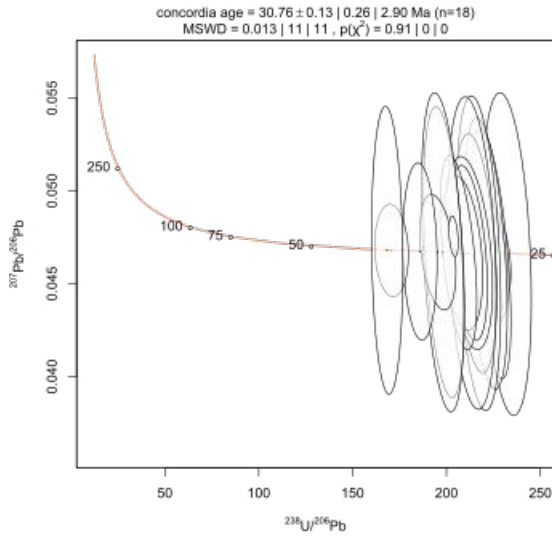
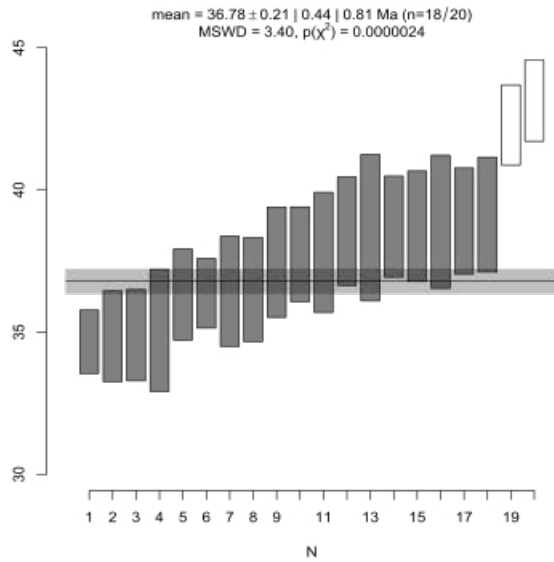
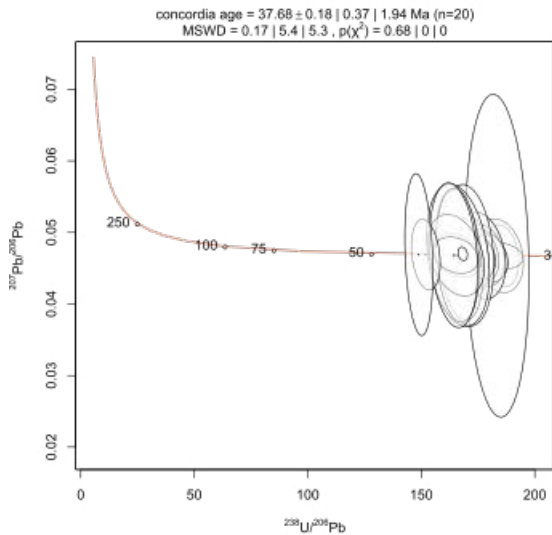


Figure 5. (Continued on following 12 pages.)

sample CH97-7 -- 30.09 +/- 0.17 Ma



sample CUSI -- 36.78 +/- 0.21 Ma



sample J406 -- 39.83 +/- 0.17 Ma

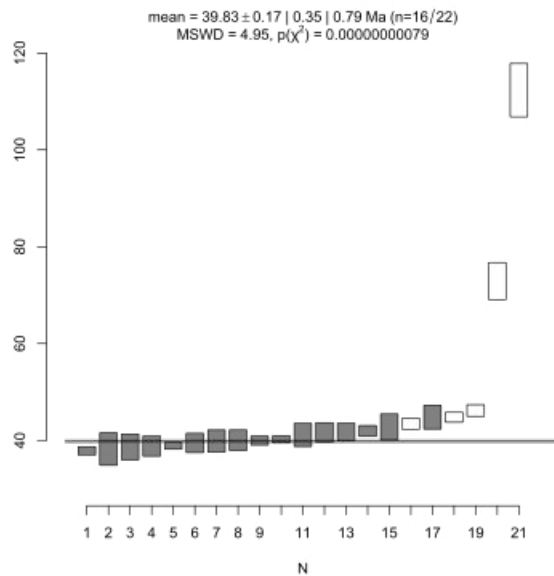
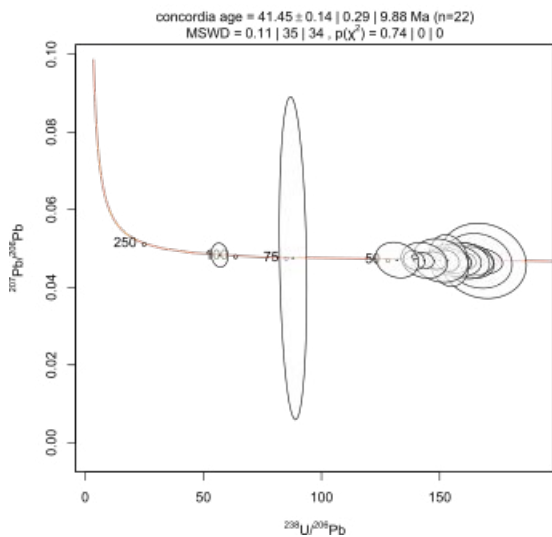
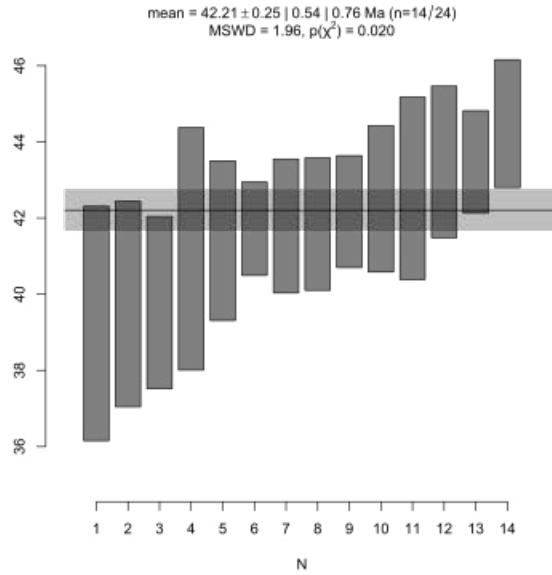
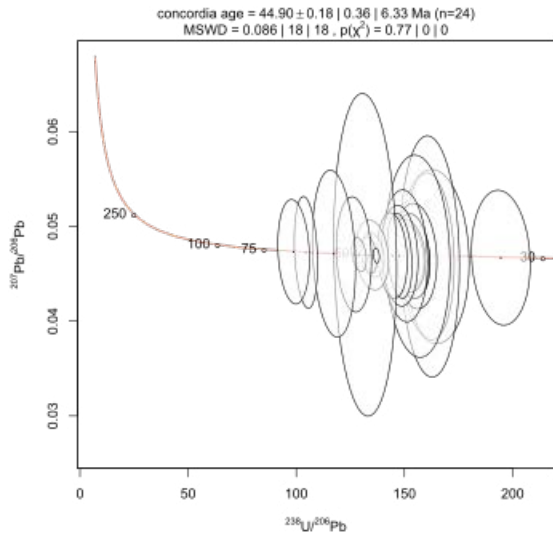
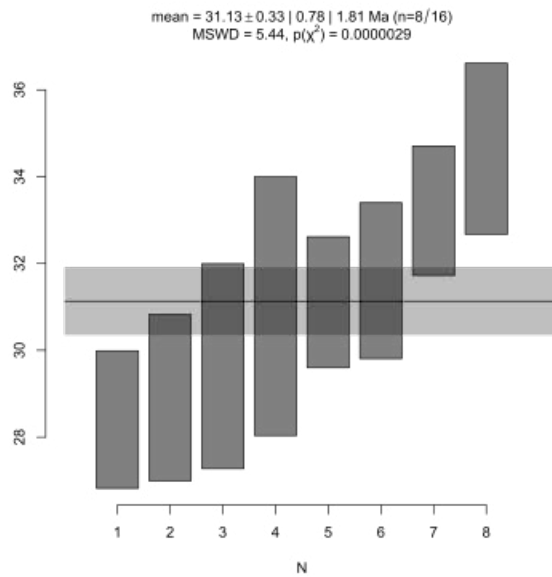
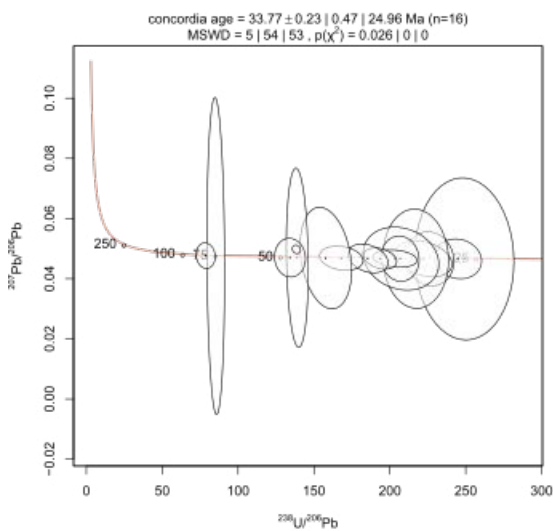


Figure 5. (Continued on following 11 pages.)

sample MAJ -- 42.21 +/- 0.25 Ma



sample N-12 -- 31.13 +/- 0.33 Ma



sample N-88 -- 29.29 +/- 0.39 Ma

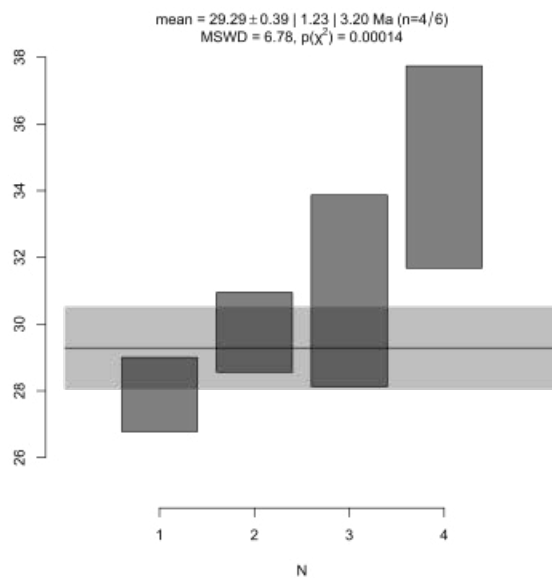
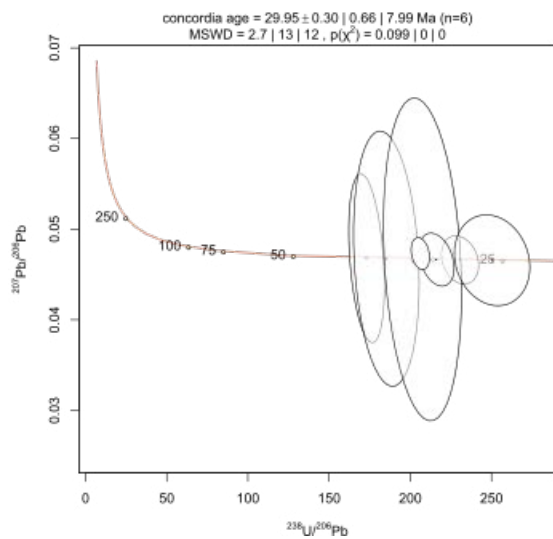
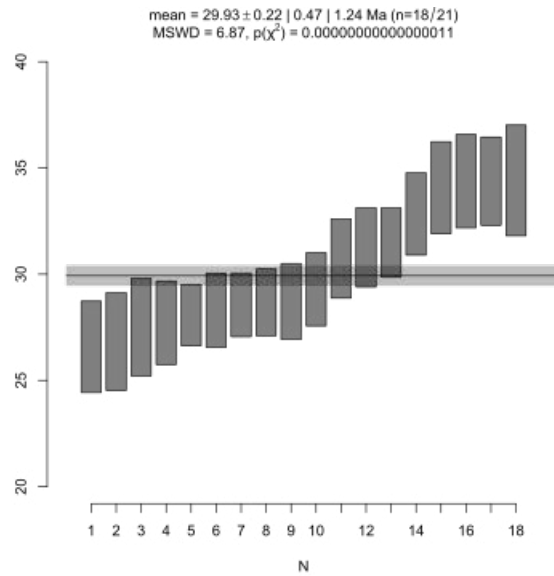
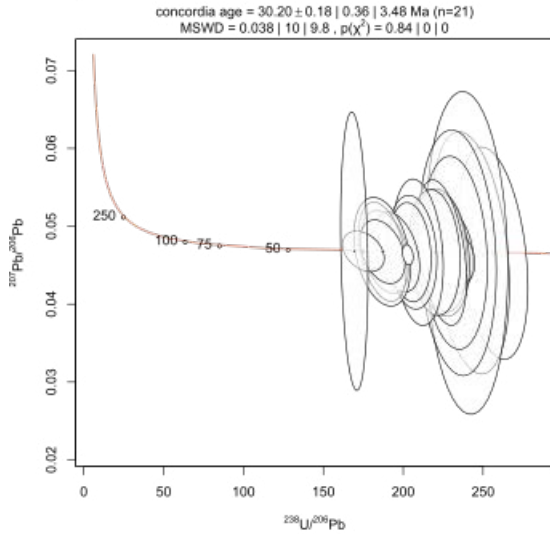
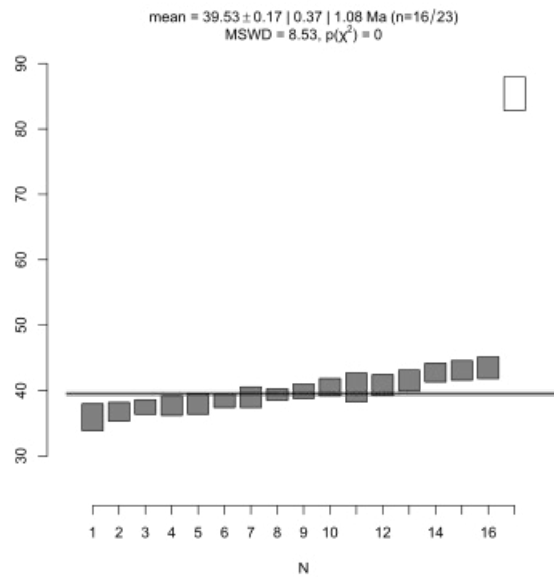
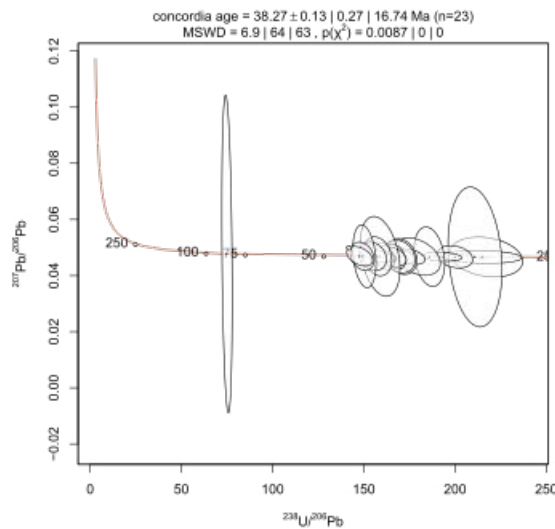


Figure 5. (Continued on following 10 pages.)

sample N-99 -- 29.93 +/- 0.22 Ma



sample RED -- 39.53 +/- 0.17 Ma



sample SJ-3 -- 32.90 +/- 0.26 Ma

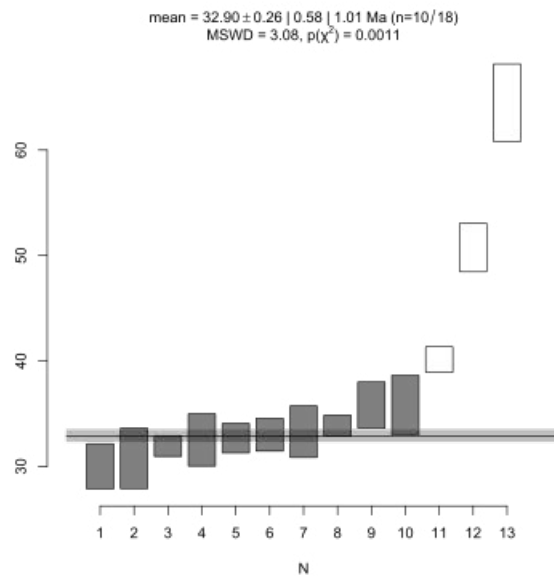
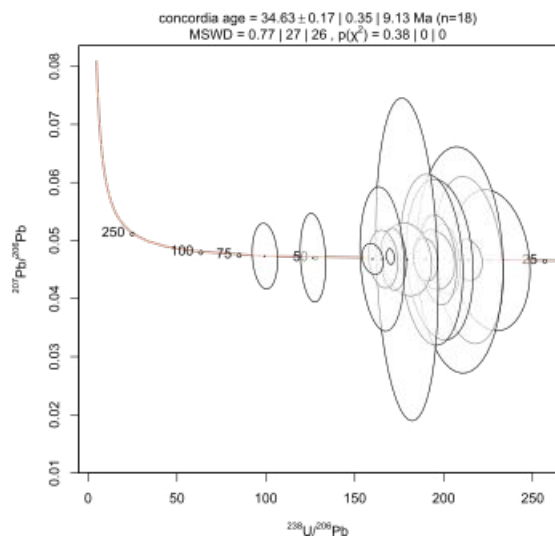
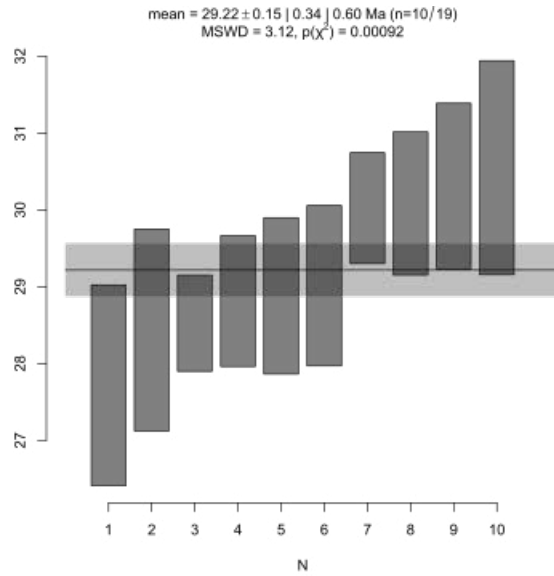
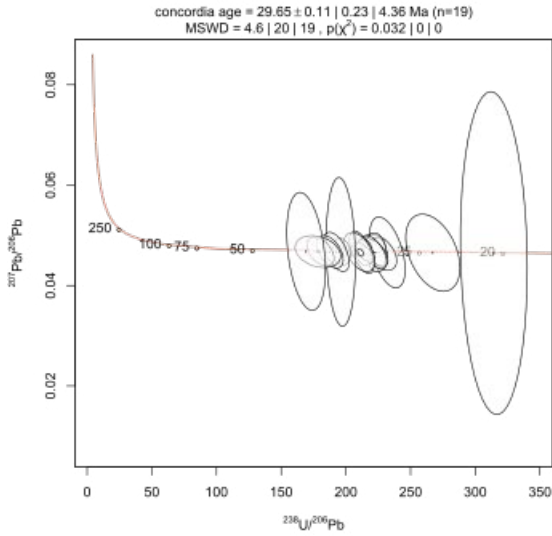
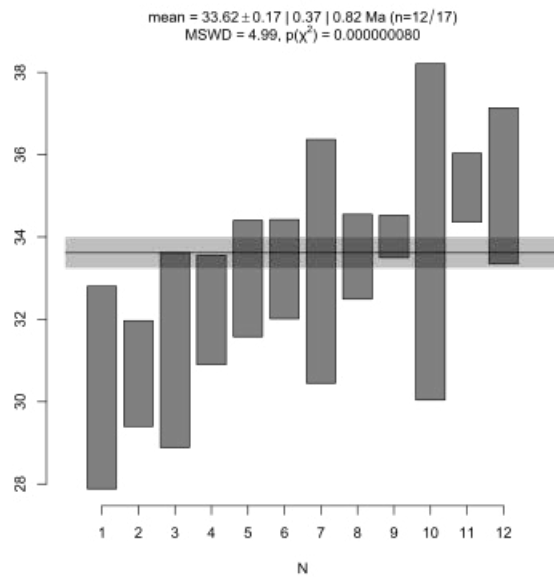
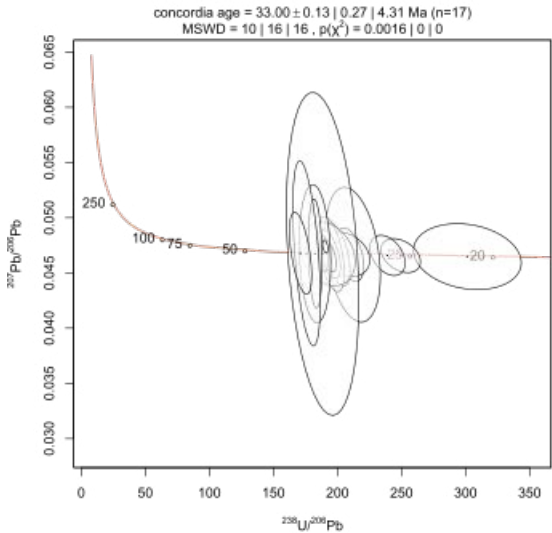


Figure 5. (Continued on following 9 pages.)

sample SJ-50 -- 29.22 +/- 0.15 Ma



sample SJ-54 -- 33.62 +/- 0.17 Ma



sample 3-71-2 -- 24.84 +/- 0.14 Ma

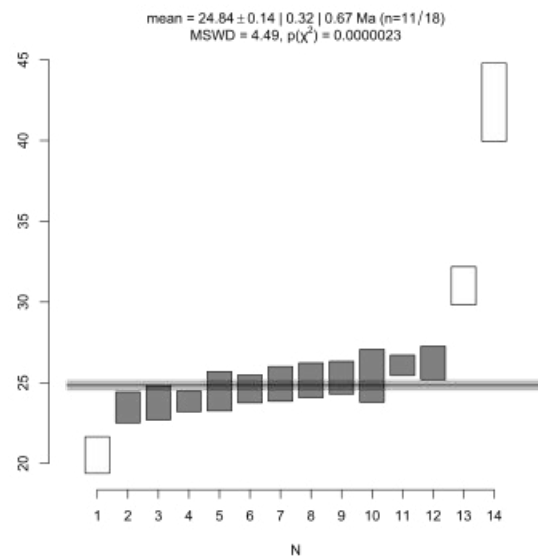
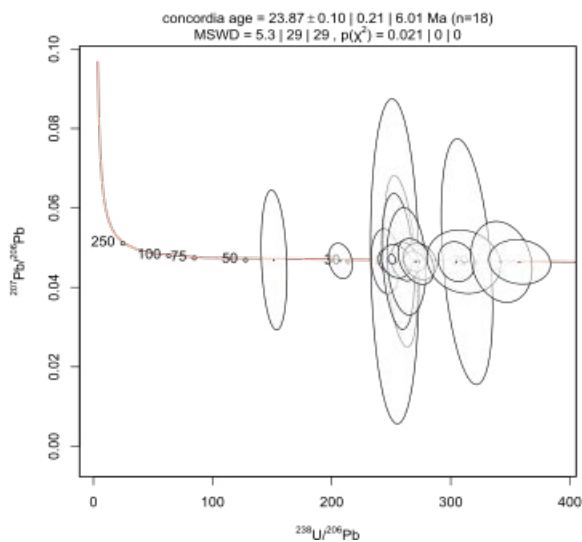
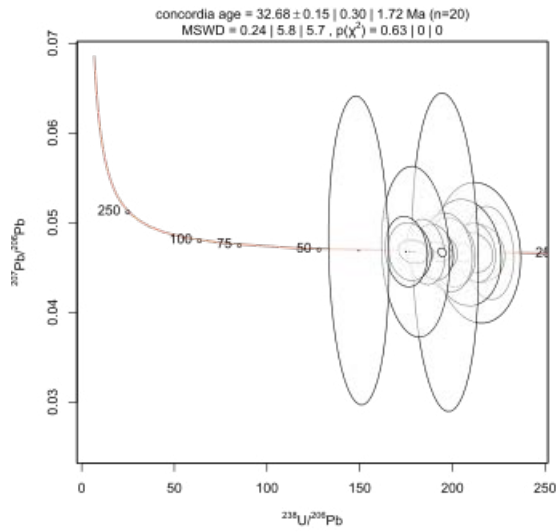
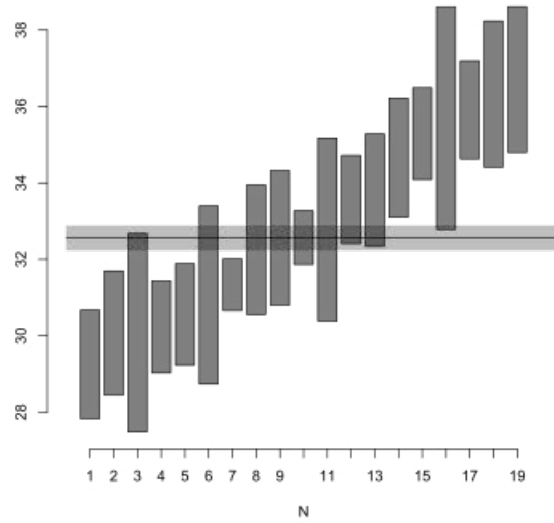


Figure 5. (Continued on following 8 pages.)

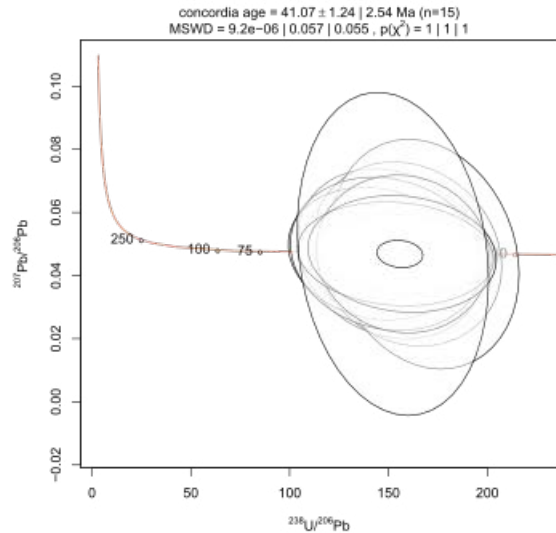
sample K-LP-T -- 32.56 +/- 0.15 Ma



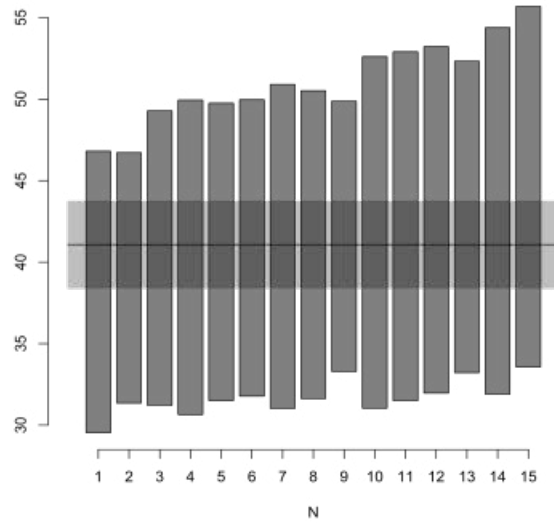
mean = $32.56 \pm 0.15 | 0.32 | 0.98$ Ma (n=19/20)
MSWD = 9.27, $p(\chi^2) = 0$



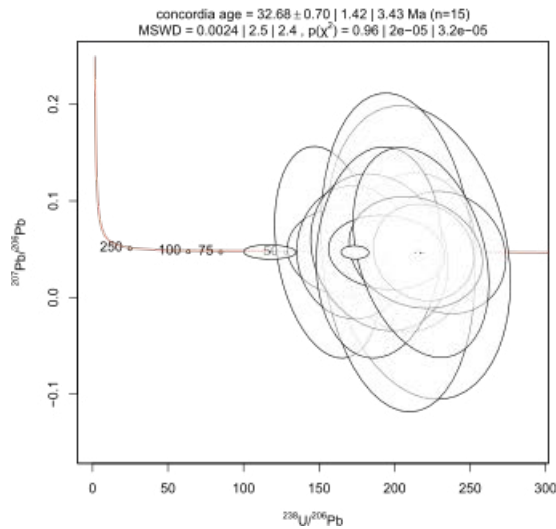
sample SMO13_03 -- 41.07 +/- 1.25 Ma



mean = $41.07 \pm 1.25 | 2.68 | 0.90$ Ma (n=15/15)
MSWD = 0.11, $p(\chi^2) = 1.00$



sample SMO13_10 -- 31.65 +/- 0.72 Ma



mean = $31.65 \pm 0.72 | 1.56 | 2.04$ Ma (n=14/15)
MSWD = 1.72, $p(\chi^2) = 0.050$

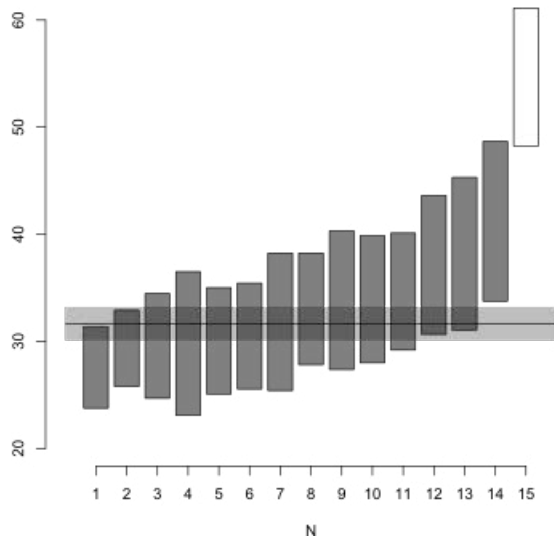
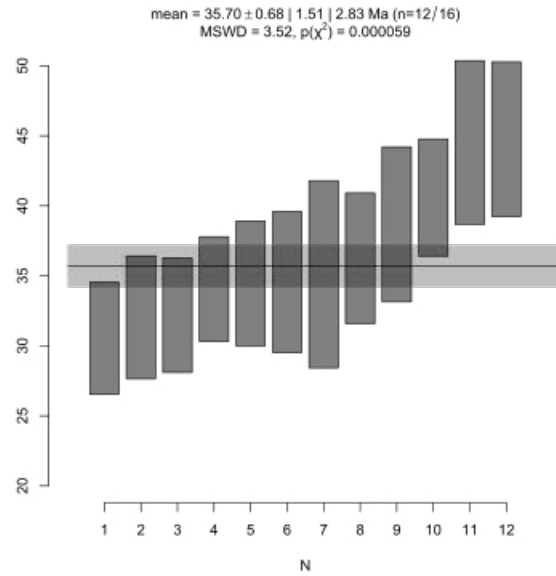
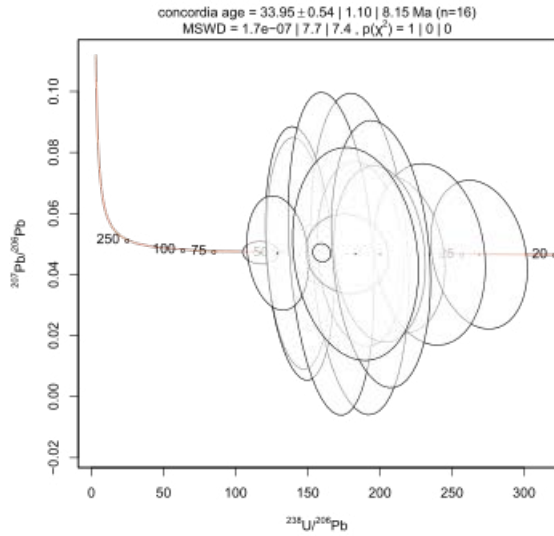
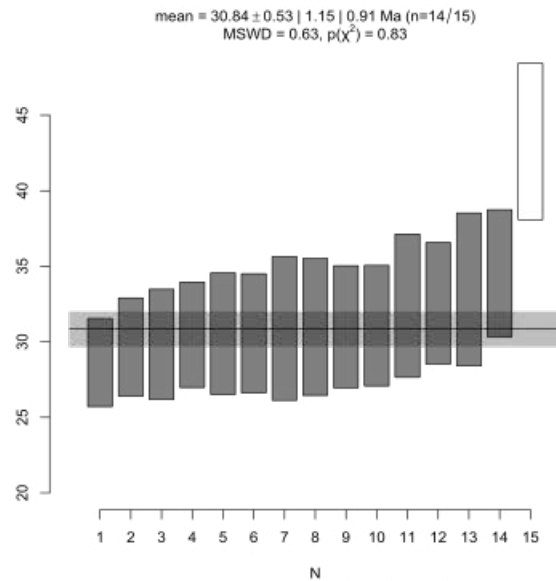
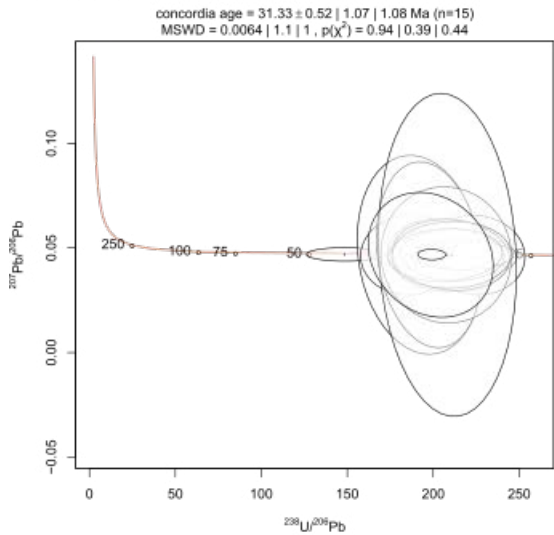


Figure 5. (Continued on following 7 pages.)

sample SMO13_17 -- 35.70 +/- 0.68 Ma



sample SMO13_27 -- 30.84 +/- 0.53 Ma



sample SMO15_01 -- 33.77 +/- 1.08 Ma

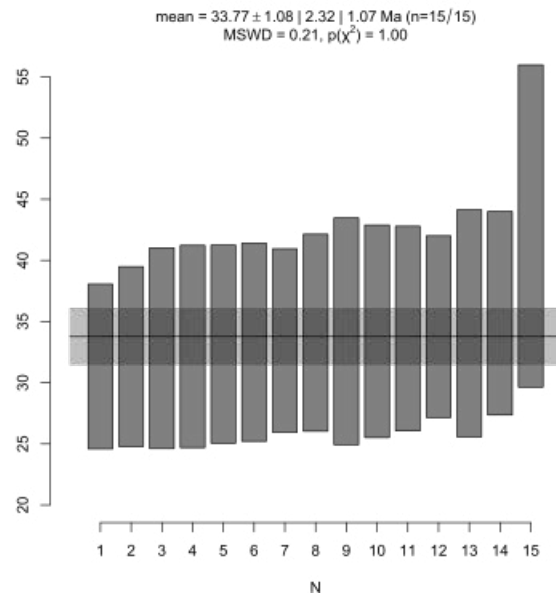
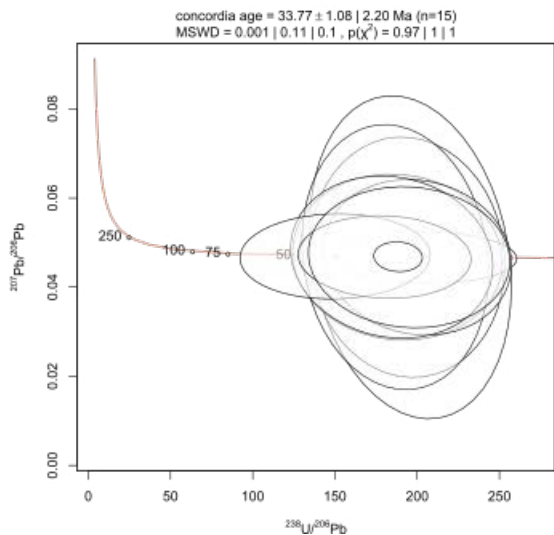
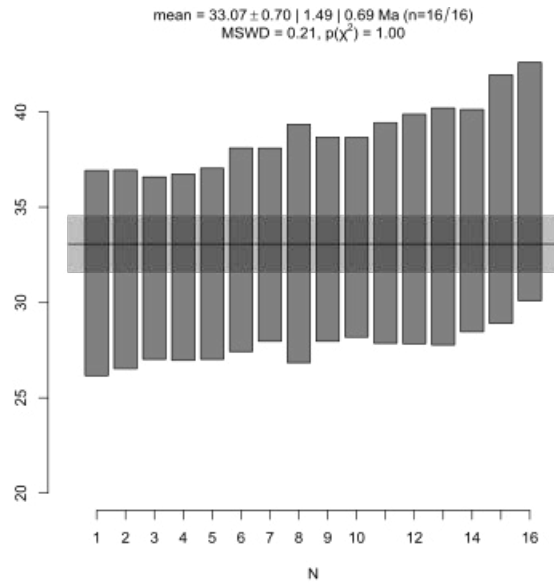
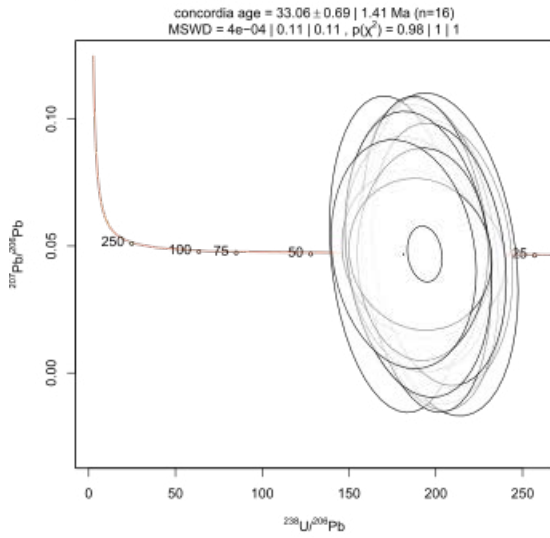
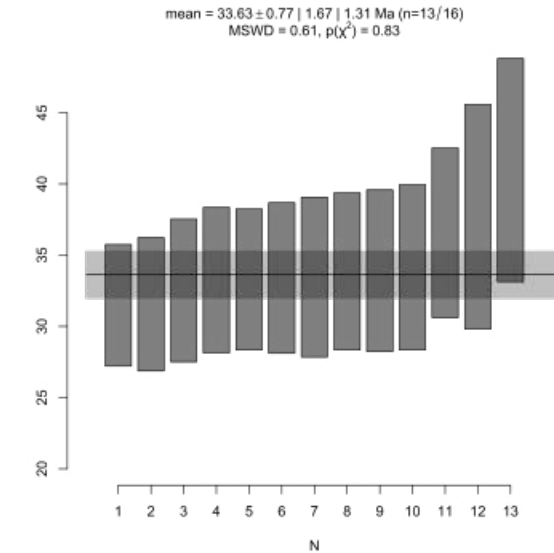
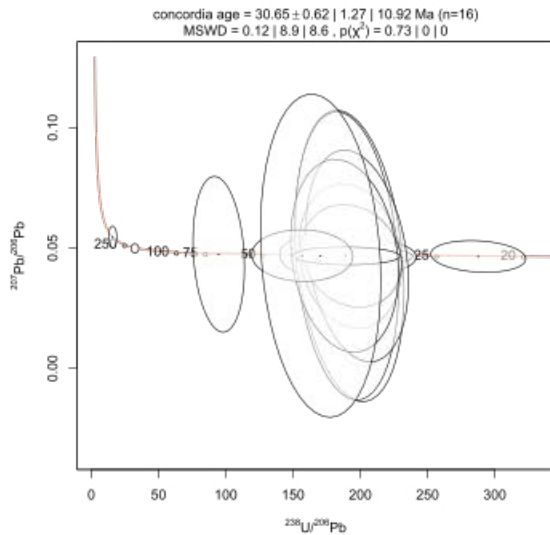


Figure 5. (Continued on following 6 pages.)

sample SMO15_06 -- 33.07 +/- 0.70 Ma



sample SMO15_09 -- 33.63 +/- 0.77 Ma



sample SMO15_10 -- 32.34 +/- 0.58 Ma

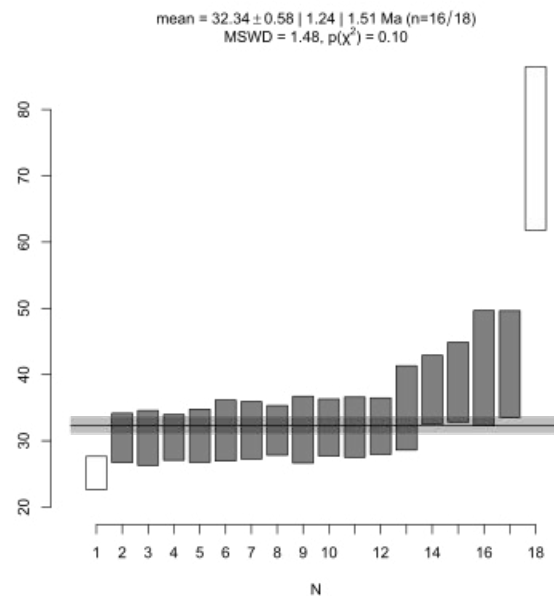
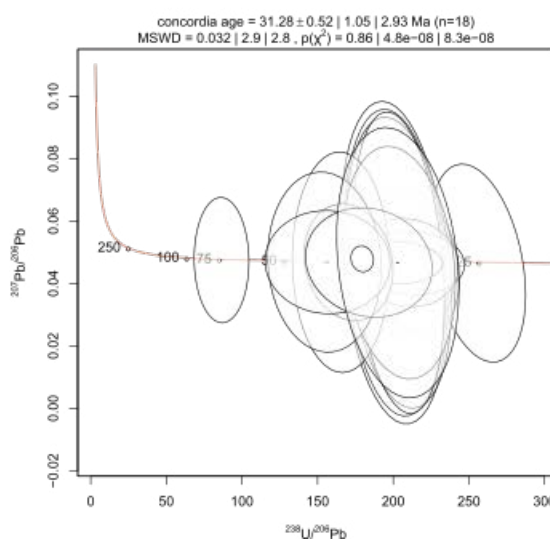
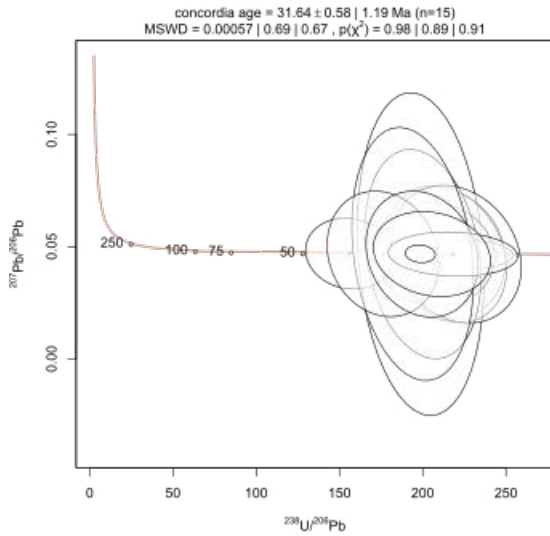
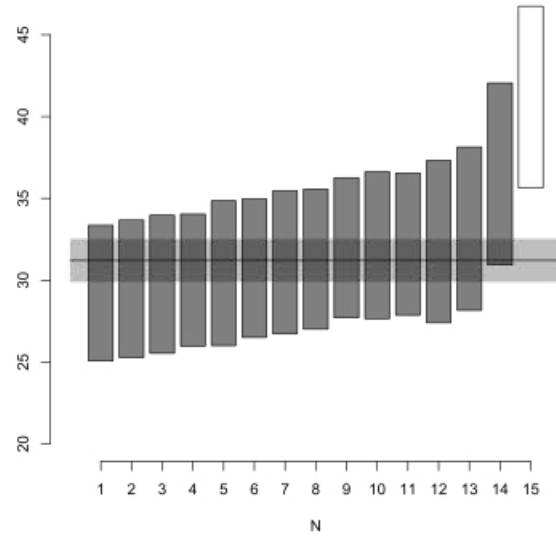


Figure 5. (Continued on following 5 pages.)

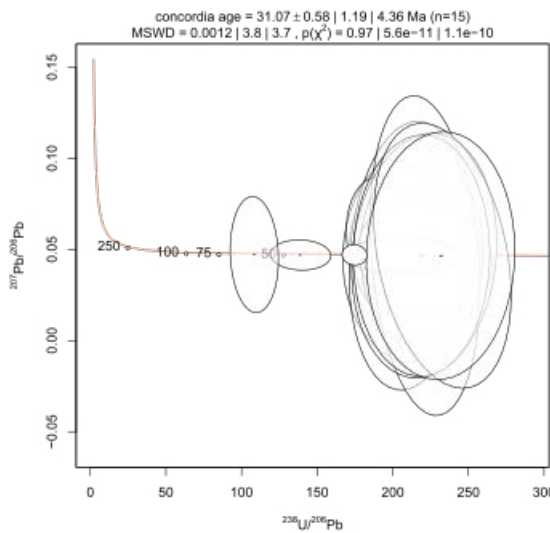
sample SMO15_11 -- 31.21 +/- 0.60 Ma



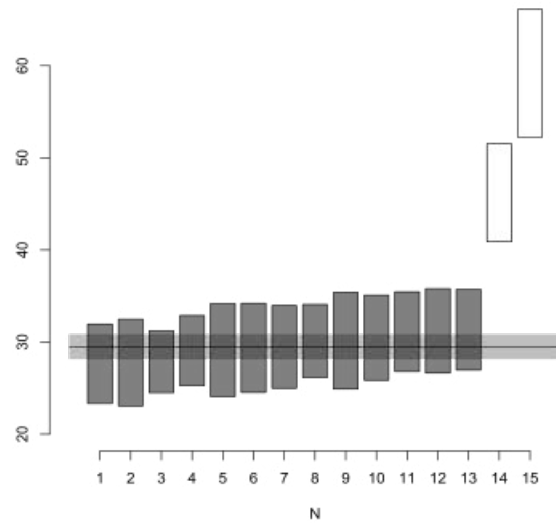
mean = 31.21 ± 0.60 | 1.30 | 0.97 Ma (n=14/15)
MSWD = 0.56, $p(\chi^2) = 0.89$



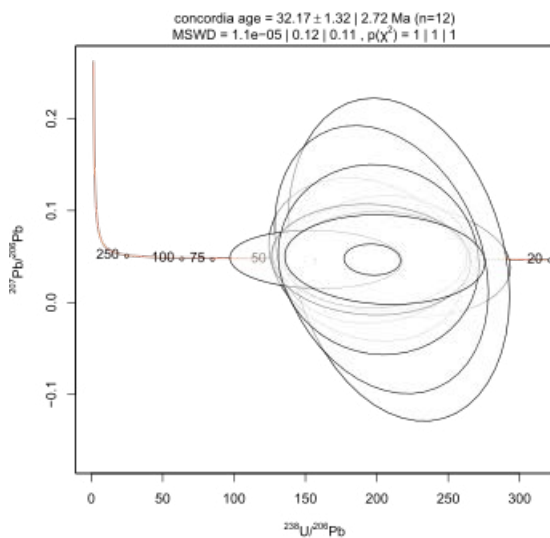
sample SMO15_14 -- 29.50 +/- 0.61 Ma



mean = 29.50 ± 0.61 | 1.34 | 0.80 Ma (n=13/15)
MSWD = 0.36, $p(\chi^2) = 0.98$



sample SMO15_17 -- 32.17 +/- 1.32 Ma



mean = 32.19 ± 1.33 | 2.93 | 1.41 Ma (n=12/12)
MSWD = 0.23, $p(\chi^2) = 1.00$

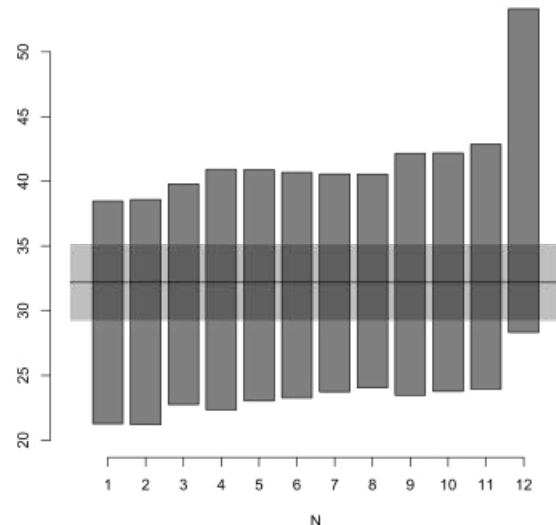
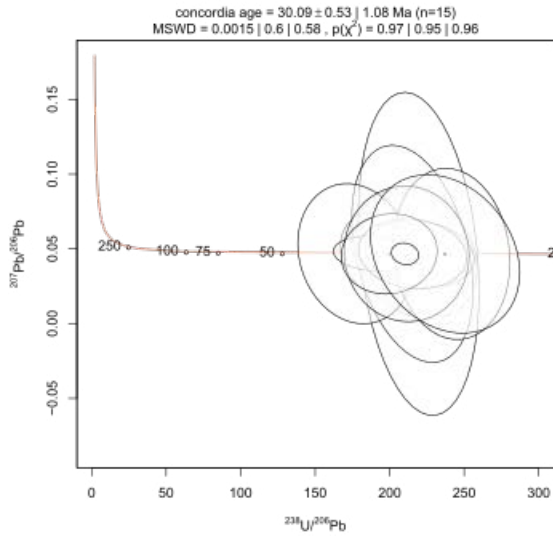
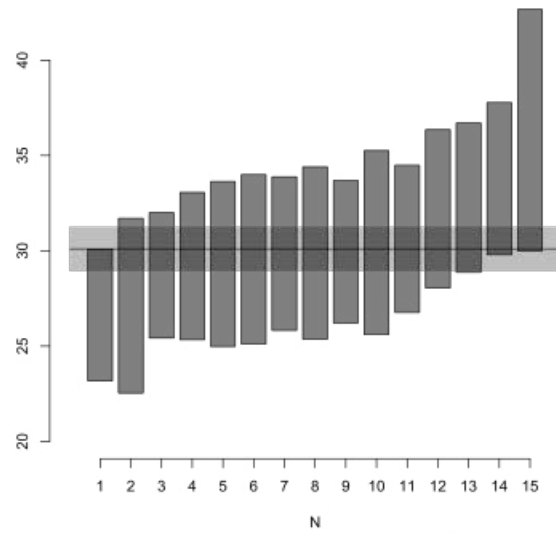


Figure 5. (Continued on following 4 pages.)

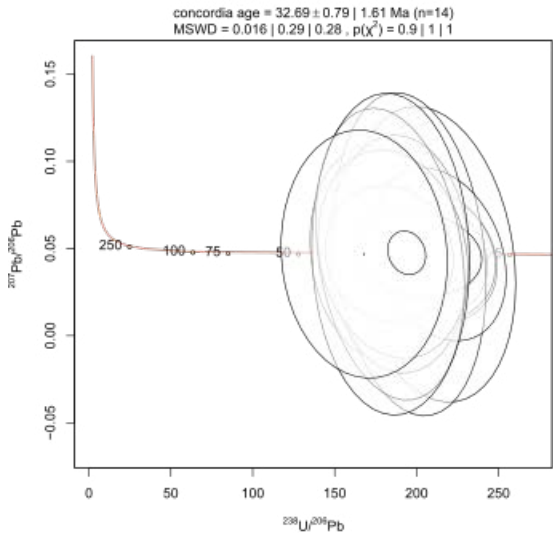
sample SMO15_23 -- 30.10 +/- 0.54 Ma



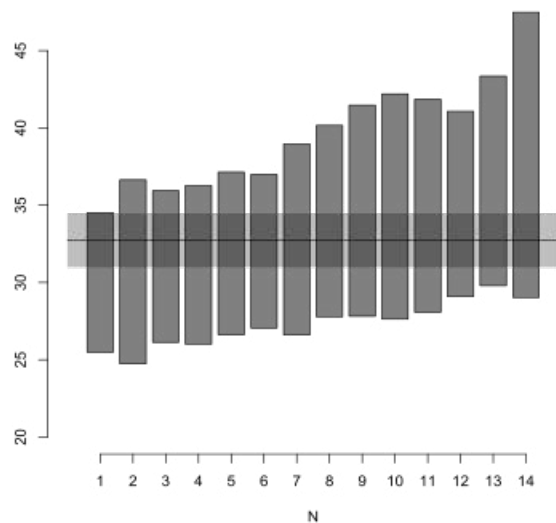
mean = 30.10 ± 0.54 | 1.15 | 1.25 Ma (n=15/15)
MSWD = 1.18, $p(\chi^2) = 0.29$



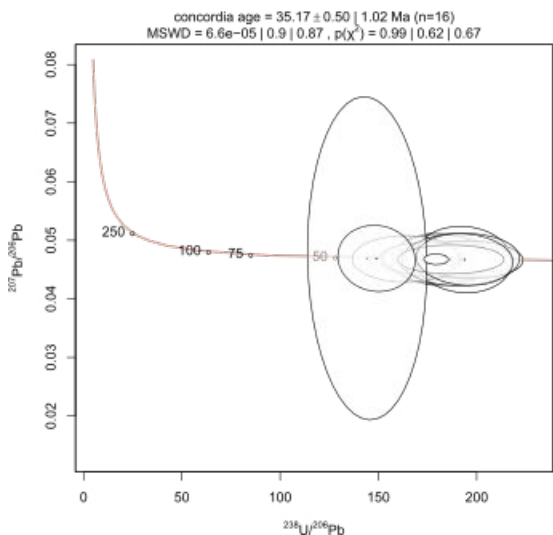
sample SMO15_32 -- 32.72 +/- 0.80 Ma



mean = 32.72 ± 0.80 | 1.72 | 1.29 Ma (n=14/14)
MSWD = 0.56, $p(\chi^2) = 0.89$



sample SMO15_35 -- 34.61 +/- 1.12 Ma



mean = 34.61 ± 0.52 | 1.12 | 0.89 Ma (n=14/16)
MSWD = 0.63, $p(\chi^2) = 0.83$

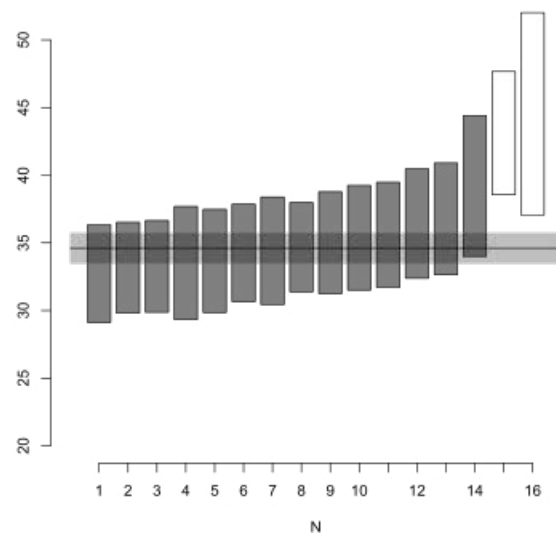
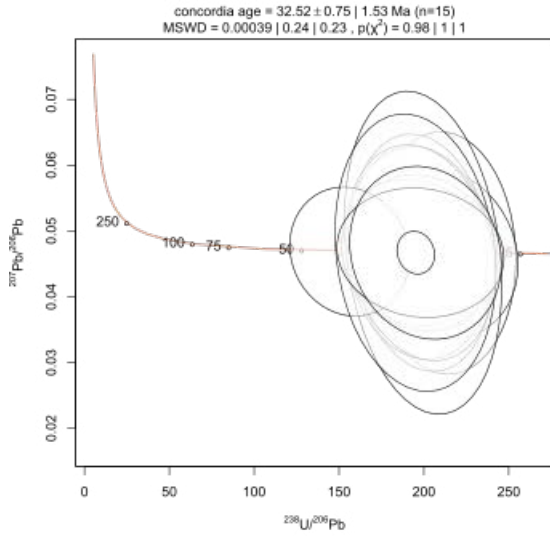
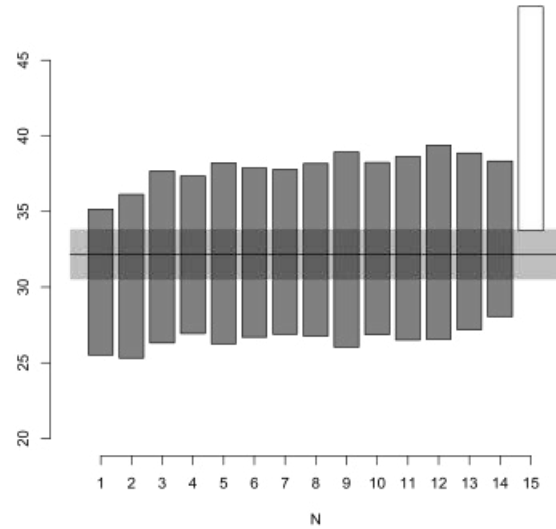


Figure 5. (Continued on following 3 pages.)

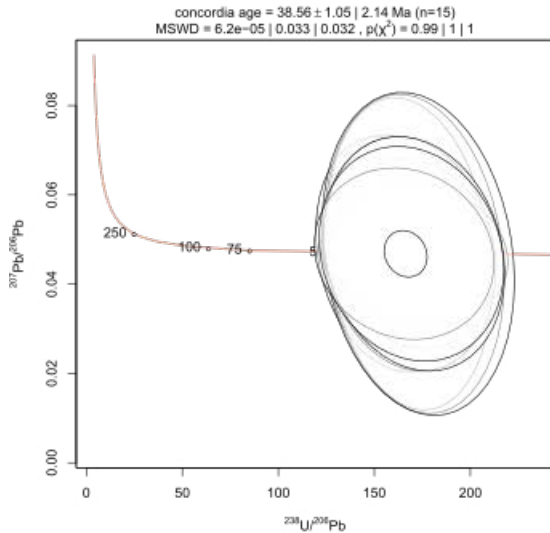
sample SMO15_37 -- 30.10 +/- 0.54 Ma



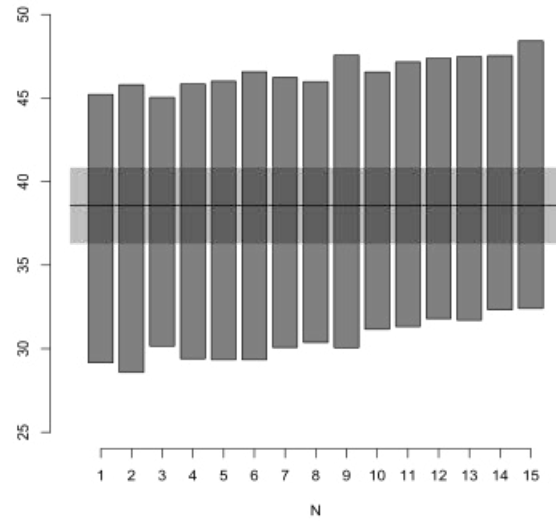
mean = 32.17 ± 0.77 | 1.66 | 0.50 Ma (n=14/15)
MSWD = 0.091, p(χ^2) = 1.00



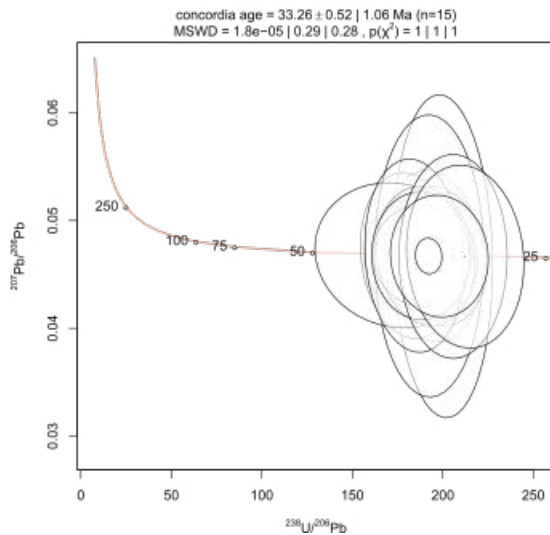
sample SMO15_41 -- 38.57 +/- 1.06 Ma



mean = 38.57 ± 1.06 | 2.27 | 0.58 Ma (n=15/15)
MSWD = 0.065, p(χ^2) = 1.00



sample SMO15_42 -- 33.26 +/- 1.11 Ma



mean = 33.26 ± 0.52 | 1.11 | 0.84 Ma (n=15/15)
MSWD = 0.57, p(χ^2) = 0.89

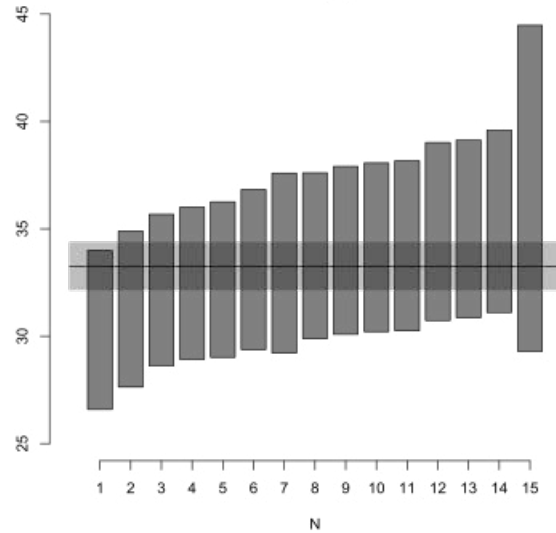
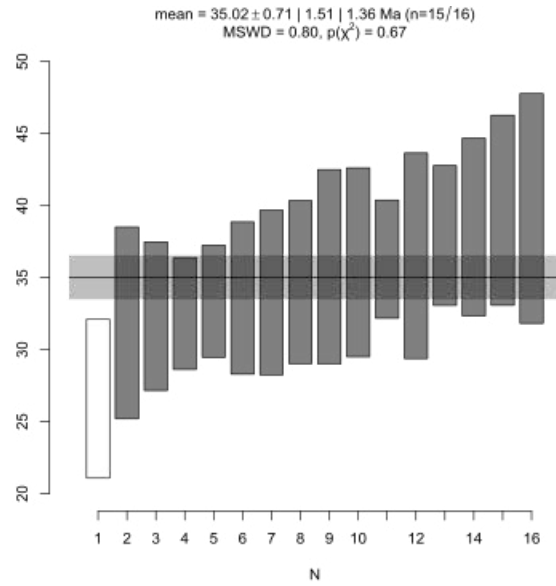
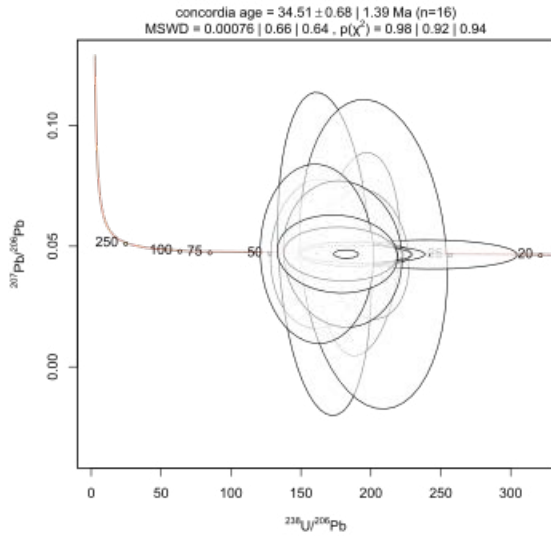
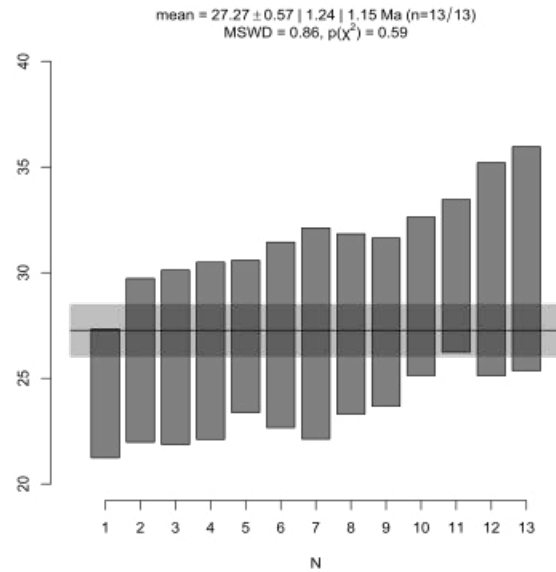
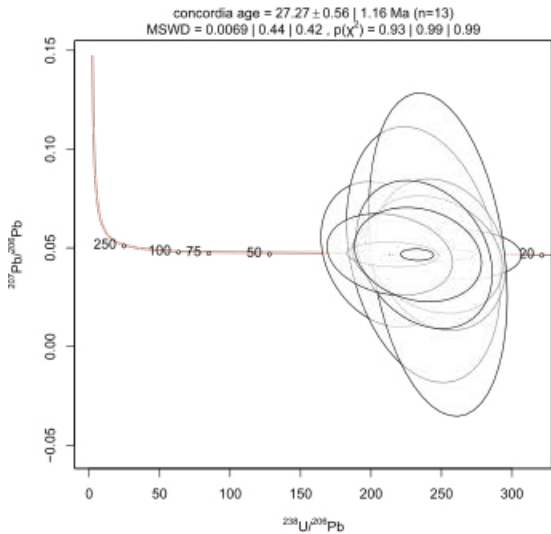


Figure 5. (Continued on following 2 pages.)

sample SMO15_44 -- 35.02 +/- 0.71 Ma



sample SMO15_46 -- 27.27 +/- 1.24 Ma



sample SMO15_49 -- 33.11 +/- 0.56 Ma

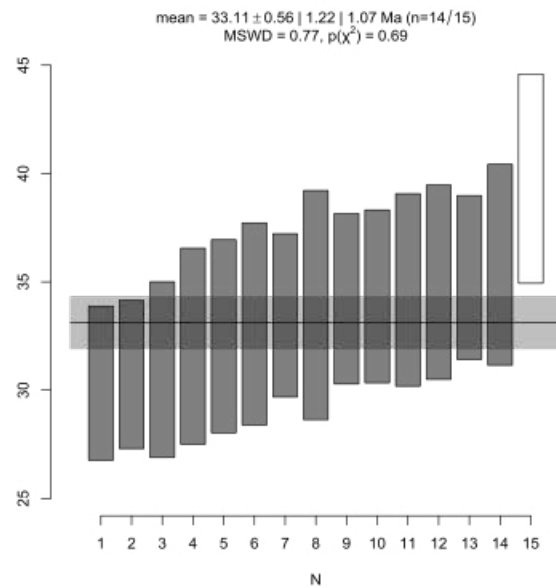
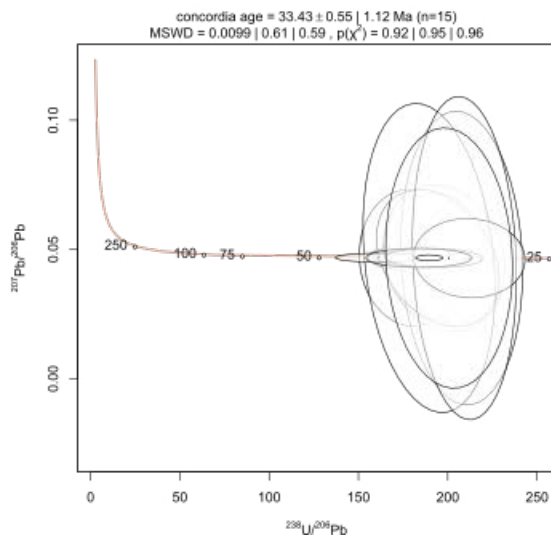
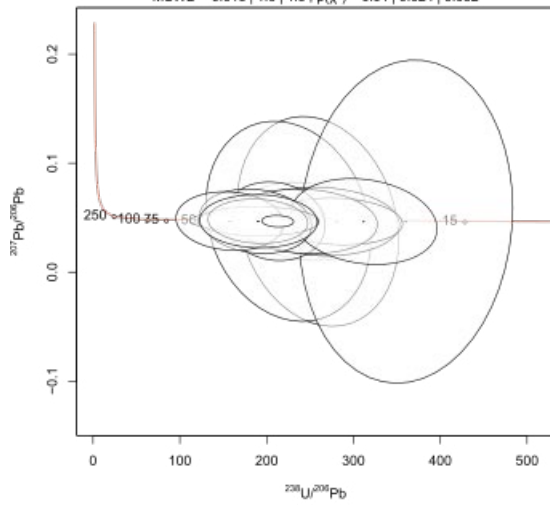


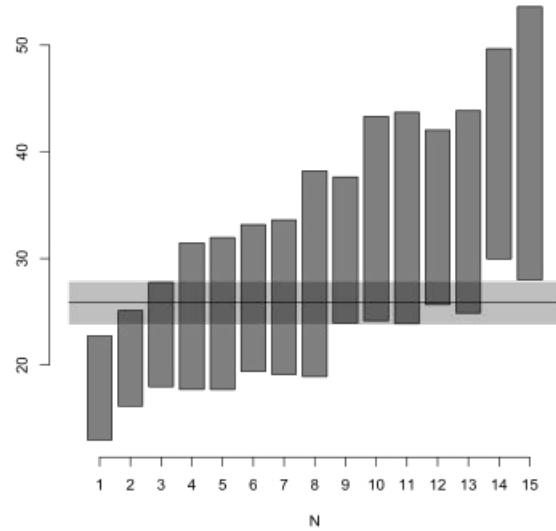
Figure 5. (Continued on following page.)

sample SMO15_52 -- 25.85 +/- 0.92 Ma

concordia age = 25.82 ± 0.91 | 1.86 | 2.87 Ma (n=15)
 MSWD = 0.013 | 1.6 | 1.5, p(χ^2) = 0.91 | 0.024 | 0.032

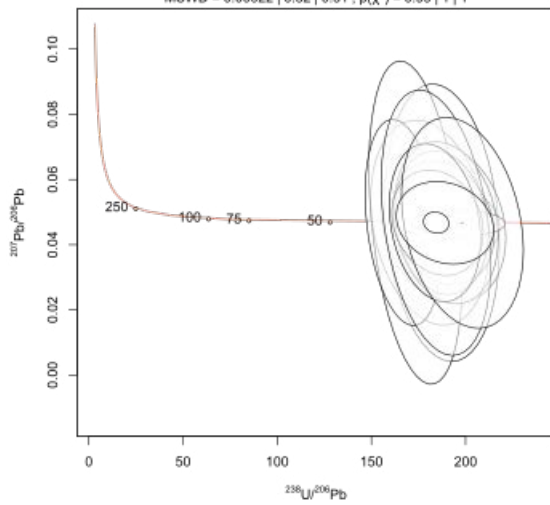


mean = 25.85 ± 0.92 | 1.96 | 3.49 Ma (n=15/15)
 MSWD = 3.16, p(χ^2) = 0.000053



sample SMO15_55 -- 34.62 +/- 0.52 Ma

concordia age = 34.65 ± 0.51 | 1.05 Ma (n=15)
 MSWD = 0.00022 | 0.32 | 0.31, p(χ^2) = 0.99 | 1 | 1



mean = 34.62 ± 0.52 | 1.12 | 0.87 Ma (n=15/15)
 MSWD = 0.60, p(χ^2) = 0.87

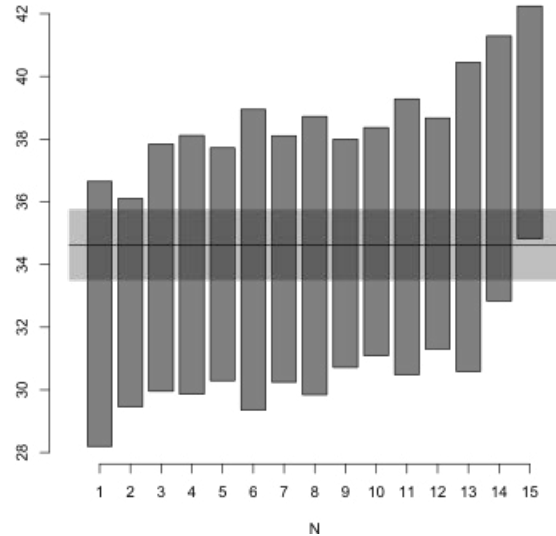


Figure 5 (continued).

weighted deviates (MSWD) for WMAs are high, ranging from 2–9 and 0.1–4 for LA-ICPMS and SIMS, respectively. Mean weighted ages (WMA) of zircon calculated in IsoplotR (Vermeesch, 2018) are presented in Table 1.

$^{206}\text{Pb}/^{238}\text{U}$ zircon crystallization ages are unimodal within each sample and are overwhelmingly concordant (Fig. 5). Age-distinct antecrysts ~3–8 m.y. older than the mean age are common, usually two or three per sample. Xenocrysts are very uncommon, and only 20 grains (~3%) older than 56 Ma were analyzed in ten samples. Eighteen Cretaceous to Paleocene grains were identified in samples 3-20-4 ($n = 3$), CH01 (1), CH03 (3), J406 (2), MAJ (2), N-12 (2), RED (1), SJ-3 (1), SMO15_09 (1), _10 (1), and _14 (1). One Devonian xenocryst (ca. 392 Ma; SMO15_09) and one Triassic xenocryst (ca. 237 Ma; CH03) were measured; no Lower Paleozoic or Precambrian xenocrysts were measured.

Mean crystallization ages are within error of, or are up to 2 m.y. older than, the corresponding published K/Ar or $^{40}\text{Ar}/^{39}\text{Ar}$ cooling ages (Table 1) except for samples SMO15_17 and _44, which are 3 and 4 m.y. older, respectively, and 3-20-4, MAJ, SJ-3, SMO15_46 and _52, which are all significantly (2–4 m.y.) too young. These anomalous ages are nevertheless used to calculate the corresponding ϵHf_T value because of the insensitivity of the long half-life Lu-Hf system to 1–10 m.y. age variations.

Lu-Hf Isotopes

Sierra Madre Occidental rhyolites have published mean whole-rock Hf contents of $\sim 9 \pm 4$ ppm ($n = 157$), ranging from 2–20 ppm (<http://portal.earthchem.org>; Supplemental Material, Section C [footnote 1]). Lu-Hf isotopes are presented as ϵHf_T values based on the corresponding $^{206}\text{Pb}/^{238}\text{U}$ crystallization age of the same analytical spot (e.g., Fig. 3), grouped by sample (Fig. 6; Supplemental Material, Section D). The highest single crystal analysis measured is +7.7 epsilon units from a 393 Ma xenocryst in SMO15_09, and the lowest is –16 epsilon units from a 39 Ma grain in SMO15_55. Most samples show less than 2.5 epsilon units of variation between phenocrysts, and 1σ uncertainties are often <1.0 epsilon units (Table 1). Including ϵHf_T and age outliers, 1σ uncertainties are usually less than 1.5 epsilon units, and the largest is 2.6 epsilon units in SMO15_52. The highest mean ϵHf_T value is +4.6 epsilon units ± 1.0 (N-99; 29.93 Ma), and the lowest is –4.1 epsilon units ± 1.4 (CH88-17; 37.23 Ma), both in the Chihuahua transect (Table 1). The average of all ϵHf_T values is +1.5 epsilon units.

Oxygen Isotopes

Zircon

$\delta^{18}\text{O}_{\text{zircon}}$ values range from 4.4‰ to 10.4‰ (Fig. 7; Supplemental Material, Section E [footnote 1]), and the range within individual samples varies

by <4.5‰ and commonly <2.5‰. There is no systematic variation in $\delta^{18}\text{O}_{\text{zircon}}$ between cores and rims in the same grain (e.g., Fig. 3). The lowest $\delta^{18}\text{O}_{\text{zircon}}$ single-grain values measured are 4.4‰–4.7‰ in SMO15_01, _41 (two grains), _46, and _52; these and an additional seven grains are all less than the $5.3\text{‰} \pm 0.3\text{‰}$ (1σ) mantle zircon of Valley et al. (2005). The highest mean $\delta^{18}\text{O}_{\text{zircon}}$ value (Table 1) is $8.0\text{‰} \pm 2.2\text{‰}$ (SMO15_52), and the lowest is $5.5\text{‰} \pm 0.2\text{‰}$ (CH03). Two anomalously high single-grain $\delta^{18}\text{O}_{\text{zircon}}$ values measured 23.9‰ and 15.8‰, respectively, both from SMO15_44.

Quartz

Eight $\delta^{18}\text{O}_{\text{quartz}}$ measurements are available, six for samples with coexisting zircon (CH03, CH97-7, N-99, SJ-54, K-LP-T, and SL-41; Table 1), and two without (CH06 and 2-71-1). $\delta^{18}\text{O}_{\text{quartz}}$ values range from 8.89‰–10.23‰ and are ~3.0‰–4.0‰ higher than for coexisting zircon. Oxygen isotope data from coexisting quartz-zircon pairs suggest subsolidus oxygen isotope fractionation in quartz between ~530–685 °C (Fig. 8).

Geothermometry

Zircon Saturation Temperatures

Zircon saturation temperatures (T_{Zircsat} ; Watson and Harrison, 1983; Hanchar and Watson, 2003), following the approach of Boehnke et al. (2013), were calculated from whole-rock analyses of 22 samples collected along the central transect and from three published analyses from the northern transect (Supplemental Material, Section F [footnote 1]). Zirconium abundances for these and an additional 67 central transect samples (Moreno, 2016; Pack, 2017) are between ~75 and ~630 ppm and M-values ($([\text{Na} + \text{K} + 2\text{Ca}]/\text{Si} \times \text{Al})$) are between 0.9 and 1.83 (Fig. 9A). Zircon saturation temperatures (T_{Zircsat}) range between 680 and 840 °C (Fig. 9B), with a median value of ~750 °C (Fig. 9C). Utilizing the model of Watson and Harrison (1983) results in temperatures ≥ 100 °C higher than that of Boehnke et al. (2013); taking this into account, our data are comparable (Fig. 9D) with those calculated for six SMO rhyolites by Bryan et al. (2008) and 12 from Siégel et al. (2018).

Liquidus Temperatures (Rhyolite-MELTS)

The estimated liquidus temperatures for SMO rhyolites were calculated using the rhyolite-MELTS and MELTS_Excel packages (Gualda et al., 2012; Gualda and Ghiorso, 2014). Liquidus temperatures were calculated for 25 rhyolites at 125 MPa (~5 km depth) and 0–6 wt% H_2O . A typical SMO rhyolite has a liquidus temperature of 944 °C with 1 wt% H_2O and 861 °C with 3 wt% H_2O (Fig. 9C).

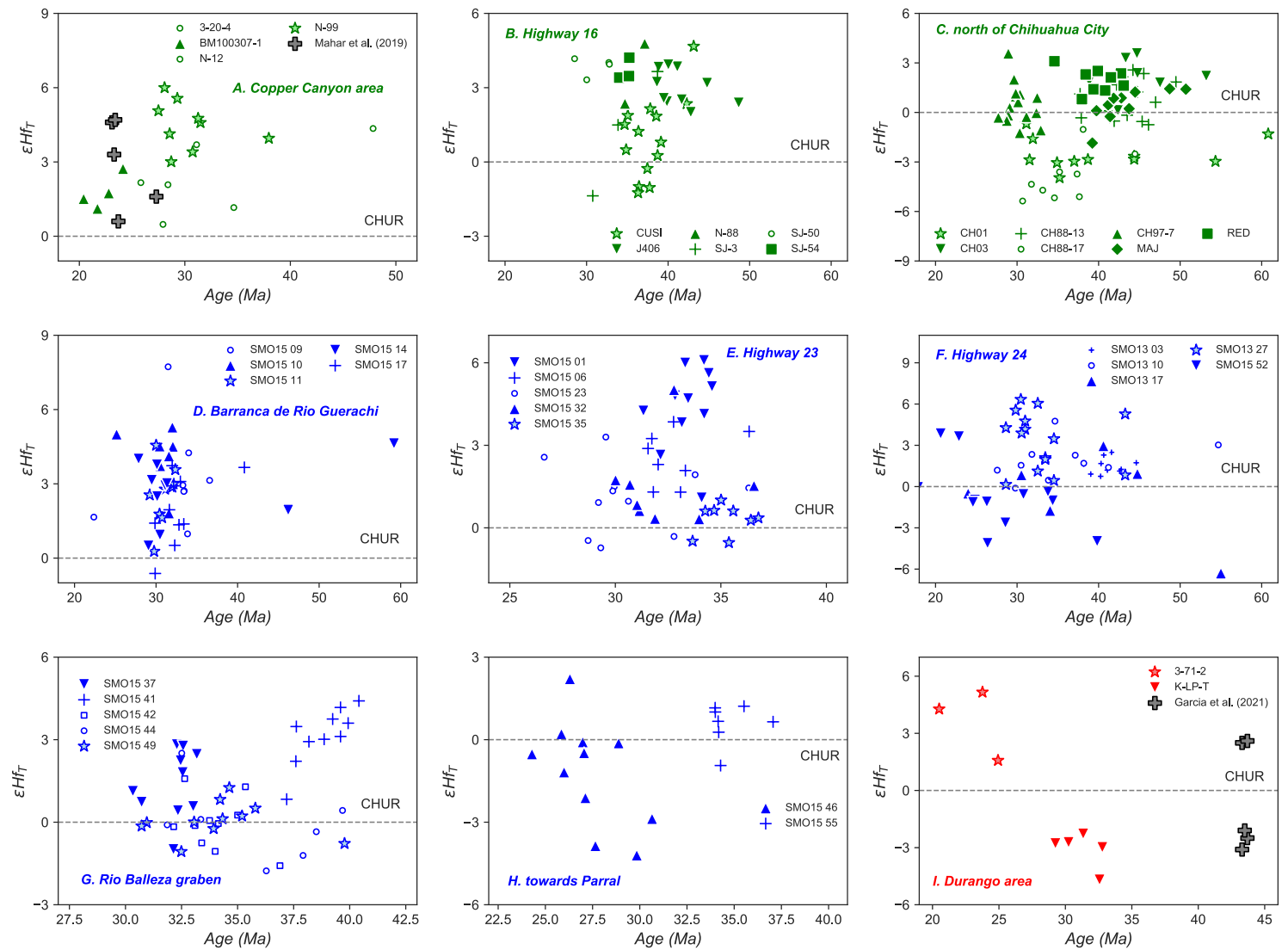


Figure 6. Age versus ϵHf_T plots for samples from the northern (A–C; green), central (D–H; blue), and southern (I; red) transects. Note that the axes differ between charts. Data from Mahar et al. (2019) and Garcia et al. (2021) are shown for reference. ϵHf_T for the depleted mantle in this time range is $\sim +15$ epsilon units. Chondritic uniform reservoir (CHUR) from Bouvier et al. (2008).

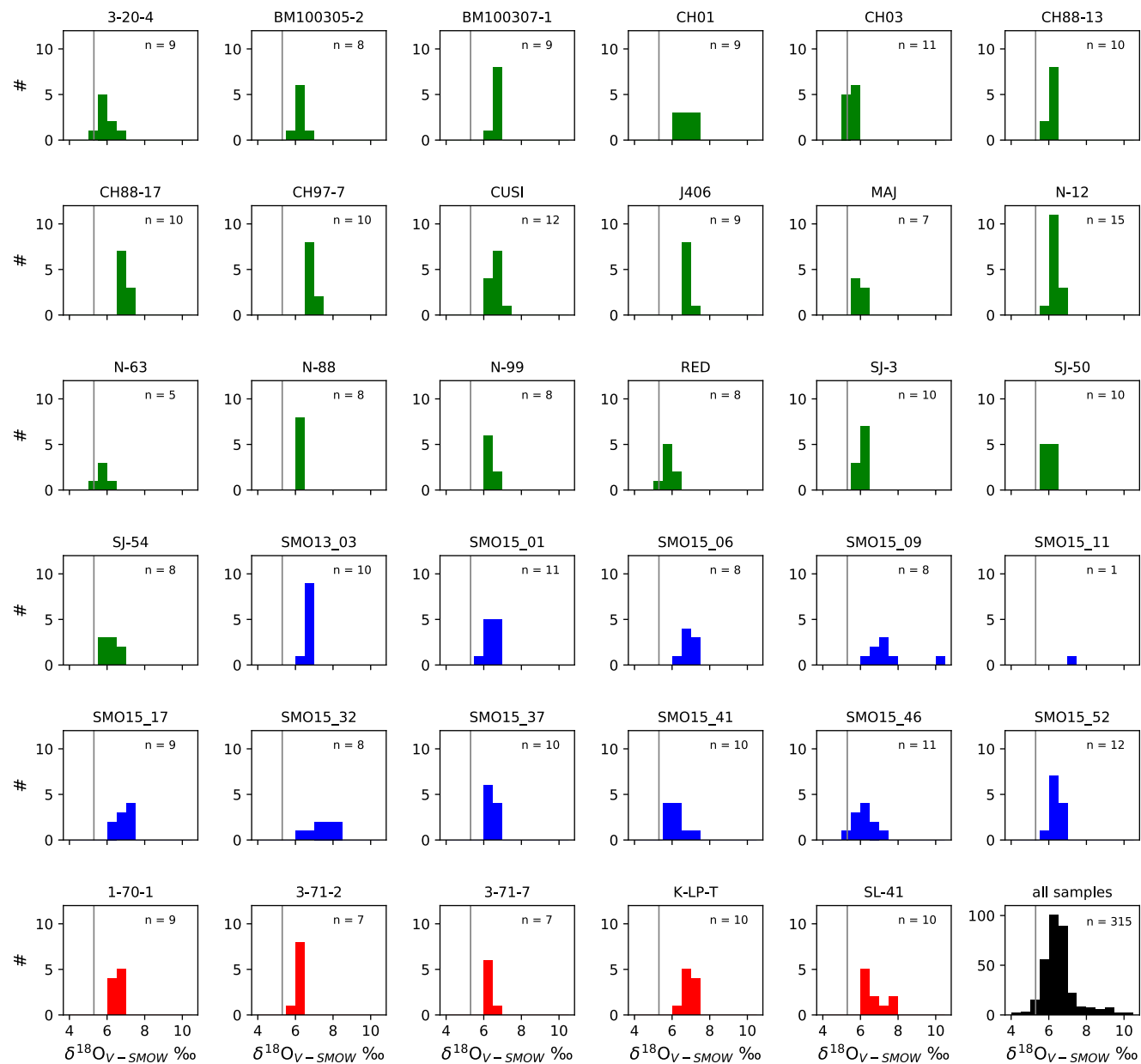


Figure 7. Distributions of $\delta^{18}\text{O}_{\text{zircon}}$ values for each sample from the northern (green), central (blue), and southern (red) transects. The gray line is the $5.3 \pm 0.3\%$ (1σ) mantle zircon value of Valley et al. (2005).

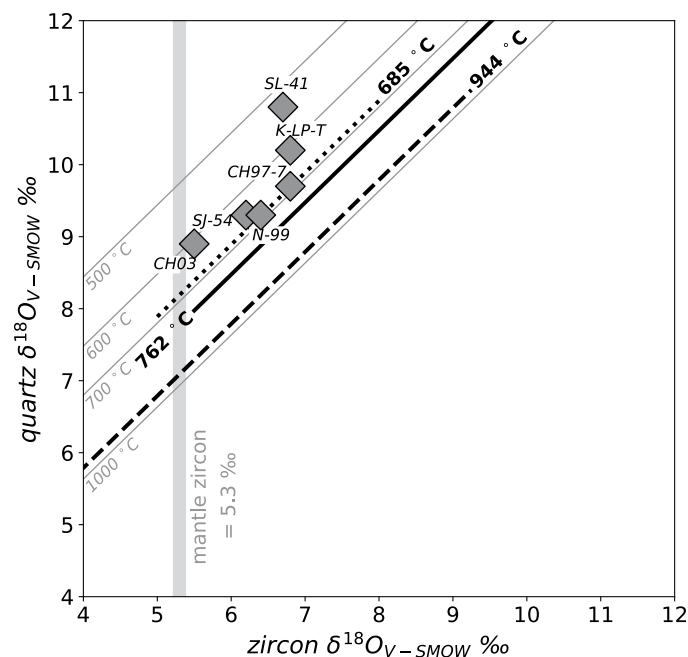


Figure 8. Zircon and quartz $\delta^{18}\text{O}$ values for six Sierra Madre Occidental (SMO) rhyolites and their calculated equilibrium temperatures. The highest equilibrium temperature is 685 °C. Mineral pair fractionation factors for quartz-zircon (Valley, 2003) were used to calculate 500 °C, 600 °C, 700 °C, and 1000 °C isotherms. The mean zircon saturation (762 °C) and estimated liquidus (944 °C) temperatures are shown for comparison.

DISCUSSION

Petrogenesis of Monotonous SMO Flood Rhyolites

Oxygen and Hafnium Isotopic Characteristics

Sierra Madre Occidental tuffs and lavas exhibit limited ranges of ϵHf_T and $\delta^{18}\text{O}_{\text{zircon}}$ within individual samples and throughout the suite (Fig. 10). Based on these data, the SMO rhyolites have $\delta^{18}\text{O}_{\text{zircon}}$ values ranging from crystallization under mantle conditions ($\sim 5.3 \pm 0.3\text{‰}$ (1σ); Valley et al., 2005) to 7‰–8‰, and ϵHf_T values from +6 to –6 epsilon units with a mean of $\sim +2$ epsilon units. SMO rhyolites are isotopically homogeneous and form a distinct cluster in ϵHf_T – $\delta^{18}\text{O}$ space. There is no systematic temporal (Fig. 10) or spatial variation in mean $\delta^{18}\text{O}_{\text{zircon}}$ and ϵHf_T values, or T_{zircsat} (Fig. 9D). This implies a uniform petrogenesis throughout the duration (~ 20 m.y.) and extent (4×10^5 km²) of SMO silicic volcanism. Combining their homogeneous zircon isotopic character

with published whole-rock elemental and isotopic data leads us to conclude that the SMO silicic magmas were remarkably monotonous.

Petrogenetic Model

The SMO likely buries a thick (25–30 km), Phanerozoic succession dominated by marine sedimentary and volcanoclastic lithologies (Fig. 11; Bryan et al., 2008). Magmatic assimilation of significant volumes of Phanerozoic sediment derived from Precambrian basement should have generated strongly negative ϵHf_T values. Assimilation of upper-crustal rocks, including pelites and carbonates (e.g., Bindeman, 2008), can raise the $\delta^{18}\text{O}_{\text{zircon}}$ value significantly. In contrast, assimilation of high-temperature hydrothermal systems (e.g., intracaldera successions; Bindeman et al., 2007) and epithermal alteration zones (e.g., Boroughs et al., 2005) can significantly lower the $\delta^{18}\text{O}_{\text{zircon}}$ value. Therefore, the absence of low- ($<4\text{‰}$; Valley et al., 2003) and high- $\delta^{18}\text{O}_{\text{zircon}}$ ($\geq 8\text{‰}$), and strongly negative ϵHf_T zircons is inferred to indicate that SMO magmas did not assimilate large volumes of upper- and middle-crustal rocks, including carbonaceous marine sedimentary rocks exposed around Parral (Fig. 1).

The narrow ranges of $\delta^{18}\text{O}_{\text{zircon}}$ and ϵHf_T values (Figs. 6, 7, and 10) are typical of magmas that have evolved, at least in part, by fractional crystallization of mafic melts (cf. Balsley and Gregory, 1998) in “hot” arc regimes with significant input from the mantle (e.g., Attia et al., 2020). Assimilation of some crustal material is required to explain the few xenocrysts identified and the rhyolites with weakly negative ϵHf_T values (Fig. 10). The paucity of xenocrystic zircon corroborates the results of Bryan et al. (2008) and suggests that magmatic temperatures (~ 700 – 850 °C) and xenocryst residence times were great enough to dissolve most older zircon. It is unlikely that the elevated magmatic temperatures needed to allow fractional crystallization processes and xenocryst destruction could be sustained for very long (10^6 years) in the upper crust (e.g., Annen et al., 2006; de Silva and Gosnold, 2007) without cooling and crystallization (e.g., Miller et al., 2003).

Instead, eruptible SMO magmas evolved from melts in excess of their zircon saturation temperatures (>850 – 900 °C). The moderately crystal-poor and xenocryst-free rhyolites of the SMO were likely “hot” magmas (e.g., Miller et al., 2003; Halder et al., 2021) that required significant advective thermal input into the lower crust to sustain the necessary high magmatic temperatures. This anomalously high thermal flux was sustained throughout the duration and extent of SMO volcanism to account for the monotony of the rhyolites. Bryan et al. (2008) attributed the sustained high thermal flux to the repetitive emplacement of mafic bodies into the lower crust, thereby transferring both mantle melt and advected heat. The lower crust evolved into a region of melting-assimilation-storage-homogenization (Fig. 11; “MASH zone”; Hildreth and Moor bath, 1988), where melts of the country rock protolith and older mafic intrusions are mixed and assimilated into juvenile magmas undergoing fractional crystallization (e.g., Lee et al., 2007). Thus, AFC processes are inextricably linked. Thermal models demonstrate the efficiency of repetitive mafic

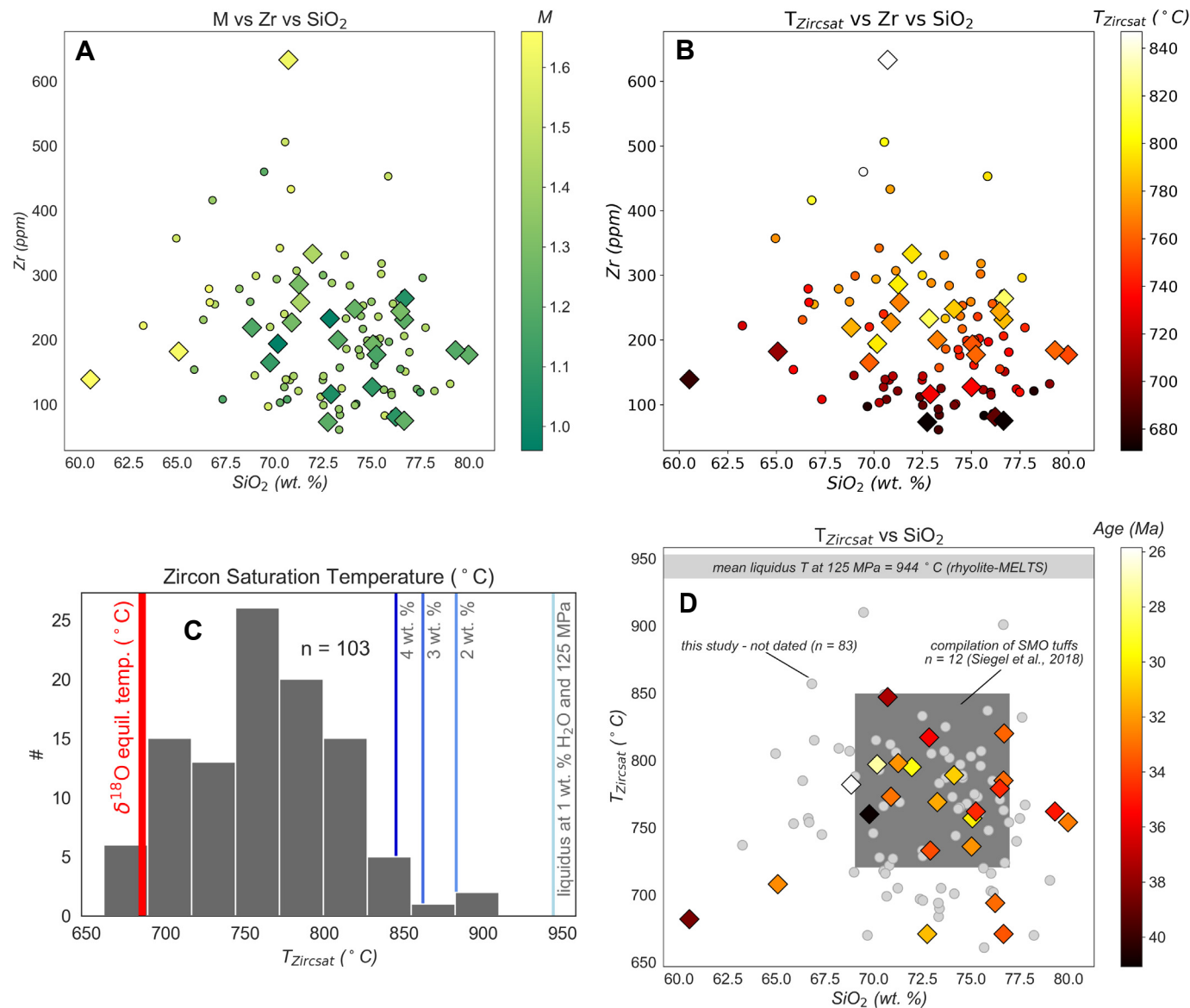


Figure 9. Zircon saturation temperatures for 103 Sierra Madre Occidental (SMO) samples (Moreno, 2016; Pack, 2017; this study) including the 49 reported herein. SiO₂ content versus Zr colored for (A) “M value” (Watson and Harrison, 1983; Boehnke et al., 2013) and (B) zircon saturation temperature (°C). (C) Distribution of zircon saturation temperatures. The calculated δ¹⁸O equilibrium temperature (Valley, 2003) and the calculated liquidus temperatures (Gualda and Ghiorso, 2014) for four different water contents at 125 MPa are shown for reference. (D) Zircon saturation temperatures for dated SMO samples (colored by age), non-dated SMO samples (gray; Pack, 2017), and the compilation of SMO tuffs (n = 12) from Siégel et al. (2018).

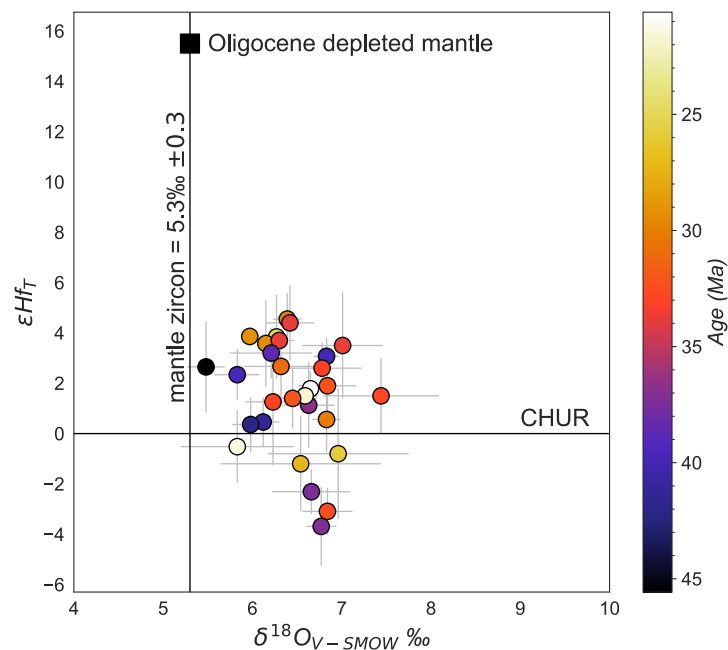


Figure 10. Plot of mean $\delta^{18}\text{O}_{\text{zircon}}$ and ϵHf_T for double-analyzed Sierra Madre Occidental (SMO) tuffs and lavas. Error bars are 1σ . Individual samples are color-coded for age. CHUR—chondritic uniform reservoir.

intrusions to elevate the temperature of the surrounding lower crust (Huppert and Sparks, 1988; Annen and Sparks, 2002; Dufek and Bergantz, 2005; Annen et al., 2006). The same models indicate that temperature can reach $>300^\circ\text{C}$ above the solidus ($950\text{--}1000^\circ\text{C}$) in 1–1.5 m.y. (Annen et al., 2006) provided that the intrusion rate is 50 m (sill thickness) per $\geq 0.01\text{--}0.1$ m.y. Super-liquidus silicic magmas formed in the lower or middle crust will have some concentration of dissolved water in them and will likely have viscosities in the $10^4\text{--}10^5$ Pa.s range (e.g., Scarfe et al., 1987; Giordano et al., 2008), many orders of magnitude less than at the surface. Such low viscosities allow for efficient transport through the remaining crust from where the magmas are either erupted directly or assembled over short timescales (e.g., Annen, 2009) in shallow sills associated with calderas.

Insights from Xenoliths

Xenolith localities and a very few outcrops around the northern SMO allow sampling of basement lithologies likely representative of the lower crust where SMO magmas are inferred to have been generated. Lower-crustal

xenoliths from La Olivina (Fig. 1; Ruiz et al., 1988b; Rudnick and Cameron, 1991; Cameron et al., 1992; Nimz et al., 1995) include mafic granulites, intermediate to felsic orthogneisses, and paragneisses. Xenolith U/Pb zircon age populations are diverse and complex (Rudnick and Cameron, 1991), and all gneissic samples show evidence for granulite-facies metamorphism in the Neogene, Late Triassic, and at ca. 1.1 Ga (Grenville orogeny). La Olivina is placed south of the Laurentian craton margin in the Late Paleozoic Ouachita suture zone (Fig. 1) by Ortega-Gutiérrez et al. (2018). The presence of xenoliths with ≥ 1.0 Ga metamorphic ages requires that either (1) the basement beneath La Olivina is the very northernmost tip of Oaxaquia (ca. 1.2–0.9 Ga; Ortega-Gutiérrez et al., 2018), or (2) the Laurentian margin has to be extended at least 20 km farther southeast (Ruiz et al., 1988a; Rudnick and Cameron, 1991; Cameron et al., 1992).

The only mafic granulite xenolith dated has a mean age of 1.3 ± 0.3 Ma, within error of the K/Ar age of the surrounding alkali basalt lavas (Rudnick and Cameron, 1991). The mafic granulites are isotopically primitive compared to the gneisses ($^{87}\text{Sr}/^{86}\text{Sr}_{30} \sim 0.705$; $\epsilon\text{Nd}_{30} \sim 0$) and indistinguishable from the SMO and Neogene mafic volcanic rocks (Cameron et al., 1992). They are typical of mafic lower-crustal rocks throughout northern Mexico (Ruiz et al., 1988b). A single granulite-facies, sillimanite-paragneiss has a maximum depositional age of 1.0 Ga and was metamorphosed at 40–20 Ma, broadly contemporaneous with SMO magmatism. The paragneisses have very strongly negative ϵNd_{30} (-8 to -16 epsilon) and high $^{87}\text{Sr}/^{86}\text{Sr}_{30}$ (>0.720). Differently aged but compositionally similar intermediate orthogneisses are present below La Olivina, where xenoliths with inferred magmatic ages of ca. 1.4 Ga, ca. 300 Ma, and 37–25 Ma have been recovered (Rudnick and Cameron, 1991). Rudnick and Cameron (1991) interpreted 37–25 Ma sample MN-40 (64.5 wt% SiO_2) to be deep-seated relation of SMO rhyolites, and they have identical strontium, neodymium, and lead isotopes values (Cameron et al., 1992). The older orthogneisses are less primitive with strongly negative ϵNd_{30} values and form a seamless trend with the paragneisses.

Xenoliths from Potrillo in northern Chihuahua and basement outcrops at Los Filtros north of Chihuahua City (Fig. 1) provide additional constraints on plausible lower crust beneath the northern SMO. Non-dated paragneiss xenoliths from Potrillo are less isotopically evolved ($\epsilon\text{Nd}_{30} \sim -7$ epsilon; $^{87}\text{Sr}/^{86}\text{Sr}_{30} \sim 0.706$) than those at La Olivina (Ruiz et al., 1988b). High-grade orthogneisses and granitoids spanning 1.3–1.0 Ga at Los Filtros have initial $^{87}\text{Sr}/^{86}\text{Sr}$ values of ~ 0.708 and are inferred to be part of a belt of Grenville-age Laurentian basement extending to and beyond the Llano Uplift in central Texas (Ruiz et al., 1988b; Ortega-Gutiérrez et al., 2018).

Cameron et al. (1992) interpreted Cenozoic xenoliths at La Olivina as evidence for wholesale or significant modification of the lower crust by mafic underplating and associated granulite-facies metamorphism (Fig. 11). However, because there are no basement outcrops or xenoliths from within or adjacent to the central SMO between La Olivina and the Mesa Central (Fig. 1), this interpretation cannot be rigorously tested. The same area is underlain by the Mesozoic accreted Alisitos-Guerrero composite terrane (Fig. 1; Centeno-García

et al., 1993); the composition and age of the lower crust of the Guerrero terrane and its subcontinental lithospheric mantle are unknown (Fig. 11). The lack of sub-SMO information contributes to a “chicken and egg” paradox where geochemical data yield insights into the buried basement age and composition, but the same data are modeled to understand potential sources of the SMO magmas and their relative contributions (e.g., Cameron and Cameron, 1985; Ruiz, et al., 1988b; Cameron et al., 1989; Wark, 1991).

Mixing Models

The observed difference in ϵHf_r ($\sim+14$ epsilon) and $\delta^{18}\text{O}$ ($\sim+1.2\%$) values in SMO zircons from mantle values, where 35 Ma depleted mantle is $+15.5$ epsilon units and 5.3% , is best explained by AFC processes (e.g., DePaolo, 1981).

Lower-crustal xenoliths from La Olivina and Potrillo provide potential end-members with which to model assimilation of different crustal contributions with both enriched and primitive mantle-derived melts. We applied Equation 15a of DePaolo (1981) to model AFC paths in ϵHf_r - $\delta^{18}\text{O}$ space (Fig. 12) with the same fixed rate of fractional crystallization twice that of assimilation ($r = 0.5$) used by Cameron and Cameron (1985) and Cameron et al. (1989). We modeled a range of scenarios using three possible crustal end-members and four different mantle end-members (Supplemental Material, Section G [footnote 1]). The crustal end-members are a mafic orthogneiss and a paragneiss from La Olivina (Cameron et al., 1992) and a paragneiss from Potrillo, northern Chihuahua (Ruiz et al., 1988b). Epsilon hafnium values for 35 Ma zircon (ϵHf_{35}) were calculated from published whole-rock ϵNd_{30} values using the terrestrial array equation of Vervoort et al. (2011). Whole-rock $\delta^{18}\text{O}$ values were calculated from $\delta^{18}\text{O}_{\text{zircon}}$ using an equilibrium temperature of $800\text{ }^\circ\text{C}$ (Bindeman et al., 2007).

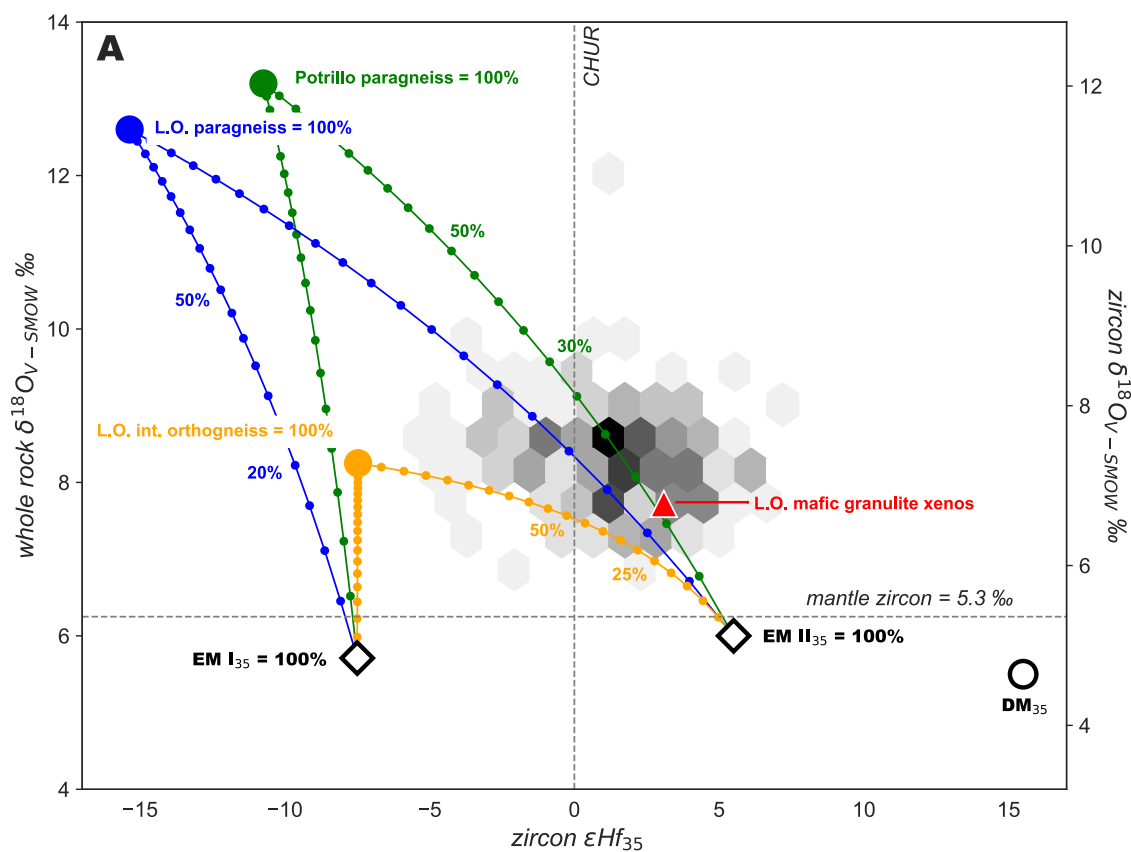


Figure 12. Density plot of Sierra Madre Occidental (SMO) samples in $\delta^{18}\text{O}_{\text{whole-rock}} - \epsilon\text{Hf}_{35}$ space showing calculated assimilation-fractional crystallization (AFC) mixing lines between different mantle and lower crustal end-members; see text for details. (A) Mixing lines between enriched mantle end-members (EM I₃₅ and EM II₃₅) and three lower-crustal lithologies recorded in xenoliths: La Olivina (LO) intermediate orthogneiss, La Olivina sillimanite-paragneiss, and Potrillo kyanite-paragneiss. (Continued on following page.)

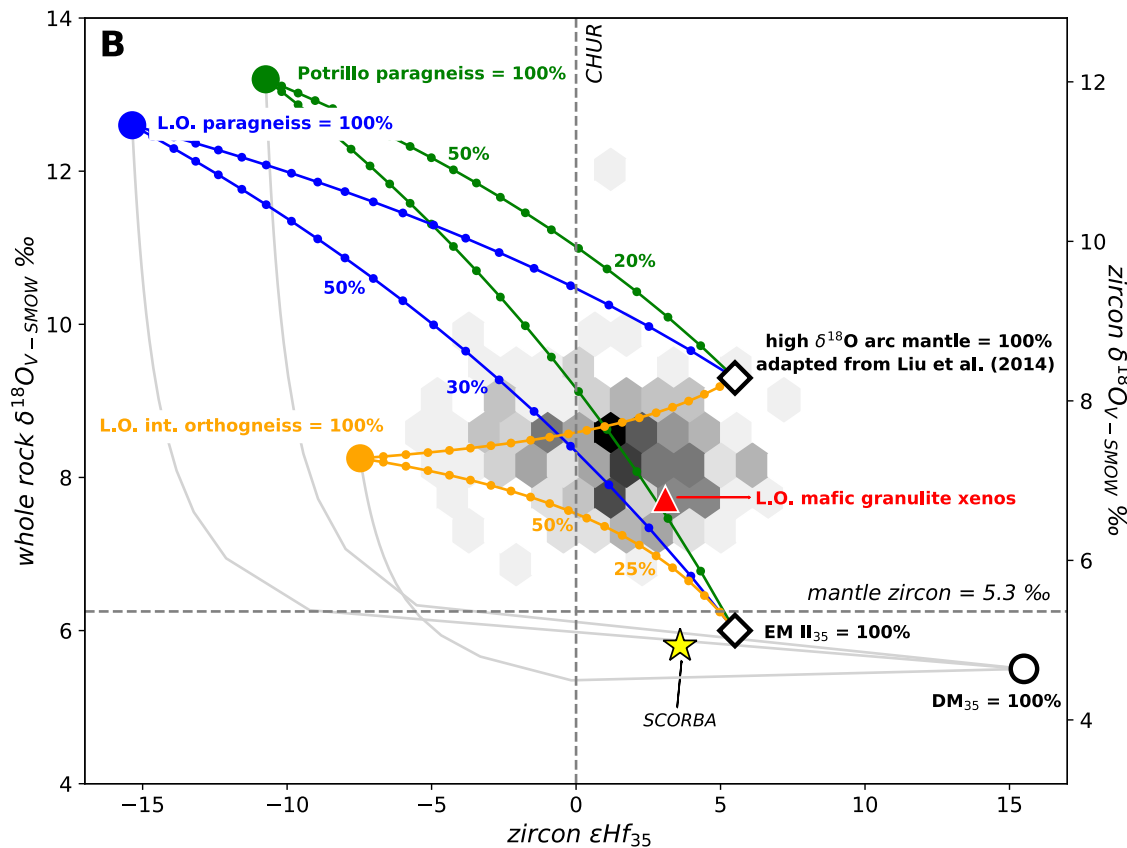


Figure 12 (continued). (B) Mixing lines between the same crustal end-members and two additional mantle end-members: depleted mantle (DM₃₅) and a putative high δ¹⁸O arc mantle (Liu et al., 2014) adapted from EMII₃₅. Each binary mixing line is divided into 5% increments. Southern Cordilleran basaltic andesite (SCORBA) lavas and mafic granulite xenoliths coeval with the SMO silicic magmas are shown for reference. CHUR—chondritic uniform reservoir; V-SMOW—Vienna standard mean ocean water.

Figure 12A depicts AFC mixing lines between enriched mantle sources and the three crustal end-members. Twenty percent assimilation of either paragneiss end-member with moderately enriched mantle (EMII₃₅) reproduces the δ¹⁸O_{WR} and εHf₃₅ values most characteristic of the SMO rhyolites. Furthermore, assimilation of ~10% paragneiss reproduces the isotopic characteristics of the coeval mafic granulite xenoliths inferred by Cameron et al. (1992) to be cumulates formed during fractional crystallization of the SMO silicic magmas. Negative epsilon hafnium and δ¹⁸O_{WR} ≈ 8 ‰ SMO rhyolites (Fig. 12A) are best modeled by significant (i.e., ≥50%) assimilation of intermediate composition orthogneiss. Although there are relatively few of these rhyolites (~4; Table 1), they all occur at the eastern ends of transects, on inferred, Proterozoic continental basement (i.e., not on the accreted Guerrero terrane). Furthermore, samples CH01 and CH88-17 of the northern transect are both less than 50 km west of exposed Proterozoic basement (1.3–1.1 Ga) at Los Filtros, Chihuahua (Fig. 1; Ruiz et al., 1988a, 1988b).

High epsilon hafnium (>+4) samples are modeled poorly by EMII₃₅ (Fig. 12A); so Figure 12B presents some alternative mantle end-members: depleted mantle (DM₃₅) and a putative δ¹⁸O-enriched (~9 ‰) form of EMII₃₅ based on Liu et al. (2014) representing hydrated arc mantle. The high epsilon hafnium samples are modeled successfully when using a mix of 10%–20% paragneiss or orthogneiss and a combination of EMII₃₅ and the δ¹⁸O-enriched arc mantle, or alternatively, a form of EMII₃₅ not as highly δ¹⁸O enriched as that described by Liu et al. (2014) from Tibet. Another explanation is satisfied if the EMII₃₅ mantle beneath the SMO was enriched in hafnium from subducted sediments; however, such sediments cannot have been derived from Precambrian crust without lowering the εHf₃₅ values, and must, therefore, have been relatively young (i.e., Phanerozoic protoliths). Finally, depleted mantle is not a viable end-member for SMO silicic magmas (Fig. 12B) due largely to its very low hafnium concentration; however, it is potentially a source of melt for the coeval

southern Cordilleran basaltic andesite (SCORBA) mafic lavas with ~2%–3% paragneiss assimilated.

Estimated Magmatic Flux

Our data suggest a juvenile-recycled crust ratio of ~4:1 for the SMO. Assuming an erupted volume of $\sim 3.9 \times 10^5 \text{ km}^3$ (Bryan et al., 2008) implies $\sim 3.1 \times 10^5 \text{ km}^3$ of silicic magma fractionated from a mafic melt in the lower crust. Assuming this was 100% of the available residual silicic melt fraction after 90% crystallization (e.g., Dunbar et al., 1993; Bower and Woods, 1998) implies fractionation from a mafic source with a volume of $\sim 2.8 \times 10^6 \text{ km}^3$. These values are underestimates by ~3–10 times (e.g., White et al., 2006) if inferred upper-crustal SMO reservoirs (Fig. 10) are included.

Estimating the magmatic and eruptive fluxes over the ~20 m.y. duration of apparently uninterrupted SMO volcanism (McDowell, 2007; McDowell and McIntosh, 2012) yields values of $\sim 0.14 \text{ km}^3 \text{ yr}^{-1}$ and $\sim 0.02 \text{ km}^3 \text{ yr}^{-1}$, respectively. White et al. (2006) calculated a volcanic flux of $0.03 \text{ km}^3 \text{ yr}^{-1}$ for the SMO over a 15 m.y. time interval. Time-averaging underestimates the peak volcanic fluxes of discrete pulses. Seventy percent of SMO eruptive ages reported in McDowell and McIntosh (2012) are in a 7 m.y. range between 36–29 Ma. If 70% of the volume of the SMO erupted at this time, the peak magmatic and volcanic fluxes are $0.28 \text{ km}^3 \text{ yr}^{-1}$ and $0.03 \text{ km}^3 \text{ yr}^{-1}$, respectively.

Mean global *magma* production since the Jurassic is $\sim 26\text{--}34 \text{ km}^3 \text{ yr}^{-1}$ (Crisp, 1984); magmatism associated with the SMO was ~1%–1.5% of this long-term average. Mean global *volcanic* output is $\sim 0.01\text{--}0.1 \text{ km}^3 \text{ yr}^{-1}$ (Crisp, 1984; White et al., 2006). Silicic and intermediate volcanism both average $0.004 \text{ km}^3 \text{ yr}^{-1}$, basaltic volcanism (excluding flood basalts) averages $0.026 \text{ km}^3 \text{ yr}^{-1}$, and flood basalts average $1 \text{ km}^3 \text{ yr}^{-1}$ (White et al., 2006). Therefore, the volcanic part of the SMO had a similar output to the long-term global mafic output and was ten times that of intermediate or silicic output. When Quaternary silicic and intermediate volcanic outputs are combined, similar $\sim 10^{-2} \text{ km}^3 \text{ yr}^{-1}$ rates are estimated at the Ethiopian and Kenyan portions of the East African Rift, the Kamchatkan, Kyushu, and Taupo intra-arc rifts (White et al., 2006).

Reconciliation with Previous Models of SMO Petrogenesis and Tectonics

Petrogenesis. We estimate the juvenile component of SMO magmas to be ~80% (Fig. 12). This is in excellent agreement with several AFC models based on trace-element and Sr and Nd isotopic analyses (e.g., Lanphere et al., 1980; Cameron and Cameron, 1985; Cameron et al., 1986; Wark, 1991; Smith et al., 1996). Fractional crystallization of a primitive melt to produce a silicic magma, enhanced further by partial melting of the surrounding lower crust, also provides a mechanism to advect-in the necessary thermal input to sustain and drive the AFC process (e.g., Annen and Sparks, 2002). This would be enhanced further by latent heat of crystallization from the fractionating mafic cumulate.

Our data are incompatible with the SMO magmas forming by assimilation of >50% continental crust (e.g., Ruiz et al., 1988b; Bryan et al., 2008) except along the eastern margins of the SMO where there is thick Proterozoic crust and an absence of accreted Mesozoic terranes (Fig. 12A). This implies that voluminous mafic melt *and* heat were transferred from the mantle into the base of the crust (cf. Ducea and Barton, 2007) causing melting, assimilation, and fractional crystallization under the thinner, younger crust below the western and central SMO. Thermal models indicate that conduction of thermal energy from the mantle is insufficient to drive and sustain melting and assimilation of continental crust. However, it is difficult for hafnium and oxygen compositions to discern fractionation of juvenile mafic magma and re-melting and subsequent fractionation of a slightly older mafic body (e.g., Bryan et al., 2008), and while neither are mutually exclusive, we cannot rule the latter out entirely. In contrast, in the thicker, older crust below the eastern SMO, heat transfer was dominant and drove anatectic melting of fertile Proterozoic orthogneisses and paragneisses with less mixing-in of mafic melts.

Crustal Thickness. Any AFC model needs to accommodate the addition of enormous volumes of mafic melt in the lower crust, most likely as a mafic underplate. Ruiz et al. (1990)'s most compelling argument against contemporary AFC models was the strong negative gravity anomaly co-spatial with the SMO. They inferred the presence of a low density, granitoid batholith in the upper and middle crust beneath the SMO. They discounted the alternative of a 4-km-thick mafic underplate (Cameron et al., 1980) in the lower crust as this would be expected to produce a positive gravity anomaly. However, there is no supporting evidence for an upper-crustal batholith; for example, there are no Cenozoic granitoid xenoliths reported. Furthermore, our hafnium and oxygen isotope data are inconsistent with assimilation of large volumes of middle- and upper-crustal rocks (e.g., $\delta^{18}\text{O} > 10\text{‰}$).

This inconsistency can be reconciled if some or all of the mafic underplate has been removed and recycled into the mantle (e.g., Lee et al., 2011). Assuming that the underplate had the same area as the modern extent of the SMO, the underplate would be >7 km thick; in contrast, reconstruction of the ~40-km-thick Sierra Nevada batholith crustal section requires a now missing ~80 km of mafic and ultramafic arc root (Saleeby et al., 2003). The thickness of the crust beneath the SMO is not well constrained; estimates range from ~55 km in the north (Bonner and Herrin, 1999) and ~40 km in the central SMO (Gomberg et al., 1989), to a uniform 30–35 km (Laske et al., 2013; Zhu et al., 2016). The minimum thickness of the necessary mafic underplate, therefore, is ~7%–23% of the current crust.

The absence of pyroxenite, ultramafic cumulate, or mantle xenoliths at La Olivina is consistent with removal of a mafic underplate and/or arc root before ca. 1.5 Ma. Application of a simple Airy isostasy model to the ~2000 m asl SMO plateau is compensated by a missing 10-km-thick mafic underplate (2.86 g/m^3) or a 5-km-thick underplate of equal parts mafic and pyroxenite (3.13 g/m^3). Removal of either of these masses would produce a negative gravity anomaly and anomalously high topography. Thicker SMO crust compensates for high topography but not for the negative gravity anomaly.

Tectonic Scenarios

Extension and thinning of the upper crust was broadly contemporaneous and co-spatial with Cordilleran volcanism during retreat and rollback of the Farallon slab (e.g., Damon et al., 1981; Ferrari et al., 2007). Although diffuse across the Basin and Range province, extension became localized to either margin of the SMO in Mexico, where the Paleocene–Eocene arc had not advanced so far to the east, and therefore, had less far to retreat. There was probably insufficient slab rollback to expose a large enough region of already hydrated subcontinental lithospheric mantle to allow enough up-welling of isotopically primitive asthenosphere (i.e., depleted mantle). The strongest argument in support of this is that rollback was much greater under the Basin and Range, and yet the volumes and rates of volcanism are an order of magnitude smaller than in the SMO (e.g., White et al., 2006), regardless of whether or not AFC processes were dominant.

Bryan and Ferrari (2013) and Ferrari et al. (2018) recognized the bimodal nature of calc-alkaline volcanism (basaltic andesite [SCORBA] and rhyolite) in the SMO region through the Oligocene and early Miocene. They attribute this to the gradual waning of the arc as a slab tear that widened to form a slab window was subducted beneath northwestern Mexico (Ferrari et al., 2018; Mahar et al., 2019). As a result, the local mantle potential temperature increased as up-welling asthenosphere was exposed through the slab window. Reorientation of far-field plate motions (Ferrari et al., 2018) and the local addition of heat to weaken the lithosphere gradually focused crustal extension along the western, younger margin of the SMO where the ca. 24 Ma flare-up was localized. Ultimately crustal extension over the slab window led to the opening of the active spreading center in the Gulf of California (6–0 Ma).

The onset of these gradual changes to crustal extension and increased heat from the deeper mantle began likely before the ca. 24 Ma flare-up within the SMO and are thought to have been on-going throughout much, if not all, of the Oligocene. We propose that the onset of extension in the lower crust allowed mafic melts to more readily intrude than they had in the Eocene and before. However, compared to modern continental arcs, the Oligocene SMO had a volcanic flux about double; therefore, it is likely that extra factors were at play. We suggest that the otherwise unexceptional increase in mantle melt supply was amplified by (1) the remnants of the lower crust and mantle wedge being hydrated and isotopically enriched through the late Cretaceous to Eocene, and (2) the arrival of the still hot and thin oceanic lithosphere preceding the opening slab tear and/or window. Asthenospheric melts from the slab window are a potential source of the coeval SCORBA mafic lavas (Fig. 12B). The presence of readily melted, extensively hydrated lithosphere is central to interpretations of enhanced magmatism through slab rollback (e.g., DeCelles et al., 2009), and cannot be ruled out in this scenario. Slab break-off and slab windows are widely recognized as major perturbations to arc systems that enhance magmatism. These processes are not mutually exclusive, and their coincidence can explain the anomalously high volume of the SMO. If correct, the origins of the SMO are distinctly different from the Mesozoic batholiths of the Cordillera (e.g., Ducea and Barton, 2007), even though they are of similar scales.

SUMMARY

Most SMO magmas were generated by juvenile melts that assimilated ~20% lower crust. The mantle-derived melts fractionated in the lower crust and advected heat into surrounding orthogneisses and paragneisses. The SMO magmas are transitional in Hf-O isotope space between continental arc granites and those formed in extensional arcs and continental rifts, in agreement with interpretations where the SMO represents the first stage of magmatism over subducting slab window during the Eocene to Miocene evolution of the Cordilleran margin from convergent to extensional. The immense volume of the SMO requires an anomalously strong heat source such as a slab window coupled with extension of the upper plate to allow for transfer of magma and heat.

ACKNOWLEDGMENTS

We recognize that this research took place throughout the historic lands of the Rarámuri, and we thank them for their hospitality. Andrews and Busby were supported by National Science Foundation (NSF) award EAR-1019559. Andrews received additional support from NSF awards EAR-1137774 and EAR-1547784. WiscSIMS is supported by NSF (EAR-2004618) and the University of Wisconsin-Madison. The ion microprobe facility at University of California, Los Angeles (UCLA) is partly supported by a grant from the Instrumentation and Facilities Program, Division of Earth Sciences, NSF. Eric Swanson kindly donated several samples. We thank John Valley and Mike Spicuzza at UW-Madison for assistance in oxygen isotope analysis by SIMS and laser fluorination. We thank Luca Ferrari, Jose Duque, Nick Moreno, Brenda Pack, Axel Schmitt, Ming-Chang Liu, Mark Pecha, Matthew Wielicki, Ryan Ickert, Mattias Smit, Charles Knapp, and Scott Boroughs, and we are indebted to William Leeman for support and encouragement. We thank two anonymous reviewers, Associate Editor Jonathan Miller and Editor Shanaka de Silva, for their constructive comments.

REFERENCES CITED

- Aguirre-Díaz, G.J., and Labarthe-Hernández, G., 2003, Fissure-igneimbrites: Fissure-source origin for voluminous ignimbrites of the Sierra Madre Occidental and its relationship with Basin and Range faulting: *Geology*, v. 31, no. 9, p. 773–776, <https://doi.org/10.1130/G19665.1>.
- Aguirre-Díaz, G.J., and McDowell, F.W., 1991, The volcanic section at Nazas, Durango, Mexico, and the possibility of widespread Eocene volcanism within the Sierra Madre Occidental: *Journal of Geophysical Research*. *Solid Earth*, v. 96, p. 13,373–13,388, <https://doi.org/10.1029/91JB00245>.
- Aguirre-Díaz, G.J., and McDowell, F.W., 1993, Nature and timing of faulting and synextensional magmatism in the southern Basin and Range, central-eastern Durango, Mexico: *Geological Society of America Bulletin*, v. 105, p. 1435–1444, [https://doi.org/10.1130/0016-7606\(1993\)105<1435:NATOF>2.3.CO;2](https://doi.org/10.1130/0016-7606(1993)105<1435:NATOF>2.3.CO;2).
- Aguirre-Díaz, G.J., Labarthe-Hernández, G., Tristán-González, M., Nieto-Obregón, J., and Gutiérrez-Palomares, I., 2008, The ignimbrite flare-up and graben calderas of the Sierra Madre Occidental, Mexico: *Developments in Volcanology*, v. 10, p. 143–180, [https://doi.org/10.1016/S1871-644X\(07\)00004-6](https://doi.org/10.1016/S1871-644X(07)00004-6).
- Amelin, Y., and Davis, W.J., 2005, Geochemical test for branching decay of ¹⁷⁶Lu: *Geochimica et Cosmochimica Acta*, v. 69, p. 465–473.
- Annen, C., 2009, From plutons to magma chambers: Thermal constraints on the accumulation of eruptible silicic magma in the upper crust: *Earth and Planetary Science Letters*, v. 284, no. 3–4, p. 409–416, <https://doi.org/10.1016/j.epsl.2009.05.006>.
- Annen, C., and Sparks, R.S.J., 2002, Effects of repetitive emplacement of basaltic intrusions on thermal evolution and melt generation in the crust: *Earth and Planetary Science Letters*, v. 203, no. 3–4, p. 937–955, [https://doi.org/10.1016/S0012-821X\(02\)00929-9](https://doi.org/10.1016/S0012-821X(02)00929-9).
- Annen, C., Blundy, J.D., and Sparks, R.S.J., 2006, The genesis of intermediate and silicic magmas in deep crustal hot zones: *Journal of Petrology*, v. 47, no. 3, p. 505–539, <https://doi.org/10.1093/petrology/egi084>.

- Appleby, S.K., Gillespie, M.R., Graham, C.M., Hinton, R.W., Oliver, G.J., and Kelly, N.M., 2010, Do S-type granites commonly sample infracrustal sources?: New results from an integrated O, U-Pb and Hf isotope study of zircon: Contributions to Mineralogy and Petrology, v. 160, no. 1, p. 115–132, <https://doi.org/10.1007/s00410-009-0469-3>.
- Aranda-Gómez, J.J., Henry, C.D., Ferrari, L., McDowell, F.W., and Valencia-Moreno, M., 2015, La evolución volcánotectónica del noroeste de México durante el Cenozoico: Una sección a lo largo de la autopista MEX 40D a través del campo volcánico de la Sierra Madre Occidental y datos acerca del magmatismo asociado a la extensión en la parte meridional de las provincias tectónicas de Cuenas y Sierras y del Golfo de California: Universidad Nacional Autónoma de México, Centro de Geociencias: Guías de Excursiones Geológicas de México, v. 1, 90 p.
- Attia, S., Cottle, J.M., and Paterson, S.R., 2020, Erupted zircon record of continental crust formation during mantle driven arc flare-ups: Geology, v. 48, no. 5, p. 446–451, <https://doi.org/10.1130/G46991.1>.
- Balsley, S.D., and Gregory, R.T., 1998, Low-¹⁸O silicic magmas: Why are they so rare?: Earth and Planetary Science Letters, v. 162, no. 1–4, p. 123–136, [https://doi.org/10.1016/S0012-821X\(98\)00161-7](https://doi.org/10.1016/S0012-821X(98)00161-7).
- Banik, T.J., Miller, C.F., Fisher, C.M., Coble, M.A., and Vervoort, J.D., 2018, Magmatic-tectonic control on the generation of silicic magmas in Iceland: Constraints from Hafnarfjall-Skarðsheiði volcano: Lithos, v. 318, p. 326–339, <https://doi.org/10.1016/j.lithos.2018.08.022>.
- Bindeman, I., 2008, Oxygen isotopes in mantle and crustal magmas as revealed by single crystal analysis: Reviews in Mineralogy and Geochemistry, v. 69, p. 445–478, <https://doi.org/10.2138/rmg.2008.69.12>.
- Bindeman, I.N., Watts, K.E., Schmitt, A.K., Morgan, L.A., and Shanks, P.W., 2007, Voluminous low ^δ¹⁸O magmas in the late Miocene Heise volcanic field, Idaho: Implications for the fate of Yellowstone hotspot calderas: Geology, v. 35, no. 11, p. 1019–1022, <https://doi.org/10.1130/G24141A.1>.
- Blundy, J., and Wood, B., 2003, Mineral-melt partitioning of uranium, thorium and their daughters: Reviews in Mineralogy and Geochemistry, v. 52, no. 1, p. 59–123, <https://doi.org/10.2113/0520059>.
- Boehnke, P., Watson, E.B., Trail, D., Harrison, T.M., and Schmitt, A.K., 2013, Zircon saturation re-visited: Chemical Geology, v. 351, p. 324–334, <https://doi.org/10.1016/j.chemgeo.2013.05.028>.
- Bolhar, R., Ring, U., Kemp, A.I.S., Whitehouse, M.J., Weaver, S.D., Woodhead, J.D., Uysal, I.T., and Turnbull, R., 2012, An integrated zircon geochronological and geochemical investigation into the Miocene plutonic evolution of the Cyclades, Aegean Sea, Greece: Part 2—Geochemistry: Contributions to Mineralogy and Petrology, v. 164, no. 6, p. 915–933, <https://doi.org/10.1007/s00410-012-0759-z>.
- Bonner, J.L., and Herrin, E.T., 1999, Surface wave studies of the Sierra Madre Occidental of northern Mexico: Bulletin of the Seismological Society of America, v. 89, no. 5, p. 1323–1337.
- Boroghs, S., Wolff, J., Bonnicksen, B., Godchaux, M., and Larson, P., 2005, Large-volume, low-^δ¹⁸O rhyolites of the central Snake River Plain, Idaho, USA: Geology, v. 33, p. 821–824, <https://doi.org/10.1130/G21723.1>.
- Bouvier, A., Vervoort, J.D., and Patchett, P.J., 2008, The Lu-Hf and Sm-Nd isotopic composition of CHUR: Constraints from unequilibrated chondrites and implications for the bulk composition of terrestrial planets: Earth and Planetary Science Letters, v. 273, no. 1–2, p. 48–57, <https://doi.org/10.1016/j.epsl.2008.06.010>.
- Bower, S.M., and Woods, A.W., 1998, On the influence of magma chambers in controlling the evolution of explosive volcanic eruptions: Journal of Volcanology and Geothermal Research, v. 86, p. 67–78, [https://doi.org/10.1016/S0377-0273\(98\)00081-X](https://doi.org/10.1016/S0377-0273(98)00081-X).
- Bowman, J.R., Moser, D.E., Valley, J.W., Wooden, J.L., Kita, N.T., and Mazdab, F.K., 2011, Zircon U-Pb isotope, ^δ¹⁸O and trace element response to 80 m.y. of high temperature metamorphism in the lower crust: Sluggish diffusion and new records of Archean craton formation: American Journal of Science, v. 311, no. 9, p. 719–772, <https://doi.org/10.2475/09.2011.01>.
- Bryan, S.E., and Ferrari, L., 2013, Large igneous provinces and silicic large igneous provinces: Progress in our understanding over the last 25 years: Geological Society of America Bulletin, v. 125, no. 7–8, p. 1053–1078, <https://doi.org/10.1130/B30820.1>.
- Bryan, S.E., Ferrari, L., Reiners, P.W., Allen, C.M., Petrone, C.M., Ramos-Rosique, A., and Campbell, I.H., 2008, New insights into crustal contributions to large-volume rhyolite generation in the mid-Tertiary Sierra Madre Occidental province, Mexico, revealed by U-Pb geochronology: Journal of Petrology, v. 49, no. 1, p. 47–77, <https://doi.org/10.1093/petrology/egm070>.
- Cameron, K.L., and Cameron, M., 1985, Rare earth element, ⁸⁷Sr/⁸⁶Sr, and ¹⁴³Nd/¹⁴⁴Nd compositions of Cenozoic orogenic dacites from Baja California, northwestern Mexico, and adjacent west Texas: Evidence for the predominance of a subcrustal component: Contributions to Mineralogy and Petrology, v. 91, no. 1, p. 1–11, <https://doi.org/10.1007/BF00429422>.
- Cameron, K.L., Cameron, M., Bagby, W.C., Moll, E.J., and Drake, R.E., 1980, Petrologic characteristics of mid-Tertiary volcanic suites, Chihuahua, Mexico: Geology, v. 8, no. 2, p. 87–91, [https://doi.org/10.1130/0091-7613\(1980\)8<87:PCOMVS>2.0.CO;2](https://doi.org/10.1130/0091-7613(1980)8<87:PCOMVS>2.0.CO;2).
- Cameron, K.L., Cameron, M., and Barreiro, B., 1986, Origin of voluminous mid-Tertiary ignimbrites of the Batopilas region, Chihuahua: Implications for the formation of continental crust beneath the Sierra Madre Occidental: Geofísica Internacional, v. 25, no. 1, p. 39–59, <https://doi.org/10.22201/igeof.00167169p.1986.25.1.800>.
- Cameron, K.L., Nimz, G.J., Kuentz, D., Niemeier, S., and Gunn, S., 1989, Southern Cordilleran basaltic andesite suite, southern Chihuahua, Mexico: A link between Tertiary continental arc and flood basalt magmatism in North America: Journal of Geophysical Research. Solid Earth, v. 94, p. 7817–7840, <https://doi.org/10.1029/JB094iB06p07817>.
- Cameron, K.L., Robinson, J.V., Niemeier, S., Nimz, G.J., Kuentz, D.C., Harmon, R.S., Bohlen, S.R., and Collerson, K.D., 1992, Contrasting styles of Pre-Cenozoic and Mid-Tertiary crustal evolution in northern Mexico: Evidence from deep crustal xenoliths from La Olivina: Journal of Geophysical Research. Solid Earth, v. 97, p. 17353–17376, <https://doi.org/10.1029/92JB01493>.
- Campa, M.F., and Coney, P.J., 1983, Tectono-stratigraphic terranes and mineral resource distributions in Mexico: Canadian Journal of Earth Sciences, v. 20, p. 1040–1051, <https://doi.org/10.1139/e83-094>.
- Camprubí, A., Ferrari, L., Cosca, M.A., Cardellach, E., and Canals, À., 2003, Ages of epithermal deposits in Mexico: Regional significance and links with the evolution of Tertiary volcanism: Economic Geology, v. 98, p. 1029–1037, <https://doi.org/10.2113/gsecongeo.98.5.1029>.
- Carley, T.L., Miller, C.F., Fisher, C.M., Hanchar, J.M., Vervoort, J.D., Schmitt, A.K., Economos, R.C., Jordan, B.T., Padilla, A.J., and Banik, T.J., 2020, Petrogenesis of silicic magmas in Iceland through space and time: The isotopic record preserved in zircon and whole rocks: Journal of Geology, v. 128, p. 1–28, <https://doi.org/10.1086/706261>.
- Cather, S.M., Dunbar, N.W., McDowell, F.W., McIntosh, W.C., and Scholle, P.A., 2009, Climate forcing by iron fertilization from repeated ignimbrite eruptions: The icehouse–silicic large igneous province (SLIP) hypothesis: Geosphere, v. 5, p. 315–324, <https://doi.org/10.1130/GES00188.1>.
- Centeno-García, E., Ruiz, J., Coney, P.J., Patchett, P.J., and Ortega-Gutiérrez, F., 1993, Guerrero terrane of Mexico: Its role in the Southern, Cordillera from new geochemical data: Geology, v. 21, p. 419–422, [https://doi.org/10.1130/0091-7613\(1993\)021<0419:GTOMIR>2.3.CO;2](https://doi.org/10.1130/0091-7613(1993)021<0419:GTOMIR>2.3.CO;2).
- Cochemé, J.J., and Demant, A., 1991, Geology of the Yécora area, northern Sierra Madre Occidental, Mexico, in Pérez-Segura, E., and Jacques-Ayala, C., eds., Studies of Sonoran Geology: Geological Society of America Special Paper 254, p. 81–94, <https://doi.org/10.1130/SPE254-p81>.
- Colón, D.P., Bindeman, I.N., Wotzlaw, J.F., Christiansen, E.H., and Stern, R.A., 2018, Origins and evolution of rhyolitic magmas in the central Snake River Plain: Insights from coupled high-precision geochronology, oxygen isotope, and hafnium isotope analyses of zircon: Contributions to Mineralogy and Petrology, v. 173, no. 2, p. 11–18, <https://doi.org/10.1007/s00410-017-1437-y>.
- Crisp, J.A., 1984, Rates of magma emplacement and volcanic output: Journal of Volcanology and Geothermal Research, v. 20, no. 3–4, p. 177–211, [https://doi.org/10.1016/0377-0273\(84\)90039-8](https://doi.org/10.1016/0377-0273(84)90039-8).
- Damon, P.E., Shafiqullah, M., and Clark, K.F., 1981, Age trends of igneous activity in relation to metallogenesis in the southern Cordillera, in Dickinson, W.R., and Payne, W.D., eds., Relations of Tectonics to Ore Deposits in the Southern Cordillera: Arizona Geological Digest, v. 14, p. 137–154.
- DeCelles, P.G., Ducea, M.N., Kapp, P., and Zandt, G., 2009, Cyclicity in Cordilleran orogenic systems: Nature Geoscience, v. 2, no. 4, p. 251–257, <https://doi.org/10.1038/ngeo469>.
- DePaolo, D.J., 1981, Trace element and isotopic effects of combined wallrock assimilation and fractional crystallization: Earth and Planetary Science Letters, v. 53, no. 2, p. 189–202, [https://doi.org/10.1016/0012-821X\(81\)90153-9](https://doi.org/10.1016/0012-821X(81)90153-9).
- de Silva, S.L., and Gosnold, W.D., 2007, Episodic construction of batholiths: Insights from the spatiotemporal development of an ignimbrite flare-up: Journal of Volcanology and Geothermal Research, v. 167, no. 1–4, p. 320–335, <https://doi.org/10.1016/j.jvolgeores.2007.07.015>.
- Dickinson, W.R., and Lawton, T.F., 2001, Carboniferous to Cretaceous assembly and fragmentation of Mexico: Geological Society of America Bulletin, v. 113, p. 1142–1160, [https://doi.org/10.1130/0016-7606\(2001\)113<1142:CTCAAF>2.0.CO;2](https://doi.org/10.1130/0016-7606(2001)113<1142:CTCAAF>2.0.CO;2).
- Ducea, M.N., and Barton, M.D., 2007, Igniting flare-up events in Cordilleran arcs: Geology, v. 35, no. 11, p. 1047–1050, <https://doi.org/10.1130/G23898A.1>.
- Dufek, J., and Bergantz, G.W., 2005, Lower crustal magma genesis and preservation: a stochastic framework for the evaluation of basalt-crust interaction: Journal of Petrology, v. 46, no. 11, p. 2167–2195, <https://doi.org/10.1093/petrology/egi049>.

- Dunbar, N.W., Riciputi, L.R., Jacobs, G.K., Naney, M.T., and Christie, W., 1993, Generation of rhyolitic melt in an artificial magma: Implications for fractional crystallization processes in natural magmas: *Journal of Volcanology and Geothermal Research*, v. 57, no. 3–4, p. 157–166, [https://doi.org/10.1016/0377-0273\(93\)90010-O](https://doi.org/10.1016/0377-0273(93)90010-O).
- Ferrari, L., López-Martínez, M., and Rosas-Elguera, J., 2002, Ignimbrite flare-up and deformation in the southern Sierra Madre Occidental, western Mexico: Implications for the late subduction history of the Farallon plate: *Tectonics*, v. 21, no. 4, p. 17–1–17–24, <https://doi.org/10.1029/2001TC001302>.
- Ferrari, L., Valencia-Moreno, M., and Bryan, S., 2007, Magmatism and tectonics of the Sierra Madre Occidental and its relation with the evolution of the western margin of North America, in Alaniz-Álvarez, S.A., and Nieto-Samaniego, Á.F., eds., *Geology of México: Celebrating the Centenary of the Geological Society of México: Geological Society of America Special Paper 422*, p. 1–39, [https://doi.org/10.1130/2007.2422\(01\)](https://doi.org/10.1130/2007.2422(01)).
- Ferrari, L., López-Martínez, M., Orozco-Esquivel, T., Bryan, S.E., Duque-Trujillo, J., Lonsdale, P., and Solari, L., 2013, Late Oligocene to Middle Miocene rifting and synextensional magmatism in the southwestern Sierra Madre Occidental, Mexico: The beginning of the Gulf of California rift: *Geosphere*, v. 9, no. 5, p. 1161–1200, <https://doi.org/10.1130/GES00925.1>.
- Ferrari, L., Orozco-Esquivel, T., Bryan, S.E., Lopez-Martinez, M., and Silva-Fragoso, A., 2018, Cenozoic magmatism and extension in western Mexico: Linking the Sierra Madre Occidental silicic large igneous province and the Comondú Group with the Gulf of California rift: *Earth-Science Reviews*, v. 183, p. 115–152, <https://doi.org/10.1016/j.earscirev.2017.04.006>.
- Fisher, C.M., Vervoort, J.D., and DuFrane, S.A., 2014, Accurate Hf isotope determinations of complex zircons using the “laser ablation split stream” method: *Geochemistry, Geophysics, Geosystems*, v. 15, no. 1, p. 121–139, <https://doi.org/10.1002/2013GC004962>.
- García, J.A., Mahar, M.A., Goodell, P.C., Molina, C., and Ricketts, J.W., 2021, Petrology, geochemistry, stratigraphy, zircon U-Pb geochronology and Hf isotopic compositions of subsurface lithologies in northwestern Mesa Central, Durango, Mexico: Implications for the tectonomagmatic evolution of northwestern Mexico: *Gondwana Research*, v. 93, p. 1–25, <https://doi.org/10.1016/j.gr.2021.01.005>.
- Gehrels, G., and Pecha, M., 2014, Detrital zircon U-Pb geochronology and Hf isotope geochemistry of Paleozoic and Triassic passive margin strata of western North America: *Geosphere*, v. 10, p. 49–65, <https://doi.org/10.1130/GES00889.1>.
- Giordano, D., Russell, J.K., and Dingwell, D.B., 2008, Viscosity of magmatic liquids: A model: *Earth and Planetary Science Letters*, v. 271, no. 1–4, p. 123–134, <https://doi.org/10.1016/j.epsl.2008.03.038>.
- Gomberg, J., Priestley, K., and Brune, J., 1989, The compressional velocity structure of the crust and upper mantle of northern Mexico and the border region: *Bulletin of the Seismological Society of America*, v. 79, no. 5, p. 1496–1519.
- Gualda, G.A., and Ghiorso, M.S., 2014, Phase-equilibrium geobarometers for silicic rocks based on rhyolite-MELTS. Part 1: Principles, procedures, and evaluation of the method: *Contributions to Mineralogy and Petrology*, v. 168, no. 1, p. 1033, <https://doi.org/10.1007/s00410-014-1033-3>.
- Gualda, G.A., Ghiorso, M.S., Lemons, R.V., and Carley, T.L., 2012, Rhyolite-MELTS: A modified calibration of MELTS optimized for silica-rich, fluid-bearing magmatic systems: *Journal of Petrology*, v. 53, no. 5, p. 875–890, <https://doi.org/10.1093/petrology/egr080>.
- Halder, M., Paul, D., and Sensarma, S., 2021, Rhyolites in continental mafic Large Igneous Provinces: *Petrology, geochemistry and petrogenesis: Geoscience Frontiers*, v. 12, no. 1, p. 53–80, <https://doi.org/10.1016/j.gsf.2020.06.011>.
- Hanchar, J.M., and Watson, E.B., 2003, Zircon saturation thermometry: *Reviews in Mineralogy and Geochemistry*, v. 53, no. 1, p. 89–112, <https://doi.org/10.2113/0530089>.
- Hawkesworth, C.J., and Kemp, A.I.S., 2006, Using hafnium and oxygen isotopes in zircons to unravel the record of crustal evolution: *Chemical Geology*, v. 226, no. 3–4, p. 144–162, <https://doi.org/10.1016/j.chemgeo.2005.09.018>.
- Henry, C.D., and Aranda-Gomez, J.J., 1992, The real southern Basin and Range: Mid- to late Cenozoic extension in Mexico: *Geology*, v. 20, no. 8, p. 701–704, [https://doi.org/10.1130/0091-7613\(1992\)020<0701:TRSBAR>2.3.CO;2](https://doi.org/10.1130/0091-7613(1992)020<0701:TRSBAR>2.3.CO;2).
- Henry, C.D., and Aranda-Gomez, J.J., 2000, Plate interactions control middle–late Miocene, pro-Gulf and Basin and Range extension in the southern Basin and Range: *Tectonophysics*, v. 318, no. 1–4, 26 p., [https://doi.org/10.1016/S0040-1951\(99\)00304-2](https://doi.org/10.1016/S0040-1951(99)00304-2).
- Henry, C.D., McIntosh, W.C., McDowell, F.W., Lipman, P.W., and Chapin, C.E., 2012, The Cenozoic ignimbrite flareup in western North America: Distribution, timing, volume, and tectonic relations: *Geological Society of America Abstracts with Programs*, v. 44, no. 3, p. 21.
- Hiess, J., Bennett, V.C., Nutman, A.P., and Williams, I.S., 2009, In situ U-Pb, O and Hf isotopic compositions of zircon and olivine from Eoarchean rocks, West Greenland: New insights to making old crust: *Geochimica et Cosmochimica Acta*, v. 73, no. 15, p. 4489–4516, <https://doi.org/10.1016/j.gca.2009.04.019>.
- Hiess, J., Bennett, V.C., Nutman, A.P., and Williams, I.S., 2011, Archaean fluid-assisted crustal cannibalism recorded by low $\delta^{18}\text{O}$ and negative $\epsilon\text{Hf}(T)$ isotopic signatures of West Greenland granite zircon: *Contributions to Mineralogy and Petrology*, v. 161, no. 6, p. 1027–1050, <https://doi.org/10.1007/s00410-010-0578-z>.
- Hildreth, W., and Moorbath, S., 1988, Crustal contributions to arc magmatism in the Andes of central Chile: *Contributions to Mineralogy and Petrology*, v. 98, no. 4, p. 455–489, <https://doi.org/10.1007/BF00372365>.
- Huppert, H.E., and Sparks, R.S.J., 1988, The generation of granitic magmas by intrusion of basalt into continental crust: *Journal of Petrology*, v. 29, no. 3, p. 599–624, <https://doi.org/10.1093/petrology/29.3.599>.
- Jicha, B.R., Scholl, D.W., and Rea, D.K., 2009, Circum-Pacific arc flare-ups and global cooling near the Eocene–Oligocene boundary: *Geology*, v. 37, no. 4, p. 303–306, <https://doi.org/10.1130/G25392A.1>.
- Kemp, A.I.S., Hawkesworth, C.J., Paterson, B.A., and Kinny, P.D., 2006, Episodic growth of the Gondwana supercontinent from hafnium and oxygen isotopes in zircon: *Nature*, v. 439, no. 7076, p. 580–583, <https://doi.org/10.1038/nature04505>.
- Kemp, A.I.S., Hawkesworth, C.J., Foster, G.L., Paterson, B.A., Woodhead, J.D., Hergt, J.M., and Hergt, J.M., 2007, Magmatic and crustal differentiation history of granitic rocks from Hf-O isotopes in zircon: *Science*, v. 315, no. 5814, p. 980–983, <https://doi.org/10.1126/science.1136154>.
- Keppie, J.D., and Ortega-Gutiérrez, E., 1995, Provenance of Mexican terranes: Isotopic constraints: *International Geology Review*, v. 37, no. 9, p. 813–824, <https://doi.org/10.1080/00206819509465428>.
- Kinny, P.D., and Maas, R., 2003, Lu-Hf and Sm-Nd isotope systems in zircon: *Reviews in Mineralogy and Geochemistry*, v. 53, no. 1, p. 327–341, <https://doi.org/10.2113/0530327>.
- Kita, N.T., Ushikubo, T., Fu, B., and Valley, J.W., 2009, High precision SIMS oxygen isotope analysis and the effect of sample topography: *Chemical Geology*, v. 264, no. 1–4, p. 43–57, <https://doi.org/10.1016/j.chemgeo.2009.02.012>.
- Lanphere, M.A., Cameron, K.L., and Cameron, M., 1980, Sr isotopic geochemistry of voluminous rhyolitic ignimbrites and related rocks, Batopilas area, western Mexico: *Nature*, v. 286, no. 5773, p. 594–596, <https://doi.org/10.1038/286594a0>.
- Laske, G., Masters, G., Ma, Z., and Pasyanos, M., 2013, Update on CRUST1.0—A 1-degree global model of Earth’s crust: *Geophysical Research Abstracts*, no. 15, p. 2658.
- Lee, C.T.A., Morton, D.M., Kistler, R.W., and Baird, A.K., 2007, Petrology and tectonics of Phanerozoic continent formation: From island arcs to accretion and continental arc magmatism: *Earth and Planetary Science Letters*, v. 263, no. 3–4, p. 370–387, <https://doi.org/10.1016/j.epsl.2007.09.025>.
- Lee, C.T.A., Luffi, P., and Chin, E.J., 2011, Building and destroying continental mantle: *Annual Review of Earth and Planetary Sciences*, v. 39, p. 59–90, <https://doi.org/10.1146/annurev-earth-040610-133505>.
- Liu, C.-Z., Wu, F.-Y., Chung, S.-L., Li, Q.-L., Sun, W.-D., and Qi, W.-Q., 2014, A ‘hidden’ ^{18}O -enriched reservoir in the sub-arc mantle: *Scientific Reports*, v. 4, p. 4232, <https://doi.org/10.1038/srep04232>.
- Mahar, M.A., Goodell, P.C., Ramírez, A., and García, J., 2019, Timing and origin of silicic volcanism in northwestern Mexico: Insights from zircon U-Pb geochronology, Hf isotopes and geochemistry of rhyolite ignimbrites from Palmarejo and Guazapares in Southwest Chihuahua: *Lithos*, v. 324, p. 246–264, <https://doi.org/10.1016/j.lithos.2018.11.010>.
- McDowell, F.W., 2007, Geologic transect across the Northern Sierra Madre Occidental volcanic field, Chihuahua and Sonora, Mexico: *Geological Society of America Digital Map and Chart Series*, 6, 70 p., <https://doi.org/10.1130/2007.DMCH006.TXT>.
- McDowell, F.W., and Keizer, R.P., 1977, Timing of mid-Tertiary volcanism in the Sierra Madre Occidental between Durango City and Mazatlán, Mexico: *Geological Society of America Bulletin*, v. 88, p. 1479–1487, [https://doi.org/10.1130/0016-7606\(1977\)88<1479:TOMVIT>2.0.CO;2](https://doi.org/10.1130/0016-7606(1977)88<1479:TOMVIT>2.0.CO;2).
- McDowell, F.W., and Mauger, R.L., 1994, K-Ar and U-Pb zircon chronology of Late Cretaceous and Tertiary magmatism in central Chihuahua State, Mexico: *Geological Society of America Bulletin*, v. 106, p. 118–132, [https://doi.org/10.1130/0016-7606\(1994\)106<0118:KAAUPZ>2.3.CO;2](https://doi.org/10.1130/0016-7606(1994)106<0118:KAAUPZ>2.3.CO;2).
- McDowell, F.W., and McIntosh, W.C., 2012, Timing of intense magmatic episodes in the northern and central Sierra Madre Occidental, western Mexico: *Geosphere*, v. 8, p. 1505–1526, <https://doi.org/10.1130/GES00792.1>.

- Miller, C.F., McDowell, S.M., and Mapes, R.W., 2003, Hot and cold granites?: Implications of zircon saturation temperatures and preservation of inheritance: *Geology*, v. 31, no. 6, p. 529–532, [https://doi.org/10.1130/0091-7613\(2003\)031<0529:HACGIO>2.0.CO;2](https://doi.org/10.1130/0091-7613(2003)031<0529:HACGIO>2.0.CO;2).
- Moreno, N., 2016, U-Pb and ⁴⁰Ar/³⁹Ar geochronology of rhyolitic tuffs and lavas of the Sierra Madre Occidental silicic large igneous province: Insights into Eocene–Oligocene silicic volcanism from a new sample transect, Chihuahua and Durango border region, northern Mexico [M.S. thesis]: California State University Bakersfield, 93 p.
- Murray, B.P., and Busby, C.J., 2015, Epithermal mineralization controlled by synextensional magmatism in the Guazapares Mining District of the Sierra Madre Occidental silicic large igneous province, Mexico: *Journal of South American Earth Sciences*, v. 58, p. 54–71, <https://doi.org/10.1016/j.jsames.2014.12.009>.
- Murray, B.P., Busby, C.J., Ferrari, L., and Solari, L.A., 2013, Synvolcanic crustal extension during the mid-Cenozoic ignimbrite flare-up in the northern Sierra Madre Occidental, Mexico: Evidence from the Guazapares Mining District region, western Chihuahua: *Geosphere*, v. 9, p. 1201–1235, <https://doi.org/10.1130/GES00862.1>.
- Murray, B.P., Busby, C.J., and Verde Ramirez, M.D.L.A., 2015, Extension and magmatism in the Cerocahui basin, northern Sierra Madre Occidental, western Chihuahua, Mexico: *International Geology Review*, v. 57, no. 5–8, p. 893–918, <https://doi.org/10.1080/00206814.2014.941022>.
- Nimz, G.J., Cameron, K.L., and Niemeyer, S., 1995, Formation of mantle lithosphere beneath northern Mexico: Chemical and Sr–Nd–Pb isotopic systematics of peridotite xenoliths from La Olivina: *Journal of Geophysical Research. Solid Earth*, v. 100, p. 4181–4196, <https://doi.org/10.1029/94JB02776>.
- Ortega-Gutiérrez, F., Elías-Herrera, M., Morán-Zenteno, D.J., Solari, L., Weber, B., and Luna-González, L., 2018, The pre-Mesozoic metamorphic basement of Mexico, 1.5 billion years of crustal evolution: *Earth-Science Reviews*, v. 183, p. 2–37, <https://doi.org/10.1016/j.earscirev.2018.03.006>.
- Paces, J.B., and Miller, J.D., 1993, Precise U–Pb ages of Duluth complex and related mafic intrusions, northeastern Minnesota: Geochronological insights to physical, petrogenetic, paleomagnetic, and tectonomagmatic processes associated with the 1.1 Ga midcontinent rift system: *Journal of Geophysical Research. Solid Earth*, v. 98, p. 13,997–14,013, <https://doi.org/10.1029/93JB01159>.
- Pack, B., 2017, Double dating and oxygen isotope analysis of silicic lavas and ignimbrites from the Sierra Madre Occidental Silicic Large Igneous Province (Mexico): Insights into the sources and timescales of magma generation in an arc flare-up [M.S. thesis]: California State University Bakersfield, 112 p.
- Page, F.Z., Ushikubo, T., Kita, N.T., Riciputi, L.R., and Valley, J.W., 2007, High-precision oxygen isotope analysis of picogram samples reveals 2 μm gradients and slow diffusion in zircon: *The American Mineralogist*, v. 92, no. 10, p. 1772–1775, <https://doi.org/10.2138/am.2007.2697>.
- Patchett, P.J., 1983, Importance of the Lu–Hf isotopic system in studies of planetary chronology and chemical evolution: *Geochimica et Cosmochimica Acta*, v. 47, p. 81–91, [https://doi.org/10.1016/0016-7037\(83\)90092-3](https://doi.org/10.1016/0016-7037(83)90092-3).
- Patchett, P.J., and Tatsumoto, M., 1981, A routine high-precision method for Lu–Hf isotope geochemistry and chronology: *Contributions to Mineralogy and Petrology*, v. 75, p. 263–267, <https://doi.org/10.1007/BF01166766>.
- Purucker, M., Sabaka, T., Le, G., Slavín, J.A., Strangeway, R.J., and Busby, C., 2007, Magnetic field gradients from the ST-5 constellation: Improving magnetic and thermal models of the lithosphere: *Geophysical Research Letters*, v. 34, no. 24, <https://doi.org/10.1029/2007GL031739>.
- Rudnick, R.L., and Cameron, K.L., 1991, Age diversity of the deep crust in northern Mexico: *Geology*, v. 19, p. 1197–1200, [https://doi.org/10.1130/0091-7613\(1991\)019<1197:ADOTDC>2.3.CO;2](https://doi.org/10.1130/0091-7613(1991)019<1197:ADOTDC>2.3.CO;2).
- Ruiz, J., Patchett, P.J., and Ortega-Gutiérrez, F., 1988a, Proterozoic and Phanerozoic basement terranes of Mexico from Nd isotopic studies: *Geological Society of America Bulletin*, v. 100, p. 274–281, [https://doi.org/10.1130/0016-7606\(1988\)100<0274:PAPBTO>2.3.CO;2](https://doi.org/10.1130/0016-7606(1988)100<0274:PAPBTO>2.3.CO;2).
- Ruiz, J., Patchett, P.J., and Arculus, R.J., 1988b, Nd–Sr isotope composition of lower crustal xenoliths—Evidence for the origin of mid-Tertiary felsic volcanics in Mexico: *Contributions to Mineralogy and Petrology*, v. 99, no. 1, p. 36–43, <https://doi.org/10.1007/BF00399363>.
- Ruiz, J., Patchett, P.J., and Arculus, R.J., 1990, Reply to “Comments on Nd–Sr isotopic compositions of lower crustal xenoliths—Evidence for the origin of mid-Tertiary felsic volcanics in Mexico” by K.L. Cameron and J.V. Robinson: *Contributions to Mineralogy and Petrology*, v. 104, no. 5, p. 615–618, <https://doi.org/10.1007/BF00306669>.
- Saleeby, J., Ducea, M., and Clemens-Knott, D., 2003, Production and loss of high-density batholithic root, southern Sierra Nevada, California: *Tectonics*, v. 22, no. 6, <https://doi.org/10.1029/2002TC001374>.
- Sañudo-Wilhelmy, S.A., and Flegal, A.R., 1994, Temporal variations in lead concentrations and isotopic composition in the Southern California Bight: *Geochimica et Cosmochimica Acta*, v. 58, no. 15, p. 3315–3320, [https://doi.org/10.1016/0016-7037\(94\)90060-4](https://doi.org/10.1016/0016-7037(94)90060-4).
- Scarfe, C.M., Mysen, B.O., and Virgo, D., 1987, Pressure dependence of the viscosity of silicate melts. *Magmatic Processes: Physicochemical Principles: Geochemical Society Special Publication*, v. 1, p. 59–67.
- Schmitt, A.K., Grove, M., Harrison, T.M., Lovera, O., Hulen, J., and Walters, M., 2003, The Geysers–Cobb Mountain Magma System, California (Part 1): U–Pb zircon ages of volcanic rocks, conditions of zircon crystallization and magma residence times: *Geochimica et Cosmochimica Acta*, v. 67, no. 18, p. 3423–3442, [https://doi.org/10.1016/S0016-7037\(03\)0140-6](https://doi.org/10.1016/S0016-7037(03)0140-6).
- Sedlock, R.L., Ortega-Gutiérrez, F., and Speed, R.C., 1993, Tectonostratigraphic Terranes and Tectonic Evolution of Mexico: *Geological Society of America Special Publication 278*, <https://doi.org/10.1130/SPE278>.
- Siégel, C., Bryan, S.E., Allen, C.M., and Gust, D.A., 2018, Use and abuse of zircon-based thermometers: A critical review and a recommended approach to identify antecrystic zircons: *Earth-Science Reviews*, v. 176, p. 87–116, <https://doi.org/10.1016/j.earscirev.2017.08.011>.
- Smith, R.D., Cameron, K.L., McDowell, F.W., Niemeyer, S., and Sampson, D.E., 1996, Generation of voluminous silicic magmas and formation of mid-Cenozoic crust beneath north-central Mexico: Evidence from ignimbrites, associated lavas, deep crustal granulites, and mantle pyroxenites: *Contributions to Mineralogy and Petrology*, v. 123, no. 4, p. 375–389, <https://doi.org/10.1007/s004100050163>.
- Spicuzza, M.J., Valley, J.W., Kohn, M.J., Girard, J.P., and Fouillac, A.M., 1998, The rapid heating, defocused beam technique: A CO₂-laser-based method for highly precise and accurate determination of δ¹⁸O values of quartz: *Chemical Geology*, v. 144, no. 3–4, p. 195–203, [https://doi.org/10.1016/S0009-2541\(97\)00131-9](https://doi.org/10.1016/S0009-2541(97)00131-9).
- Stelten, M.E., Cooper, K.M., Vazquez, J.A., Reid, M.R., Barfod, G.H., Wimpenny, J., and Yin, Q.Z., 2013, Magma mixing and the generation of isotopically juvenile silicic magma at Yellowstone caldera inferred from coupling ²³⁸U–²³⁰Th ages with trace elements and Hf and O isotopes in zircon and Pb isotopes in sanidine: *Contributions to Mineralogy and Petrology*, v. 166, no. 2, p. 587–613, <https://doi.org/10.1007/s00410-013-0893-2>.
- Swanson, E.R., and McDowell, F.W., 1984, Calderas of the Sierra Madre Occidental volcanic field western Mexico: *Journal of Geophysical Research. Solid Earth*, v. 89, p. 8787–8799, <https://doi.org/10.1029/JB089iB10p08787>.
- Swanson, E.R., and McDowell, F.W., 1985, Geology and geochronology of the Tomochic caldera, Chihuahua, Mexico: *Geological Society of America Bulletin*, v. 96, p. 1477–1482, [https://doi.org/10.1130/0016-7606\(1985\)96<1477:GAGOTT>2.0.CO;2](https://doi.org/10.1130/0016-7606(1985)96<1477:GAGOTT>2.0.CO;2).
- Swanson, E.R., Keizer, R.P., Lyons, J.L., and Clabough, S.E., 1978, Tertiary volcanism and caldera development near Durango City, Sierra Madre Occidental, Mexico: *Geological Society of America Bulletin*, v. 89, p. 1000–1012, [https://doi.org/10.1130/0016-7606\(1978\)89<1000:TVACDN>2.0.CO;2](https://doi.org/10.1130/0016-7606(1978)89<1000:TVACDN>2.0.CO;2).
- Swanson, E.R., Kempton, K.A., McDowell, F.W., and McIntosh, W.C., 2006, Major ignimbrites and volcanic centers of the Copper Canyon area: A view into the core of Mexico’s Sierra Madre Occidental: *Geosphere*, v. 2, p. 125–141, <https://doi.org/10.1130/GES00042.1>.
- Torres-Hernández, J.R., Labarthe-Hernández, G., Aguillón-Robles, A., Gómez-Anguiano, M., and Mata-Segura, J.L., 2006, The pyroclastic dikes of the Tertiary San Luis Potosí volcanic field: Implications on the emplacement of Panalillo ignimbrite: *Geofísica Internacional*, v. 45, no. 4, p. 243–253, <https://doi.org/10.22201/igeof.00167169p.2006.45.4.161>.
- Trail, D., Mojzsis, S.J., Harrison, T.M., Schmitt, A.K., Watson, E.B., and Young, E.D., 2007, Constraints on Hadean zircon protoliths from oxygen isotopes, Ti-thermometry, and rare earth elements: *Geochemistry, Geophysics, Geosystems*, v. 8, no. 6, <https://doi.org/10.1029/2006GC001449>.
- Tristán-González, M., Labarthe-Hernández, G., Aguirre-Díaz, G.J., and Aguillón-Robles, A., 2008, Tectono-volcanic control of fissure type vents for the 28 Ma Panalillo ignimbrite in the Villa de Reyes Graben, San Luis Potosí, México: *IOP Conference Series. Earth and Environmental Science*, v. 3, no. 1, p. 012026, <https://doi.org/10.1088/1755-1307/3/1/012026>.
- Valley, J.W., 2003, Oxygen isotopes in zircon: *Reviews in Mineralogy and Geochemistry*, v. 53, p. 343–385, <https://doi.org/10.2113/0530343>.
- Valley, J.W., and Kita, N.T., 2009, In situ oxygen isotope geochemistry by ion microprobe. *Mineralogical Association of Canada short course: Secondary Ion Mass Spectrometry in the Earth Sciences*, v. 41, p. 19–63.
- Valley, J.W., Chiarenzelli, J.R., and McLelland, J.M., 1994, Oxygen isotope geochemistry of zircon: *Earth and Planetary Science Letters*, v. 126, no. 4, p. 187–206, [https://doi.org/10.1016/0012-821X\(94\)90106-6](https://doi.org/10.1016/0012-821X(94)90106-6).

- Valley, J.W., Kitchen, N., Kohn, M.J., Niendorf, C.R., and Spicuzza, M.J., 1995, UWG-2, a garnet standard for oxygen isotope ratios: Strategies for high precision and accuracy with laser heating: *Geochimica et Cosmochimica Acta*, v. 59, no. 24, p. 5223–5231, [https://doi.org/10.1016/0016-7037\(95\)00386-X](https://doi.org/10.1016/0016-7037(95)00386-X).
- Valley, J.W., Bindeman, I.N., and Peck, W.H., 2003, Empirical calibration of oxygen isotope fractionation in zircon: *Geochimica et Cosmochimica Acta*, v. 67, no. 17, p. 3257–3266, [https://doi.org/10.1016/S0016-7037\(03\)00090-5](https://doi.org/10.1016/S0016-7037(03)00090-5).
- Valley, J.W., Lackey, J.S., Cavosie, A.J., Clechenko, C.C., Spicuzza, M.J., Basei, M.A.S., Bindeman, I.N., Ferreira, V.P., Sial, A.N., King, E.M., Peck, W.H., Sinha, A.K., and Wei, C.S., 2005, 4.4 billion years of crustal maturation: Oxygen isotope ratios of magmatic zircon: *Contributions to Mineralogy and Petrology*, v. 150, no. 6, p. 561–580, <https://doi.org/10.1007/s00410-005-0025-8>.
- Vermeesch, P., 2018, IsoplotR: A free and open toolbox for geochronology: *Geoscience Frontiers*, v. 9, no. 5, p. 1479–1493, <https://doi.org/10.1016/j.gsf.2018.04.001>.
- Vervoort, J.D., Patchett, P.J., Söderlund, U., and Baker, M., 2004, Isotopic composition of Yb and the determination of Lu concentrations and Lu/Hf ratios by isotope dilution using MC-ICPMS: *Geochemistry, Geophysics, Geosystems*, v. 5, <https://doi.org/10.1029/2004GC000721>.
- Vervoort, J.D., Plank, T., and Prytulak, J., 2011, The Hf-Nd isotopic composition of marine sediments: *Geochimica et Cosmochimica Acta*, v. 75, no. 20, p. 5903–5926, <https://doi.org/10.1016/j.gca.2011.07.046>.
- Wang, X.-L., Coble, M.A., Valley, J.W., Shu, X.-J., Kitajima, K., Spicuzza, M.J., and Sun, T., 2014, Influence of radiation damage on late Jurassic zircon from southern China: Evidence from in situ measurement of oxygen isotopes, laser Raman, U-Pb ages, and trace elements: *Chemical Geology*, v. 389, p. 122–136, <https://doi.org/10.1016/j.chemgeo.2014.09.013>.
- Wark, D.A., 1991, Oligocene ash flow volcanism, northern Sierra Madre Occidental: Role of mafic and intermediate-composition magmas in rhyolite genesis: *Journal of Geophysical Research. Solid Earth*, v. 96, p. 13,389–13,411, <https://doi.org/10.1029/90JB02666>.
- Watson, E.B., and Harrison, T.M., 1983, Zircon saturation revisited: Temperature and composition effects in a variety of crustal magma types: *Earth and Planetary Science Letters*, v. 64, no. 2, p. 295–304, [https://doi.org/10.1016/0012-821X\(83\)90211-X](https://doi.org/10.1016/0012-821X(83)90211-X).
- White, S.M., Crisp, J.A., and Spera, F.J., 2006, Long-term volumetric eruption rates and magma budgets: *Geochemistry, Geophysics, Geosystems*, v. 7, no. 3, <https://doi.org/10.1029/2005GC001002>.
- Wiedenbeck, M., Allé, P., Corfu, F., Griffin, W., Meier, M., Oberli, F., Quadt, A.V., Roddick, J., and Spiegel, W., 1995, Three natural zircon standards for U-Th-Pb, Lu-Hf, trace element and REE analyses: *Geostandards and Geoanalytical Research*, v. 19, no. 1, p. 1–23, <https://doi.org/10.1111/j.1751-908X.1995.tb00147.x>.
- Wiedenbeck, M., Hanchar, J.M., Peck, W.H., Sylvester, P., Valley, J., Whitehouse, M., Kronz, A., Morishita, Y., Nasdala, L., and Fiebig, J., 2004, Further characterisation of the 91500 zircon crystal: *Geostandards and Geoanalytical Research*, v. 28, no. 1, p. 9–39, <https://doi.org/10.1111/j.1751-908X.2004.tb01041.x>.
- Woodhead, J., Hergt, J., Shelley, M., Eggins, S., and Kemp, R., 2004, Zircon Hf-isotope analysis with an excimer laser, depth profiling, ablation of complex geometries, and concomitant age estimation: *Chemical Geology*, v. 209, p. 121–135, <https://doi.org/10.1016/j.chemgeo.2004.04.026>.
- Zhao, J.H., Zhou, M.F., and Zheng, J.P., 2013, Constraints from zircon U-Pb ages, O and Hf isotopic compositions on the origin of Neoproterozoic peraluminous granitoids from the Jiangnan Fold Belt, South China: *Contributions to Mineralogy and Petrology*, v. 166, no. 5, p. 1505–1519, <https://doi.org/10.1007/s00410-013-0940-z>.
- Zheng, Y.F., Zhao, Z.F., Wu, Y.B., Zhang, S.B., Liu, X., and Wu, F.Y., 2006, Zircon U-Pb age, Hf and O isotope constraints on protolith origin of ultrahigh-pressure eclogite and gneiss in the Dabie orogen: *Chemical Geology*, v. 231, no. 1–2, p. 135–158, <https://doi.org/10.1016/j.chemgeo.2006.01.005>.
- Zhu, L.F., Pan, X., and Sun, J.Z., 2016, Visualization and dissemination of global crustal models on virtual globes: *Computers & Geosciences*, v. 90, p. 34–40, <https://doi.org/10.1016/j.cageo.2016.01.015>.